RICE UNIVERSITY

Expansion and Shockwave Development in Ultracold Neutral Plasmas with an Initial Exponentially Decaying Density Distribution

---

by

MacKenzie Warrens

April 14, 2025

"Apart from Me you can do nothing."

John 15:5

Abstract

Ultracold neutral plasmas (UNPs), which are formed by photoionizing a cloud of cold atoms, have been a powerful platform for studying a wide variety of plasma phenomena. Two areas of interest include expansion into vacuum and the development of shockwaves. Previous UNP experiments have used plasmas with an initial Gaussian density distribution. UNPs with a radially exponentially decaying density distribution, or exponential UNPs, can be formed by photoionizing atoms out of a purely magnetic trap. This dissertation studies the expansion in free space of exponential UNPs as well as the development and characterization of shockwaves in exponential UNPs.

The free space expansion of an exponential UNP is compared to the well-known self-similar hydrodynamic expansion of a Gaussian plasma. Similar scaling laws describe the size evolution well for both cases. The evolution of the plasma size and velocity show a characteristic ion acoustic time scale, indicating that the plasma is generally well-described by a hydrodynamic description. While the exponential UNP is predominantly in the hydrodynamic regime, heating at the central peak for low-density, high-electron temperature suggests significant local non-neutrality at early times.

This thesis presents the first observation of a shockwave in a UNP. The evolution of the density and velocity for exponential UNPs show signs of wave steepening. A significant density and velocity jump over a narrow region develops. These occur at the same location in the plasma. Additionally, a large spike in the ion temperature occurs at this front. The relative ion velocity across the front modestly surpasses the local sound speed.

The initial conditions were varied to characterize the development of shockwaves. Varying the density and electron temperature did not impact shock formation for the ranges used. Changing the shape caused the shocks to disappear as the density gradient decreased. This suggests that the electron thermal pressure gradient plays a significant

role in the shock formation. The establishment of shock formation in UNPs opens a new avenue of research for UNPs.

Acknowledgements

There have been many people who played a significant role in my graduate career. They all need acknowledgment and a heartfelt thank you. I cannot do this justice, but I will at least try. Traditionally, the acknowledgments begin with the graduate student thanking their Ph.D. advisor. However, Rice University is proud of their unconventional wisdom, and my graduate journey has been quite unconventional, to say the least. Not to minimize the role my advisor has played, but there are a couple of people who I need to thank first.

Truly, without the grace of God, I would not have finished my Ph.D. I can only offer a sacrifice of my heart in praise and thanksgiving in the Mass. Thank you to the many priests who have given me the Sacraments, especially the Eucharist, over the past eight years, and most especially since May 21, 2020.

Thank you to Stephanie for healing my broken brain. I would still be a severely traumatized non-functioning vegetable if it was not for your help. The transformation that I have undergone under your care is nothing shy of miraculous. This thesis would not have happened without you.

I would like to thank my advisor, Tom Killian. You met me where I was my first year and set me up to succeed, for which I cannot begin to express my gratitude. You always demand the best of me, and because of that I have grown more than I imagined possible. Thank you also for your heroic patience with me, especially after my accident. While this has not been the Ph.D. experience I wanted due to life interfering, you accommodated my limitations, never gave up on me, and helped me do excellent and groundbreaking science while overcoming C-PTSD. I cannot begin to express my gratitude for you and all that you did for me these past 8 years.

Thank you also to my lab partners, Grant Gorman and Nina Inmann. Grant, thank you for your teaching me all about ultracold neutral plasmas, coding, and running the experiment. I would be pretty lost without your help. Nina, thank you for helping me run the experiment. Your work on upgrading the apparatus and helping take data were invaluable. Thank you also to Soumya for helping out as a post-doc. We could not have made such timely progress without you, especially with debugging mysteriously broken equipment. I would also like to thank the other members of the Killian lab (past and present) - Thomas, Priyansh, Miriam, Caleb, and Bennett on the plasma experiment; Jim, Josh, and Brent from Neutral (now Tweezer); and Roger, Joe, Haad, Yi, and Chuanyu from Rydberg - for enlightening conversations and assisting me in the lab.

A special thanks to my two best friends - Alisa and Emily. Thank you for maintaining our friendship. Your unwavering support and encouragement means a lot to me. Thank you for forcing me to stop working and making me laugh until I can't breathe. You are always there for me, no matter how stressed and grumpy I can be. Y'all are incredible friends. I am very blessed to have you in my life. And, of course, thanks for the baby snuggles. :)

Thank you to my spiritual family at St. Vincent de Paul. Your support, encouragement, and intercession has meant a lot to me.

A heartfelt thanks to Fr. David, my spiritual father, without whom I would not have finished graduate school. Thank you for all that you have done to lead me closer to my Spouse and help me grow more into the saint God created me to be. Thank you for teaching me how to pray. Thank you for leading me deeper into the Mass through your own love for the Eucharist and great care in offering right worship.

One woman deserves an extremely profound thank you - my birth-mother Julie. Thank you for your courage and for choosing life. Literally I would not be here without you.

Finally, and most importantly, I would like to thank my family - my mom Cathy,

Deacon Daddy Doug, and my brother Zach - without whom none of this would have been possible. Thank you for always encouraging me to dream big and pursue those big dreams, even if it means living in Texas potentially for the rest of my life. Thank you for forming me into the woman I am today, and for always being my prayer warriors.

Contents

List of Figures

Chapter 1

Introduction

1.1 General Plasma Introduction

Plasmas are a soup of positively and negatively charged particles that often can be described as a gas [1]. Plasmas differ from ideal gases because the plasma particles - positively charged ions and negatively charged electrons - interact through the long-range Coulomb interaction, and thus interact with many neighbors simultaneously.

Plasmas are seen throughout the universe and are commonly known as the most abundant state of visible matter. Some astrophysical plasmas include solar plasmas [2], white dwarf stars [3], and nebulae [4]. Natural plasmas seen on Earth include the aurora and lightening. Plasmas are integrated into technology, like fluorescent lights, plasma televisions, and plasma etching. Plasmas are also used in Hall Effect Thrusters as fuel to launch satellites into space and to control their orbits once in space [5]. Plasmas are even used in medicine for wound care [6] and cancer treatment research [7]. Another key area of plasma application research is in achieving fusion as a clean energy source. Both inertial confinement fusion (ICF) reactors [8–10] and magnetic confinement fusion reactors [11, 12] promise to be clean energy sources, utilizing plasmas. In a recent major ICF breakthrough, more energy was produced than was put into the system [13].

1.2 Ultracold Neutral Plasma Introduction

Ultracold neutral plasmas (UNPs) are exotic plasmas that are created by photoionizing laser-cooled atoms just above the ionization threshold [14, 15] or excitation of atoms or molecules to Rydberg states, followed by collisional or autoionization [16–18]. The UNPs in this thesis are created through photoionization. UNP formation through Rydberg cascade will not be further discussed here.

UNPs are very cold ($\sim$1 K) and dilute with low initial densities on the order of $\sim 10^{14}$ m^{-3}. They are a powerful platform for studying plasma dynamics because they can be used to study hydrodynamic [19–22] or kinetic [23] effects, unmagnetized or magnetized plasmas [24–26], weak or strong coupling [27–29], and single ion species or mixtures [30, 31]. This has aided substantial work in theory and simulations [32–34].

UNPs have several advantages over hotter, denser plasmas. These include experimentally accessible timescales, excellent control over initial conditions, and precise diagnostics. For densities in dense astrophysical or laboratory systems, the inverse plasma frequency, which sets the timescale for the dynamics, is on the order of 10^{-15} s. These timescales are extremely difficult to probe. The low density in UNPs decreases the inverse ion plasma frequency by many orders of magnitude to a value of on the order of 10^{-6} s, which is very easy to measure and makes UNPs favorable for studying fundamental plasma physics.

Another advantage of UNPs is the excellent control over initial conditions and diagnostics, which utilize lasers. This provides robust and precise control over the density and electron temperature [35]. The density distribution can also be sculpted by changing the intensity distribution in the laser beam used to photoionize [21, 36, 37]. Additionally, Laser-Induced Fluorescence (LIF), which will be described in detail in Section 2.2,

provides precise measurements of ion density, temperature, and velocity with both temporal and spatial resolution [38]. The low densities used in UNPs are advantageous for LIF because they have a low optical density, making it easier to image the plasma. Using common experimental techniques in atomic physics also allows laser cooling or heating of ions in the plasma (even on just one axis) [29], spin tagging which is useful for measuring transport properties [27, 28, 39], and probing atomic states.

At the birth of the field of UNPs, they were of great interest because they can be used to study strong coupling, which is discussed in Section 1.3. Since then, they have also proven to be a powerful plasma simulator and have given rise to novel behavior. In this thesis, I focus on the use of UNPs as a plasma simulator and novel behavior seen in UNPs: namely the development and characterization of shockwaves.

1.3 Universality and Coulomb Coupling Parameter

One way to characterize plasma dynamics is through the strength of the Coulomb interaction given by the Coulomb coupling parameter Γ, which is the ratio of the Coulomb interaction energy to the thermal energy. For singly ionized particles, this is

$$\Gamma = \frac{e^2}{4\pi\epsilon_0 a k_B T} = \frac{e^2}{4\pi\epsilon_0 k_B T (4/3\pi n)^{1/3}}, \tag{1.1}$$

where e is the charge of an electron, ϵ_0 is the permittivity of free space, a is the Weigner-Seitz radius, k_B is the Boltzmann constant, T is the temperature, and n is the particle density.

When $\Gamma < 1$, the thermal energy is the dominant energy in the system and the plasma is in the weakly coupled regime. In this case, the Coulomb interaction can be treated as a perturbation. Traditionally, plasma physics works with systems with $\Gamma < 1$. Weakly

coupled plasmas have been extensively studied and are well described by analytic models [1, 40].

However, when $\Gamma > 1$, there is an inversion of the energy hierarchy as the Coulomb interaction energy becomes the dominant energy. This makes modeling the plasmas difficult because the Coulomb interaction is a long-range, many-body interaction. There has been a large focus on extending weakly coupled plasma theory into the strongly coupled regime [41–45]. Additional work has been done with molecular dynamics simulations [32, 46, 47]. Both the theory and simulation results need to be experimentally verified, thus studying strongly coupled plasmas in the lab is necessary for understanding the fundamental physics of strongly coupled plasmas.

Γ is significant because it is a universal parameter, meaning that plasmas with the same Γ exhibit the same physics, despite having densities and temperatures that could potentially differ by many orders of magnitude. This is illustrated in Fig. 1.1, which shows the $n - T$ phase diagram for different plasmas seen throughout the universe and in labs. The red line indicates $\Gamma = 1$. Plasmas along the same line have the same Γ, and are described by the same physics. The weakly coupled regime is above the red line and the strongly coupled regime is below. The universality of Γ allows for the use of a more experimentally convenient density and temperature over the densities and temperatures seen in nature while still allowing the same physics to be studied. UNPs, which straddle the weakly and strongly coupled regimes, are one such experimentally convenient plasma.

1.4 Fundamental Length and Time Scales

In addition to Γ, there are several important parameters in plasmas, especially length scales and time scales. These length scales and time scales determine the dynamics of the

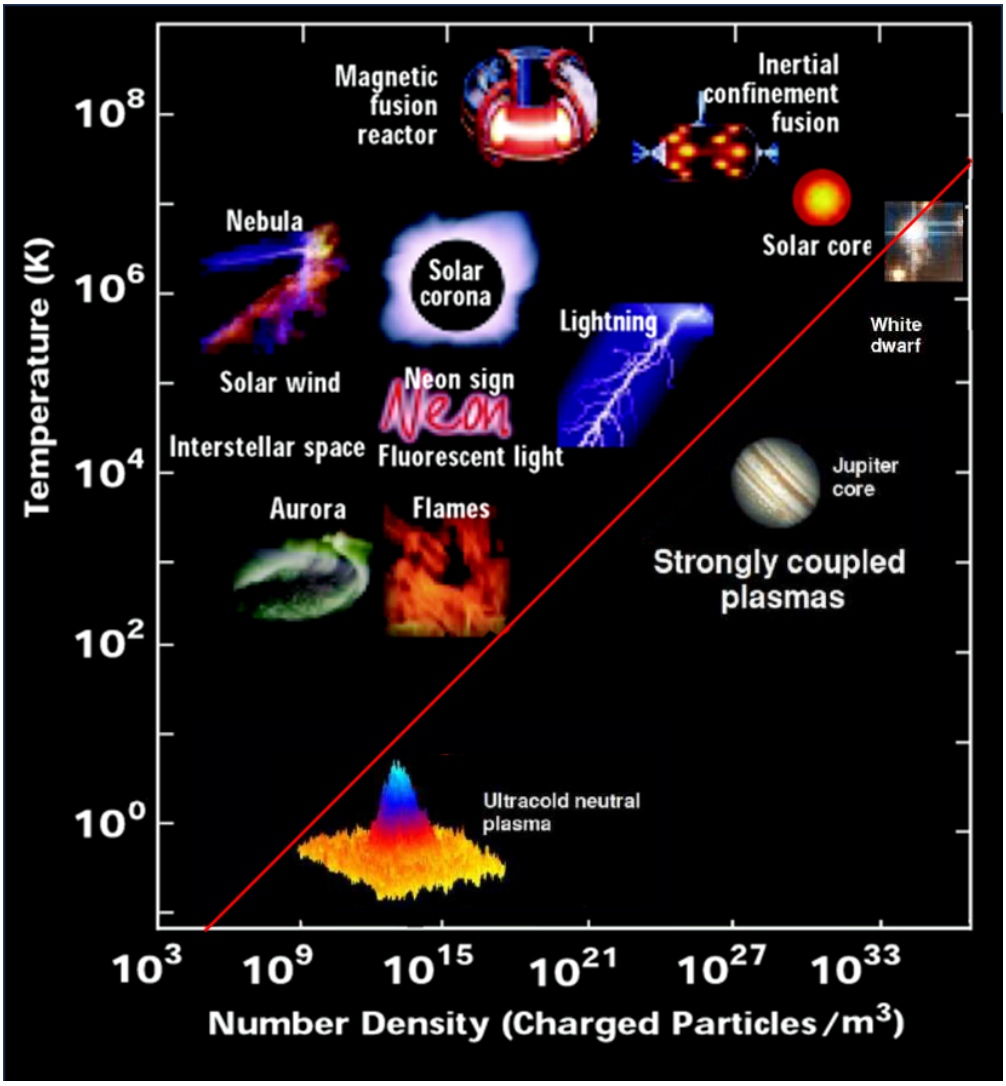

FIGURE 1.1: $n - T$ phase diagram with different plasmas. The red line indicates $\Gamma = 1$. Plasmas below the red line are in the the strongly coupled regime while plasmas above the line are weakly coupled. Adapted from [48].

plasma. Their relative sizes are also important and provide insight into the physics of the system.

1.4.1 Debye Length

Debye shielding is fundamental in plasma physics. In Debye shielding, electrons rearrange to shield electric fields from the ions [1, 49]. It leads to an interaction between two

ions given by

$$V_{ij}(r_i, r_j) = \frac{U_0}{r_{ij}} exp\bigg(- \frac{r_{ij}}{\lambda_D}\bigg), \tag{1.2}$$

where U_0 is the product of two charges and constants that depend on the unit system, $r_{ij} = |\vec{r_i} - \vec{r_j}|$, and λ_D is the Debye screening length. The Debye length is given by

$$\lambda_D = \sqrt{\frac{\epsilon_0 k_B T_e}{ne^2}}. \tag{1.3}$$

The Debye length only depends on the electron temperature and the density. The Debye length is significant because $\kappa = a/\lambda_D$, where a is the Weigner-Seitz radius, is a universal parameter that determines the dynamics [50]. If the Debye length is short, the ions strongly feel very few, close neighbors. This leads to dynamics dominated by large angle collisions. If the Debye length is large, the ions interact with a lot of neighbors who are further way, leading to weaker interactions and small angle collisions.

1.4.2 Mean Free Path

Another important length scale is the mean free path. The mean free path (MFP) describes the average distance that a particle travels before colliding with another particle, and is different for ion-ion, ion-electron, and electron-electron collisions. The MFP is important for determining transport rates. The MFP gives insight into whether kinetic effects are important or if the system is hydrodynamic. When the MFP is small compared to the length scale for density variation or other plasma parameters, the system can be described by hydrodynamic models. When the MFP is large, particles can stream significant distances, requiring a kinetic description.

The equation for the MFP is given by λ_{MFP} in Eqs. 1.4-1.7:

$$\lambda_{MFP} = v_{therm}/\nu \tag{1.4}$$

$$v_{therm} = \sqrt{\frac{k_B T}{m}} \tag{1.5}$$

$$\nu = 2\frac{e^4 \lambda n}{4\pi\epsilon_0^2 m v^3}\frac{2}{\sqrt{\pi}}\int_0^{x(v,T,m)} \sqrt{t}e^{-t}dt \tag{1.6}$$

$$\lambda = ln(1 + 0.4\Gamma^{-3/2}) \tag{1.7}$$

Γ is the Coulomb coupling parameter given in Eq. 1.1, v_{therm} is the thermal velocity, ν is the collision frequency, and λ is the Coulomb logarithm [23]. ν is calculated from statistical mechanics [51].

For an electron temperature of 160 K and a density of 15×10^{14} m^{-3}, the MFP for an electron moving with the thermal velocity is 2.4 mm. This is on the order of the initial plasma size, which is $\sim$1 mm in the experiments discussed in this thesis.

The MFP for an ion moving at the thermal velocity for 1 K and a typical density of 1×10^{14} m^{-3} is 28 μm, which is significantly smaller than the plasma size.

1.4.3 Plasma Size

One final significant length scale is the plasma size. This will be discussed in more detail in Section 3.2. The relative size of other length scales compared to the plasma size determines either their relevance or a certain regime. For example, if a density perturbation has a length scale that is 5% of the plasma size versus 50%, the dynamics and the treatment will be very different.

1.4.4 Plasma Oscillation

The fundamental timescale on which dynamics occur is the inverse plasma frequency, $\tau_{pi,e} = 2\pi/\omega_{pi,e}$, where the subscript i is for ions and e is for electrons. The plasma frequency is derived by displacing an electron or ion in a uniform slab of background plasma and calculating the frequency of oscillation due to the Coulomb force [1]. The plasma frequency is given by

$$\omega_{pi,e} = \sqrt{\frac{n_{i,e}e^2}{m_{i,e}\epsilon_0}}, \tag{1.8}$$

where n is the density, e is the elementary charge, m is the mass, and ϵ_0 is the vacuum permittivity. For the densities in the experiments discussed in this thesis, $\tau_{pe} \sim 1$ ns and $\tau_{pi} \sim 1\,\mu$s. For singly-ionized strontium ions in a quasi-neutral plasma ($n_i \sim n_e$), $\tau_{pi} = 400\tau_{pe}$.

1.4.5 Collision Rate

The collision rate sets the rate at which equilibration occurs. This is given in Eq. 1.6. If the collision rate is large compared to the expansion rate, the plasma can attain local, if not global, thermal equilibrium. For UNPs, because the electron MFP and the collision rate are both large, the electrons are in global thermal equilibrium. However, the ions are only in local thermal equilibrium.

1.4.6 Expansion Time

The final time scale is the expansion time. This sets the lifetime of the plasma. In order to study different plasma phenomena, they must occur faster than the plasma expands. This will also be discussed in greater detail in Section 3.2, but the plasma expansion time

plays a critical role in the hierarchy of length and time scales, and is significant in the work presented in this thesis [19]. For the plasmas studied in this thesis, this timescale is $\sim 1 - 10\,\mu$s.

1.5 Life of an Ultracold Neutral Plasma

The life of a UNP consists of three main phases: electron equilibration, local ion equilibration, and plasma expansion.

1.5.1 Electron Equilibration

In the first few hundred nanoseconds, the electrons equilibrate. During this early time in the plasma life, some of the electrons escape until enough positive charge builds up to create a deep enough energy well to trap the remaining electrons [14]. This leads to quasi-neutrality with about 95% of the electrons remaining.

For the electrons, the mean free path is on the order of the plasma size. Because of this, the electrons are in global thermal equilibrium, and remain in global thermal equilibrium throughout the entire plasma expansion [52, 53].

1.5.2 Disorder Induced Heating

Due to excess Coulomb energy due to initially uncorrelated positions, the ions undergo a process called disorder-induced heating (DIH) which converts the excess Coulomb energy into thermal energy through kinetic energy oscillations [39, 54]. DIH occurs in the first couple of microseconds after photoionization. While the atoms in the trap are approximately 10 mK, during DIH, the ions heat to on the order of 1 K, depending on the density. The ion DIH temperature, T_{DIH} is given by

$$T_{DIH} = \frac{2}{3}\frac{e^2}{4\pi\epsilon_0 a k_B}|\tilde{U} + \kappa/2|, \tag{1.9}$$

where ϵ_0 is the permittivity of free space, k_B is the Boltzmann constant, and $a = (4/3\pi n_i)^{1/3}$ is the Wigner-Seitz radius. $\kappa = a/\lambda_D$, where λ_D is the Debye length (Eq. 1.3). $\tilde{U}$ is the Coulomb energy per particle and has been tabulated in [55]. Given n_i and T_e, T_{DIH} is calculated numerically and the tabulated values of $\tilde{U}$ [39]. Additionally, the kinetic energy oscillations can be used to calibrate the density in the plasma [50].

DIH is unfortunate because it limits experiments to $\Gamma \lesssim 3$ without interventions to either order the atoms before photoionization [54, 56, 57] or removing heat after DIH [29].

In the experiments in this thesis, $T_e(0) \geq 60$ K. DIH only adds ~ 1 K to the temperature, so DIH does not significantly contribute to the electron temperature.

1.5.3 Expansion

The final stage of the UNP life is the plasma expansion. This lasts on the order of tens of microseconds, making it the longest stage of the plasma life. Depending on the initial conditions or experimental interventions, different phenomena can be studied or different transport properties measured. Sculpting the density distribution has allowed the exploration of new phenomena [21, 23, 36]. Laser cooling the ions has allowed access to a wider range of Γ [29]. Different density distributions can be created to see different phenomena [21, 23]. This is what makes UNPs such powerful platforms for studying plasma physics: they give rise to new phenomena and are excellent plasma simulators.

In this thesis, the expansion of a UNP with an initial exponentially decaying density distribution is studied. This novel density distribution gives rise to shockwaves - the first observation of shockwaves in UNPs. The investigation and characterization of shockwaves in UNPs is also described in this thesis.

Chapter 2

Experimental Set Up and Upgrades

This chapter contains two main sections. The first describes the experimental apparatus and the second details upgrades that are relevant to the work described here. The experimental apparatus section is intended for the general reader while the upgrades section documents different elements of the apparatus for future students' reference. There is considerably more detail about the upgrades in various appendices.

2.1 Experimental Apparatus

All of the experiments are done in an ultra-high vacuum chamber. To form UNPs, strontium atoms are heated and sublimate to create an atomic vapor. Atoms stream through a nozzle. Immediately after the nozzle is a 2D collimator, which is made of a beam of 461 nm light that passes through the chamber twice forming an "X," and is retro-reflected back onto itself. This serves to push the atoms back toward the center of the atomic beam, decreasing the divergence of the beam and minimizing the loss of atoms that hit the wall of the vacuum chamber. After the 2D collimator, the atomic beam passes through the Zeeman slower, which consists of a magnetic field with a gradient and a 461 nm laser beam that is propagating in the direction opposite the Sr beam. The Zeeman slower slows the atoms down to nearly a stop when they reach the main chamber where the experiments

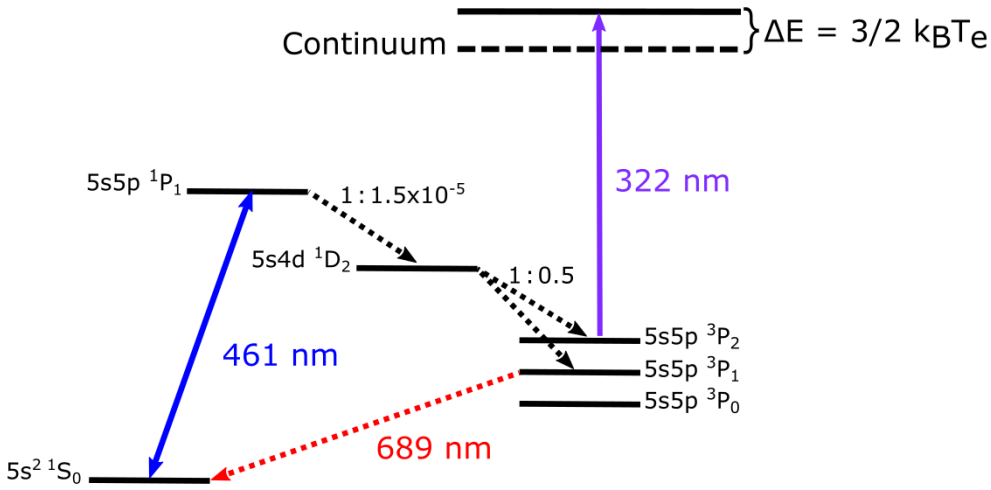

FIGURE 2.1: Level diagram for ^{8}8Sr. The atoms are laser cooled and trapped using the $5s^{1}\,{}^{1}S_0$ - $5s5p\,{}^{1}P_1$ transition with 461 nm light. Some of the atoms decay into the metastable dark $5s5p\,{}^{3}P_2$ state where they can be trapped in a purely magnetic trap. The atoms in the magnetic trap are photoionized using a 10 ns pulse of 322 nm light, forming the plasma. The electron temperature is determined by how far above the ionization threshold the 322 nm laser is detuned. From [59]

are conducted. The magnetic field gradient in the Zeeman slower is designed so that the Zeeman shift counteracts the change in the Doppler shift to keep the atoms on resonance with the laser beam as they slow down [58].

In the main chamber, atoms slowed by the Zeeman slower are loaded into a magneto-optical trap, or a MOT. A MOT uses three pairs of mutually perpendicular counter-propagating laser beams and a quadrupole magnetic field to laser cool and trap a cloud of atoms in the vacuum chamber. The atoms are cooled using the ${}^{1}S_0 - {}^{1}P_1$ transition with 461 nm light, as illustrated in Fig. 2.1. Some of the atoms decay into the metastable dark ${}^{3}P_2$ state. Atoms that decay into the ${}^{3}P_2$, $m_J = +2, +1$ states are then trapped in a purely magnetic trap, unless an additional laser is used to re-pump those atoms [60]. In the experiments described in this thesis, we do not re-pump the atoms out of the magnetic trap.

In previous experiments, the atoms were trapped in a MOT and photoionized using a two-photon ionization scheme [27, 61]. The plasma inherits its density profile from the atoms. For atoms in a MOT, this is given by a Gaussian $n(\vec{r}, t = 0) = n_0 exp\left[-\frac{r^2}{2\sigma_0^2}\right]$, where σ_0 characterizes the size of the density distribution. UNPs with an initial Gaussian density distribution have been extensively studied and are well-understood [19]. The expansion of a Gaussian UNP will be discussed in more detail in Section 3.2. This is used to compare the expansion of the novel density distribution studied in this thesis: a density distribution that decays exponentially from the center of the plasma, or an exponential plasma.

In the experiments in this thesis, exponential plasmas are created by photoionizing the atoms in the purely magnetic trap. The exponentially decaying density distribution $n(\vec{r}) = n_0 exp[-U_Z/k_B T]$ comes from the Zeeman shift $U_Z = \mu_B m_J g_l B$ of the $^3P_2$ state, where μ_B is the Bohr magneton, m_J is the projection of the total angular momentum, and $g_l = 1 + \frac{j(j+1)+s(s+1)-l(l+1)}{2j(j+1)}$ is the Lande g-factor. in g_l, j is the total angular momentum quantum number, s is the spin quantum number, and l is the orbital angular momentum quantum number. Near the center of the trap, the magnetic field can be approximated as linear by $|B| = b\sqrt{x^2 + y^2/4 + z^2/4}$, where b = 115 G/cm is the slope of the magnetic field. This gives an atomic density distribution in the magnetic trap that exponentially decays radially from the center of the trap given by [62]

$$n(\vec{r}) = n_0 exp\left[-\frac{8\mu_B b\sqrt{x^2 + \frac{y^2}{4} + \frac{z^2}{4}}}{3k_B T}\right] = n_0 exp\left[-\frac{\sqrt{x^2 + \frac{y^2}{4} + \frac{z^2}{4}}}{\sigma_0}\right]. \tag{2.1}$$

To make the plasma, typically the magnetic field and MOT lasers are turned off, and the atoms are photoionized with a 10 nm pulse of 322 nm light. The laser detuning above the ionization threshold determines the electron temperature. Low temperatures are avoided to mitigate three-body recombination [63, 64]. Ballistic expansion of the atoms

before photoionization can be important if the delay between turning off the magnetic field and ionizing is too long. This will be discussed in Section 5.3.2.

The general evolution of a plasma after photoionization is described in Sec. 1.5. At different times throughout the plasma expansion, the ions are imaged using the powerful technique of Laser-Induced Fluorescence, which is described in Sec. 2.2.

2.2 Imaging Using Laser Induced Fluorescence

Laser-Induced Fluorescence (LIF) is a powerful form of spectroscopy used to image the ions in the plasma [38]. Figure 2.2 shows (A) the $^{88}Sr^{+}$ level diagram for imaging, (B) experimental set up, (C) sample false-color density plot, and (D) sample spectrum at the center of the plasma.

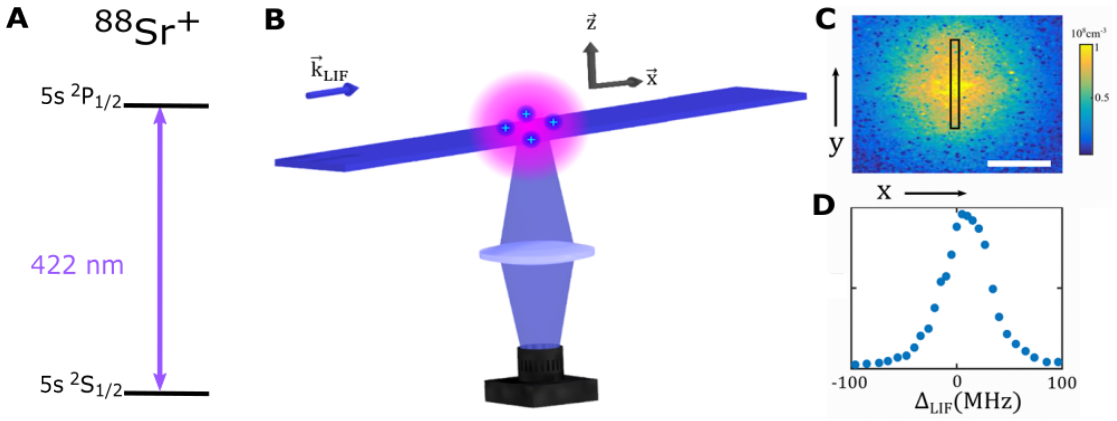

FIGURE 2.2: Diagram of the experimental set up. (A) Energy level diagram for $^{88}Sr^{+}$. The ions are imaged using the $5s\,^2S_{1/2} - 5p\,^2P_{1/2}$ transition at 422 nm. (B) Diagram of the imaging system. A thin 1 mm sheet of 422 nm light passes through the center of the plasma. The fluorescence light is imaged using a 1:1 optical relay and collected on an intensified CCD camera. (C) A sample false-color image of the plasma density. (D) A sample spectrum taken from the black box in (C). From [59]

In the experiments in this thesis, a thin 1 mm sheet of linearly polarized 422 nm light illuminates the central xy-plane of the plasma, as shown in Fig. 2.2B. The Sr^{+} ions are

probed on the $5s\,^2S_{1/2} - 5p\,^2P_{1/2}$ transition at adjustable times after photoionization, as shown by Fig. 2.2A. The fluorescence signal along the negative z-axis is collected on an intensified CCD camera using a 1:1 optical relay. This gives temporally and spatially resolved spectra. From the spectra, we extract the density, velocity, and temperature of the ions. Figure 2.2C shows an example of a false-color image of the ion density.

In an unmagnetized and locally thermalized UNP, the local spectra consist of a single peak that is characterized by a Voigt profile, given by [38]

$$F(\nu,x,y) = C\frac{\gamma_0}{2}\int dz n_i(\mathbf{r})\frac{I(\mathbf{r})}{I_{sat}}\int ds \frac{\gamma_0/\gamma_{eff}}{1+\left[\frac{2(\nu-s)}{\gamma_{eff}/2\pi}\right]^2}\times\frac{1}{\sqrt{2\pi}\sigma_D[T_i(\mathbf{r})]}exp\left\{-\frac{[s-(\nu_0+\nu_{exp}(\mathbf{r}))]^2}{2\sigma_D^2[T_i(\mathbf{r})]}\right\}. \tag{2.2}$$

A sample spectrum is shown in Fig. 2.2D. The fluorescence depends on the ion density $n_i(\mathbf{r})$, the intensity of the laser $I(\mathbf{r})$, the saturation intensity of the transition I_{sat}, the natural linewidth of the transition γ_0, the effective linewidth $\gamma_{eff} = \gamma_0 + \gamma_{las}$ where γ_{las} is the linewidth of the imaging laser, and the Voigt profile. C is a constant that takes into account the solid angle, the dipole radiation pattern, and the efficiency of the CCD camera. It is calibrated through measuring DIH curves [50].

The Voigt profile is the convolution of the single-atom Lorentzian lineshape with a Gaussian that describes the velocity distribution of the localized system. Since the laser in our experiment does not saturate the transition, we do not include power broadening. The horizontal shift of the Gaussian is given by the unperturbed resonance frequency of the transition ν_0 and the Doppler shift due to the expansion velocity parallel to the laser propagation ν_{exp}. In the experiments in this thesis, the laser only propagates along the x-axis, which is the axis of symmetry for the MOT. The width of the Gaussian depends on the ion temperature and is given by the Doppler broadening due to the random thermal

motion:

$$\sigma_D[T_i(\mathbf{r})] = \frac{\sqrt{k_B T_i/m_i}}{\lambda}. \tag{2.3}$$

The ion temperature, expansion velocity, and ion density are measured by fitting the local spectra with Eq. 2.2. The velocity is determined by how far the laser is detuned from resonance. The ion temperature is given by Eq. 2.3. Integrating the spectrum over frequency gives the density. The temperature, velocity, and density can vary spatially, but we work with small enough regions that the variations within an analysis region can typically be ignored. Section 4.7 explores in detail the cases where this assumption is invalid.

2.3 System Upgrades

2.3.1 922 system

To laser cool and trap Sr atoms, we frequency double a 922 nm laser beam to make 461 nm light. We have two doubling cavities - one for the MOT and another for the Zeeman slower. Some of the light from the MOT is used in a saturated absorption (SatAbs) cell to lock the frequency of the 922 nm laser so that the MOT beam is on resonance with Sr atoms [58].

The most important laser in the UNP experiment is the 922 nm laser. The other laser systems depend on the 922 laser. There are two transfer cavities that are used to stabilize the other lasers relative to the 922. The first is the 844 transfer cavity, which is actually called the "transfer cavity." The second is the transfer cavity that controls the 408, 1033, and 1092 nm lasers, which is the "superlock." The Toptica 408 nm diode is actually an 816

nm diode that is frequency doubled in the laser box into 408 nm. It includes an 816 nm test beam that is sent into the superlock, so everything in the superlock is IR.

The 844 nm laser is frequency doubled to 422 nm, and is used in LIF. The 408 nm laser is used to laser cool the ions [29], and is not used in the experiments described in this thesis. The 1033 and 1092 nm lasers are used to re-pump the ions out of metastable dark states. They are not used in the experiments in this thesis. They are necessary for laser cooling when the ions are exposed to lasers for much longer, and so a significant number of ions are pumped into dark states.

MOTsitter

The MOT doubling cavity lock is very sensitive and regularly comes unlocked. When it unlocks, it needs to be relocked immediately or we have to throw away the data. It is particularly fond of unlocking near the end of a very long data set, especially if it's late at night and is the last data set for the day. It is hard to do everything else that needs to be done while taking data if you're just staring at the optical table waiting for the MOT to unlock. To solve this issue, I created the MOTsitter that sets off an alarm when the photodiode voltage used to lock the MOT drops below an adjustable threshold. It can detect when the MOT is unstable and about to unlock.

The MOTsitter was designed to be get students' attention when the MOT comes unlocked. This has a twofold purpose: 1) preventing us from having to throw out datasets where the MOT unlocks 45 minutes into the scan and 2) allowing us to work while taking data rather than watching the oscilloscope with the MOT beam signal.

Figure 2.3 shows the circuit diagram. A hard copy is taped on the inside of the lid. The digital copy is saved on the Drobo under Plasma, circuits, MOTsitter. The box has three inputs: MOT input, +18 V, and –18 V. The ±18 V powers the voltage regulators which

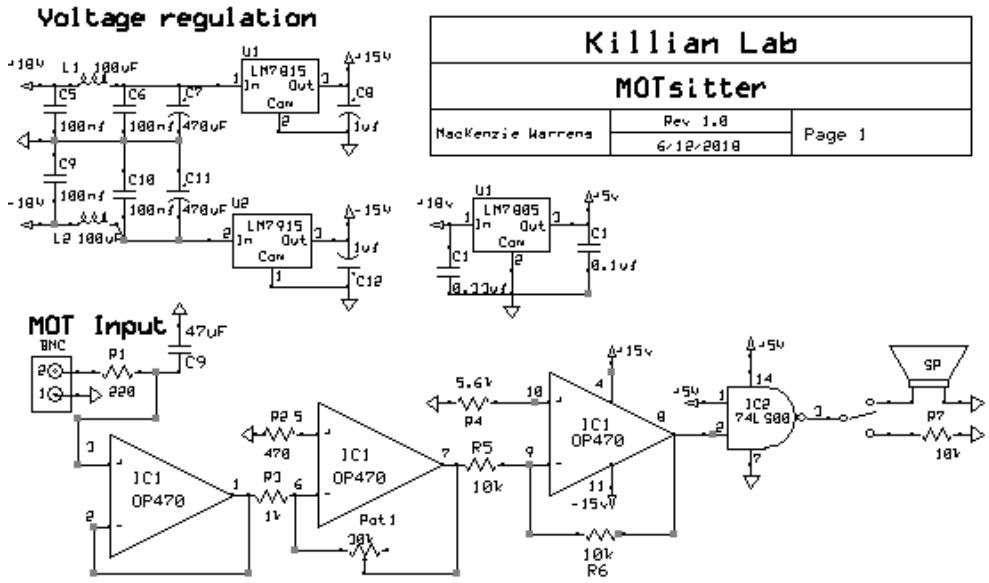

FIGURE 2.3: The circuit diagram for the MOTsitter, which sounds an alarm when the doubling cavity for the MOT beam starts to unlock.

output ±15 V. The ±15 V power the OP470, and the +15 V is used for the +5 V voltage regulator. The +5 V powers the 74LS00 and is one of the inputs for the NAND gate.

The circuit essentially consists of three stages: a low pass filter, an amplification stage, and a logic gate. The idea behind the circuit is to amplify the MOT signal so that when the laser is locked, the NAND gate sees a high and when it is unlocked, the NAND gate sees a low. When both inputs to the NAND gate are high, the output is low and the buzzer is quiet. When one input is low, the output is high, and the buzzer sounds an alarm.

MOT Autorelocker

We continued to have a lot of problems with the MOT lock being extremely sensitive to vibrations and frequently unlocking, so we replaced the lock with an autorelocker, removing the need for the MOTsitter and the graduate student needing to manually relock it every time it unlocks. This circuit was built by Priyansh Lunia. This circuit is fast enough to relock the MOT cavity before the SatAbs unlocks, which is essential. Once the

SatAbs unlocks, the experiment has to be stopped and any data taken in that scan has to be thrown out. This circuit is described in significantly more detail, including circuit diagrams and PCB traces, in Appendix A.

New 922 nm Diode Laser

The original laser used to laser cool and trap strontium atoms on this experiment was a Ti:Sapphire pumped by a Coherent Verdi. Unfortunately after 20 years, Coherent stopped supporting this laser and it died a slow, painful death. Before its decline, the Ti:Sapphire laser output 845 mW of 922 nm light. We replaced this system with a Toptica TA Pro 922 nm diode, which we refer to as the Toptica 922. It has a FiberDock which is a fiber output. Without the fiber, the laser should output 3.5 W at full power, and 1.6 W through the fiber.

If the internal alignment is off, the power will be low. Toptica sent a video that demonstrates how to peak up the laser alignment.

Current Lock for Topitca 922 nm Laser

With the Toptica 922, high frequency noise was preventing the MOT and Zeeman doubling cavities from staying locked. The normal autorelocker was not fast enough. With the Toptica 922, we not only have control over the PZT on the doubling cavity, but we also have much faster control over the diode current. To silence some of the noise, I added a current lock. Figure 2.4 shows the bode plot with the error gain set to where the lock is optimized.

2.3.2 422 Imaging System Upgrade

Our imaging system has been degrading over time. The 422 nm laser power is not stable and is not what is used to be. We want more power and need better stability. To achieve

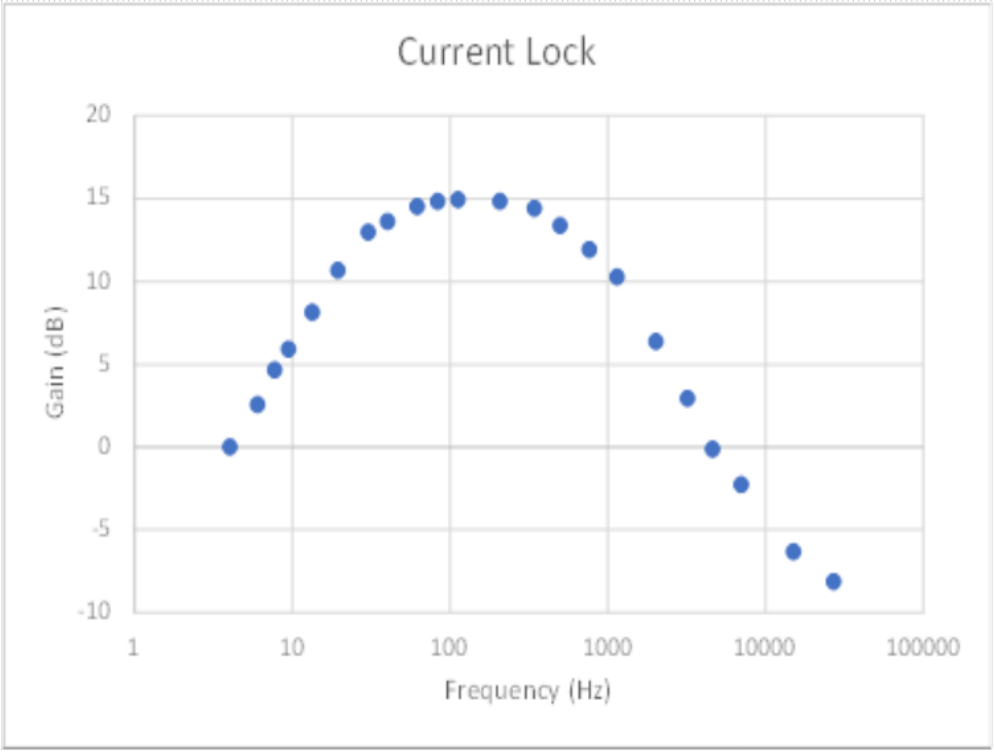

FIGURE 2.4: The bode plot for the Toptica 922 diode laser current lock.

this, we upgraded our imaging system. We are still using the Toptica 844 diode head, but we upgraded the TA and SHG. Instead of using a doubling cavity, the SHG is a single-pass fiber input and free-space output SHG from AdvR. This upgrade was done after the experiments for this thesis were completed. The old TA and bow-tie doubling cavity were used for this thesis.

Transfer Cavity Upgrade

To stabilize the 844 nm laser, which is frequency doubled to 422 nm, a small amount of 844 nm light and 922 nm light are injected into a Fabry-Perot cavity. The cavity is locked to the 922 nm beam so that the 922 nm beam is at a fixed voltage when ramping the cavity length. The 844 nm beam is locked relative to the 922 nm beam. The scan range of the 422 is limited to the free spectral range (FSR) of the cavity, given by

$$\nu_{FSR} = \frac{c}{2L}, \tag{2.4}$$

where c is the speed of light and L is the cavity length. Since the 422 nm laser probes the ions over a wide range of velocities, this is potentially limiting. With the original transfer cavity, we could only image ions over about 1.4 GHz for 422 nm, which is about 700 MHz in 844 nm. In the shockwave experiments, the detuning range needed to image the ions far exceeded 1.4 GHz, which forced us to either take multiple data sets and stitch them together for the same plasma expansion time, or upgrade the cavity to one with a significantly larger FSR. We tried taking multiple sets with different detuning ranges, but stitching them together did not work, so Nina Inman upgraded the cavity to a Thorlabs cavity with a 3 GHz FSR in 844 nm. This is 6 GHz in 422 nm. We were able to scan the 422 nm beam 3.4 GHz (or 1.7 GHz in 844) before we were limited by the mode-hop free range of the laser itself. This range was sufficient to image all of the ions in the plasmas for the different experiments.

Included in the upgrade was replacing the home-built analog cavity lock with a digital LabVIEW lock.

422 Current Lock

Similar to the 922 Topitca diode, when we upgraded the transfer cavity, we ran into issues with the new digital lock being too slow, causing the doubling cavity to unlock. I added a current lock to the 844 which helped with the speed and stability issues.

2.3.3 New Atom Source Heater Coil

Figure 2.5 shows the atom source. It consists of two main parts: the flange with the fire rod and feedthrough (left through center), and the nozzle (right). The flange connects

the atom source to the vacuum chamber. The fire rods are in the tube that is fixed to the flange. They heat the strontium so it sublimates, creating the free atoms that flow through a small hole in the nozzle. The tip of the nozzle is far from the fire rod, creating a thermal gradient that allows the atoms to stick inside the nozzle hole and clog the nozzle. To prevent clogging, the nozzle is wrapped with UHV-compatible heater wire. After many years of continual use, the heater wire failed and the nozzle clogged, requiring us to fix it. This is described in detail in Appendices A.0.1 and A.1.

FIGURE 2.5: The strontium source removed from the vacuum chamber. There are three screws holding the nozzle to the rest of the device. The fire rod which heat up the strontium are near the back of the device, creating a thermal gradient with a cooler tip. The tip of the nozzle is wrapped with heater wire to prevent strontium atoms from sticking to the cooler nozzle hole and clogging it. A clamp prevents the coil from unwinding.

2.3.4 Temperature and Humidity Logger

We had issues with humidity and temperature stability. Lasers operate best under stable conditions, especially where the index of refraction remains constant. When the humidity and temperature fluctuate, especially when the humidity suddenly drops ∼30%, the laser performance is greatly hindered. This causes substantial valuable time to be lost. If the laser beam paths are realigned (a several-hour process), they have to be realigned again when the humidity and temperature return to their normal values. I created a temperature and humidity logger using an Arduino to monitor, record, and display the temperature and humidity data so we know if there is a problem with the lasers or with the environment.

There are two different sensors - one near the oven and one near the 422 temperature controller. The circuit measures the humidity and temperature every 10 minutes, records the date, time, humidity, and temperature on a micro SD card, and displays the most recent humidity and temperature readings on an LCD.

A detailed description including how to build the logger can be found in Appendix B.

Sample Humidity and Temperature Data

Figure 2.6 shows the humidity data and Fig. 2.7 shows the corresponding temperature data for March 14-16, 2023. During this time, the temperature and humidity for the entire building dropped significantly due to a facilities issue. This is clearly shown in the data where the temperature suddenly drops about 2 F midway through March 14 and slowly increases the rest of the day, re-stabilizing late that night. The humidity responds much slower, taking several hours to drop to the minimum, with a change of about 25-30% - a massive change that significantly changes the index of refraction of air and changes the alignment of the lasers (as well as the overall performance, *i.e.* major decreased power).

Unlike the temperature which took about half a day to re-stabilize, the humidity quickly increases over about an hour. However, the humidity overshoots and remains high for almost an entire day before returning to the value before the incident.

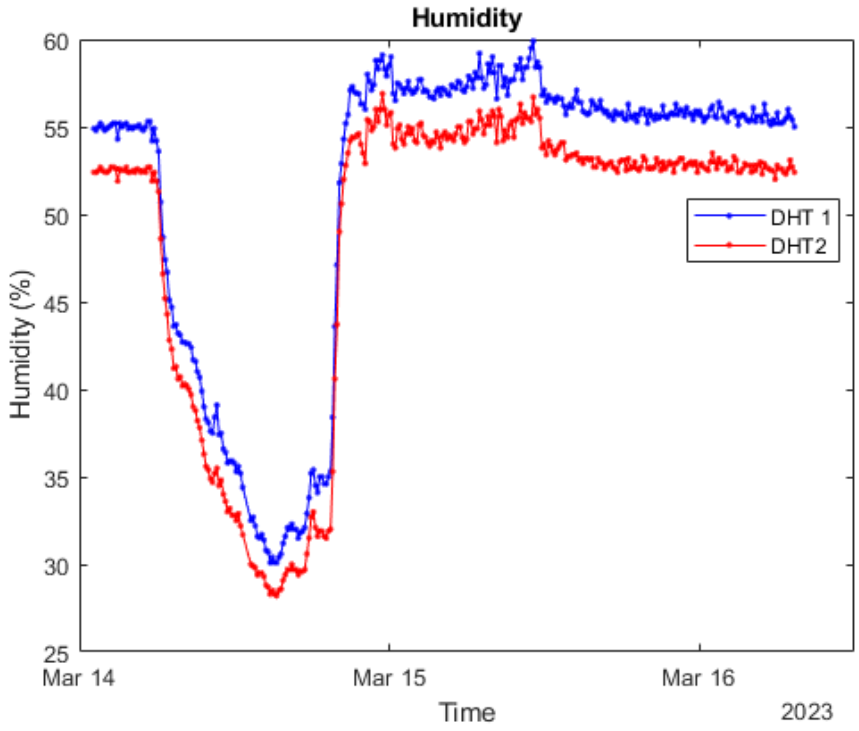

FIGURE 2.6: A sample of the humidity data for the Temperature and Humidity Logger. The humidity for the entire building dropped significantly due to an issue with the steam. The Temperature and Humidity logger is quite effective.

The two sensors differ from each other by a small offset - about 0.25 F and about 3% humidity. However, we are not interested in precision measurements of the exact values of the temperature and humidity. The purpose of this device is to see the general trend of what is happening with the temperature and humidity and how it changes with time.

Another aspect of the data that may raise questions is the oscillations, especially on the temperature. The temperature does indeed oscillate about 0.5 F, but that is not enough

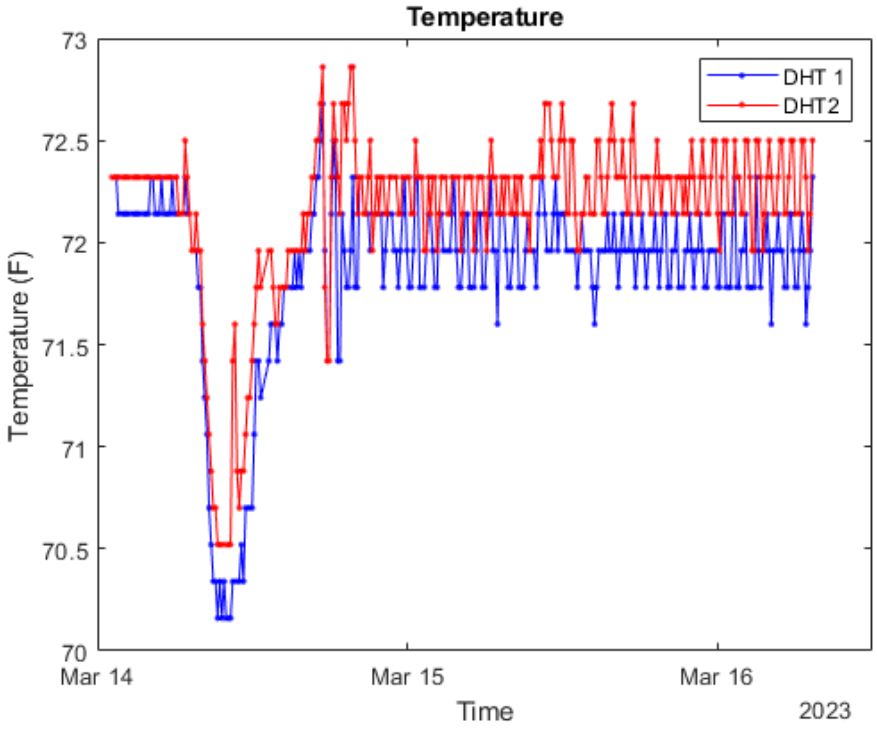

FIGURE 2.7: A sample of the temperature data for the Temperature and Humidity Logger for the same incident described in Fig. 2.6.

to impact the performance of our equipment. Problems arise with significant changes, especially in the humidity.

This data demonstrates that the temperature and humidity logger works as intended.

Temperature and Humidity Logger Future Work

It would be nice if the Arduino was also capable of sending some kind of signal to let us know when the humidity and temperature are out of range as well as when it is restored. It could be as simple as using text on the LCD, using a green LED when it is in range and a red LED when it is out of range, or having an alarm literally sound when it is out of range. The auditory might be better than the visual because we likely will not look at the box regularly. However, the auditory would be extremely annoying, especially for a

prolonged issue, so it will undoubtedly be unplugged with a high probability of being forgotten about and not plugged back in. A more expensive and complex upgrade would be to connect the Arduino to the internet and have it email or text the lab members when the temperature and humidity are out of range and/or restored.

2.3.5 Future Upgrades

Replacing Ion Pumps

The vacuum has been degrading over the years. It is still functional for what we were doing, but it is time for the ion pumps to be replaced and the ion pump controller to be upgraded. It is thought that the ion pumps are the original ion pumps, so they are approximately 25 years old, which is well beyond the expected lifetime of an ion pump. Before breaking vacuum, they can be "high-potted" to try to remove any whiskers that have built up on the electrodes over the years, which will buy some more time, but will also temporarily cause an increase in pressure as matter is expelled from the electrodes and is recaptured. The process for high-potting is described in ion pump manuals.

Replacing Optics

To make the magnetic fields required to trap the atoms, 80 A of current is run through two coils. That much current heats up the wire, so in order to mitigate the risk of ruining the coils or causing a fire, the coils are water-cooled with water at about 80 PSI. The water connects to the coils on the corner of our optical table that is closest to the vacuum chamber. In the 2017-2018 academic year, there was a flood in the lab caused by a failure in the connection, leading to a hose freely spraying water at 80 PSI. Dirty water contaminated most of the optics in that region of the table, including the windows on the vacuum chamber. While the students were diligent in cleaning up and trying to care for the optics, there

are nonetheless water marks on some of the optics. Since this incident, we have not been able to reach the densities that were achieved before The Flood, likely due to water marks impacting the MOT beam and the 2D collimator. Since it has not impacted the experiment to the point that we needed to break vacuum to replace the windows and replace other precisely placed optics that are not very accessible, we have continued research with the water spots. However, it would be nice to replace the windows on the vacuum chamber.

New Ionization Beam

The year before I arrived, the ionization beam was upgraded to a Continuum Surelite II Nd:YAG and ND6000 dye laser that we acquired from a professor who was retiring. While it is more powerful than the previous laser, the power is not uniformly distributed. We attribute the asymmetries we see in our plasma to the ionization beam's unique profile, especially because we do not think we fully ionize our plasma, even with eight passes of the beam. We would like to fully ionize the plasma so we can work at higher densities, which would require a more powerful laser. Additionally, the donated laser is having issues with burn marks on the dye cells, which we cannot replace because the parts are obsolete. This is impacting both the power and the distribution, which in turn impacts the densities that we can attain.

To solve these problems we got a new Quanta Ray Pro 250 Nd:YAG and Cobra Stretch Dye Laser that I have nicknamed the Death Laser because it is so powerful that we assume anything in the beam's way that isn't supposed to be there will be destroyed. An excellent upgrade to the system would be integrating the Death Laser into the experiment. This will require the construction of a beam shield around the table for safety reasons and likely some other modifications to make working on the optical table both safe and feasible.

New Current Source

The original current source is able to supply 80 A, which provides respectably strong magnetic fields. However, we want to do experiments with higher currents for a couple reasons. First, we would like to increase the cuspiness of the plasma. Since the size of the atomic cloud in the magnetic trap (and consequently also the plasma) is inversely proportional to the magnetic field gradient, increasing the current will increase the cuspiness of the plasma. Second, we would like to have stronger magnetic fields to trap the plasma, building on the magnetic confinement experiment in [24]. In the second instance, we would like to trap the atoms at lower current and then briefly increase the current to ~ 400 A.

Chapter 3

Hydrodynamic Expansion of an Exponential UNP

This chapter is drawn from [22] and [59].

3.1 Hydrodynamics

When the mean free path of particles is short relative to the system size, the system is collisional and can be treated as a fluid that ignores individual particles. In this regime, magnetohydrodynamics (MHD) is valid. In MHD, each species is treated as a separate fluid with its own equation of motion. The different species are coupled through the electric field and collisions. Fluid models assume that particles are in local thermal equilibrium with a temperature for each species.

Hydrodynamic theories can be derived from kinetic treatments, which track the evolution of phase space distributions and do not assume local thermal equilibrium. When tracking phase space densities is insufficient, and when individual particle trajectories and interactions must be followed, computationally expensive molecular dynamics simulations must be used.

Ultracold neutral plasmas are well described by MHD. Sometimes a UNP can be predominantly hydrodynamic but can have some kinetic effects like streaming plasmas, depending on the conditions. In past experiments, these effects have been seen using techniqus that sculpt the plasma's initial density distribution [21, 36, 37, 65]. For the experiments described in this thesis, UNPs are in the hydrodynamic regime with some discussion of possible kinetic effects. This will be shown later in this chapter. Collisions are ignored. UNPs studied here are two-component unmagnetized plasmas with Sr+ ions and electrons, each with separate equations of motion given by

$$\begin{aligned} n_e m_e \dot{\vec{v}}_e + e n_e \vec{E} &= -\vec{\nabla} P_e \\ n_i m_i \dot{\vec{v}}_i - e n_i \vec{E} &= -\vec{\nabla} P_i, \end{aligned} \tag{3.1}$$

where $\dot{\vec{v}} = \frac{d\vec{v}}{dt} = \vec{v} \cdot \vec{\nabla}\vec{v} + \frac{\partial \vec{v}}{\partial t}$ and $\vec{\nabla} P_{i,e} = \vec{\nabla}(n_{i,e} k_B T_{i,e})$ [1]. For low-temperature quasi-neutral plasmas it is a reasonable first approximation to assume $n_i \approx n_e = n$ and $v_i \approx v_e = v$. Equations 3.1 become

$$\begin{aligned} n m_e \dot{\vec{v}} + e n \vec{E} &= -\vec{\nabla}(n k_B T_e) \\ n m_i \dot{\vec{v}} - e n \vec{E} &= -\vec{\nabla}(n k_B T_i), \end{aligned} \tag{3.2}$$

which are added together to give

$$(m_e + m_i) n \dot{\vec{v}} = -\vec{\nabla}\big[n k_B (T_e + T_i)\big]. \tag{3.3}$$

Since $m_e \ll m_i$, we can approximate $m_e \approx 0$. In our experiments, we use $T_e \geq 40$ K, primarily to avoid recombination, but also because at higher T_e we see more interesting effects that will be discussed in greater depth in Chapter 5. Likewise, since $T_i \ll T_e$, $T_i \approx 0$. Eq. 3.3 becomes

$$m_i n \dot{\vec{v}} = -\vec{\nabla}(n k_B T_e). \tag{3.4}$$

Because the mean free path of the electrons is larger than the plasma size, the electrons are in global thermal equilibrium, so $\vec{\nabla} T_e = 0$ and Eq. 3.4 can be rewritten as

$$\dot{\vec{v}}_{exp} = -\frac{k_B T_e}{m_i} \frac{\vec{\nabla} n}{n}. \tag{3.5}$$

This is the general equation for the hydrodynamic expansion of a UNP, which shows that the electron thermal pressure gradient drives the plasma expansion. The acceleration increases linearly with T_e. Additionally, because the acceleration depends on $\frac{\vec{\nabla} n}{n}$, this indicates that different density distributions could give rise to very different and interesting physics.

3.2 Expansion of a Gaussian Plasma

UNPs with an initial Gaussian density distribution, or Gaussian UNPs, given by

$$n(\vec{r}) = n_0 e^{-r^2/2\sigma_0^2} = n_0 \exp\left[-\frac{x^2}{2\sigma_x^2} - \frac{y^2}{2\sigma_y^2} - \frac{z^2}{2\sigma_z^2} \right] \tag{3.6}$$

have been studied extensively and used in many experiments [19, 20, 28, 39, 65–71]. Gaussian plasmas have an exact solution to the Vlasov equations [19], which is unique. Additionally, the expansion of a Gaussian plasma is well understood, and is what we compare the expansion of an exponential plasma to [22]. The expansion of a Gaussian UNP is discussed here before analyzing the expansion of an exponential UNP in Sec. 3.3.

Assuming spherical symmetry and substituting Eq. 3.6 into Eq. 3.5 yields

$$\dot{\vec{v}}_{exp}(\vec{r}, t = 0) = \frac{k_B T_{e0}}{m_i \sigma_0^2} \vec{r}. \tag{3.7}$$

The acceleration has a linear dependence on the displacement vector $\vec{r}$, which means the Gaussian UNP maintains its shape as it expands, or it self-similarly expands. Dimensional analysis yields a characteristic time scale for the plasma expansion,

$$\tau_{exp} = \sqrt{\frac{m_i}{k_B T_{e0}}} \sigma_0, \tag{3.8}$$

which depends only on the initial size of the plasma and the electron temperature. This is a significant parameter that will be used to describe the plasma expansion, and will be applied to the exponential plasmas.

An exact analytic solution can be found for the expansion of a quasi-neutral spherically symmetric Gaussian plasma, given by [69]

$$\sigma(t) = \sigma_0 \sqrt{1 + t^2/\tau_{exp}^2} \tag{3.9}$$

$$\gamma(t) = \frac{t/\tau_{exp}^2}{1 + t^2/\tau_{exp}^2} \tag{3.10}$$

$$T_i(t) = \frac{T_i(0)}{1 + t^2/\tau_{exp}^2} \tag{3.11}$$

$$T_e(t) = \frac{T_e(0)}{1 + t^2/\tau_{exp}^2} \tag{3.12}$$

$$\vec{v}_{exp}(\vec{r}, t) = \frac{t}{t^2 + \tau_{exp}^2} \vec{r}. \tag{3.13}$$

Equations 3.9, 3.11 and 3.12 can be rewritten as universal curves for the evolution of the size and species temperatures.

$$\frac{\sigma(t)}{\sigma_0} = \sqrt{1 + t^2/\tau_{exp}^2} \tag{3.14}$$

$$\frac{T_{i,e}(t)}{T_{i,e}(0)} = \frac{1}{1 + t^2/\tau_{exp}^2}. \tag{3.15}$$

These universal curves will be used to compare to the expansion of an exponential plasma in the next section.

3.3 Expansion of an Exponential Plasma

In this section, the expansion of an exponential UNP is studied and compared to the expansion of a Gaussian UNP. We are interested in understanding if the expansion of an exponential UNP is driven by the same physical effects that dominate during the expansion of a Gaussian UNP, namely the electron thermal pressure gradient. Additionally, we see if the expansion can be characterized by similar parameters as a Gaussian plasma, like σ and τ_{exp}.

An exponential plasma has an exponentially decaying density distribution given by Eq. 2.1. This density distribution is illustrated and compared to the Gaussian plasma in Fig. 3.1. Fig. 3.1A shows a false-color image of an exponential plasma's density distribution 350 ns after photoionization next to Fig. 3.1B which is a false-color image of a Gaussian plasma's density distribution at 330 ns expansion time. Figures 3.1C and D show the density of the Gaussian and exponential plasmas with their respective 2D fits along the x and y-axes respectively. Both are well described by the fits, although the exponential plasma is not as sharply peaked at the center as the fit. The fits are done by integrating the z-axis over the width of the LIF imaging beam.

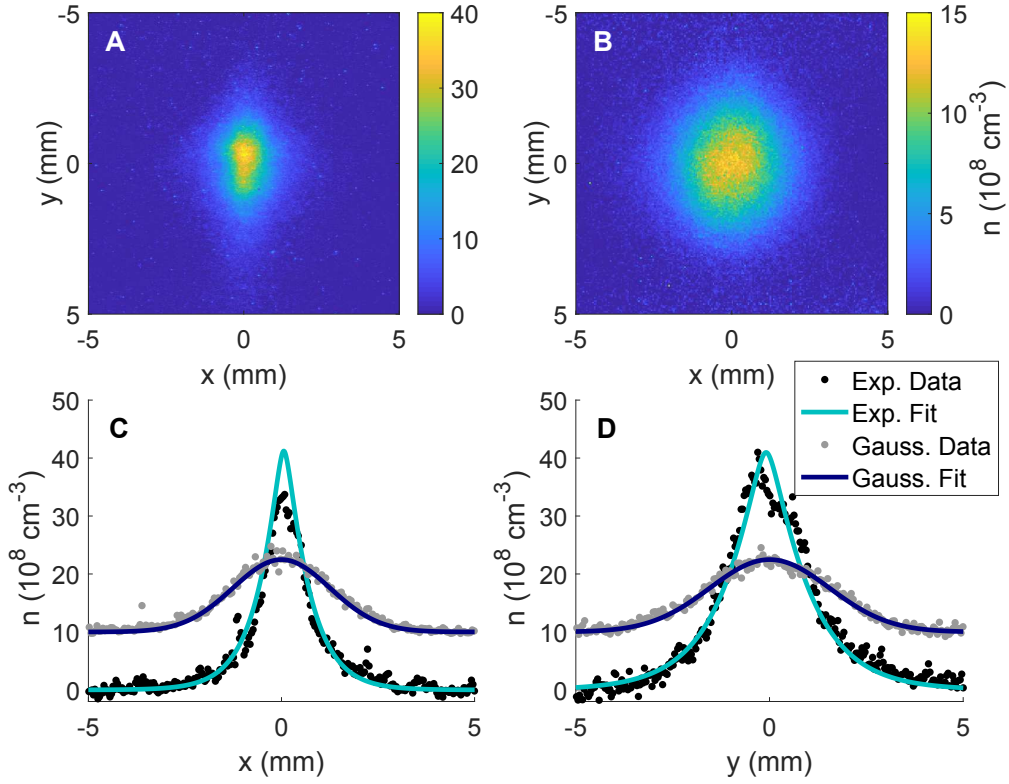

FIGURE 3.1: (A) False-color initial density profile of an exponential plasma with $T_e(0) = 160$ K at $t = 350$ ns after photoionization. (B) Density distribution of a Gaussian plasma with $T_e(0) = 40$ K at $t = 330$ ns. (C) Density along the x-transect through the center of the plasmas shown in (A) and (B). (D) Density along the y-transect through the center of the plasmas shown in (A) and (B). The Gaussian x and y-transects are offset for clarity. Integrating Eq. 2.1 for the exponential plasma and of Eq. 3.6 for the Gaussian plasma over the LIF laser sheet thickness gives the fits in (C) and (D). From [22].

3.3.1 Theory

Substituting the exponential density from Eq. 2.1 into Eq. 3.5 gives

$$\dot{\vec{v}}_{exp} = \frac{k_b T_e}{m_i \sigma_0} \frac{2x\hat{x} + \frac{y}{2}\hat{y} + \frac{z}{2}\hat{z}}{\sqrt{x^2 + \frac{y^2}{4} + \frac{z^2}{4}}} \tag{3.16}$$

for the acceleration due to the thermal pressure gradient. Unlike the equation for the acceleration of a Gaussian plasma (Eq. 3.7), Eq. 3.16 is not linear in $\vec{r}$, so we do not expect a self-similar expansion. Instead, the density distribution should start changing

immediately.

Since we image the plasma in the xy-plane, $z = 0$ and 3.16 becomes

$$\dot{\vec{v}}_{exp} = \frac{k_b T_e}{m_i \sigma_0} \frac{2x\hat{x} + \frac{y}{2}\hat{y}}{\sqrt{x^2 + \frac{y^2}{4}}}. \tag{3.17}$$

From 3.17, it is clear that the acceleration along the x-axis is larger than along the y-axis. While the plasma is initially smaller along the x-axis than the y-axis, due to the difference in acceleration on the two axes, we expect to see an inversion in the aspect ratio as the electron thermal pressure gradient drives the expansion of the exponential plasma.

Since the imaging beam propagates along the x-axis, we only have velocity data in the x-direction, so we are most interested in the dynamics along the x-axis. Setting $y = 0$, Eq. 3.17 becomes a step function given by

$$\dot{\vec{v}}_{exp}(y, z = 0) = \begin{cases} \frac{2k_b T_e}{m_i \sigma_0}, & x \geq 0 \\ -\frac{2k_b T_e}{m_i \sigma_0}, & x < 0. \end{cases} \tag{3.18}$$

From Eq. 3.18, the acceleration of an exponential plasma is not linearly dependent on r, as seen in a Gaussian plasma (Eq. 3.7). Therefore, self-similar expansion is not expected. Instead, the initial acceleration is piece-wise defined, with constant values but opposite signs on either side of the the plasma. This is illustrated in Fig. 3.2.

Since the acceleration is a piece wise-defined constant and the initial velocity is 0 m/s, integrating Eq. 3.18 with respect to time gives an initial velocity of

$$\vec{v}_{exp}(y, z = 0) = \begin{cases} \frac{2k_b T_e}{m_i \sigma_0} t, & x \geq 0 \\ -\frac{2k_b T_e}{m_i \sigma_0} t, & x < 0. \end{cases} \tag{3.19}$$

The velocity transect is clearly very different from a Gaussian plasma, which has a

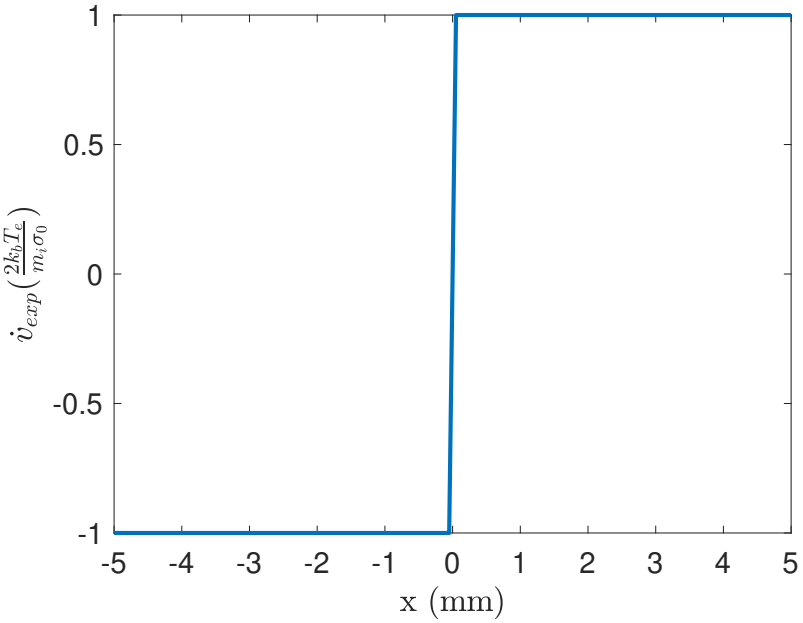

FIGURE 3.2: The initial acceleration of the plasma due to the electron thermal pressure gradient for an exponential UNP, given by Eq. 3.18. The acceleration is a step function. The initial velocity follows the same form, as shown in Eq. 3.19

linear velocity throughout the plasma. This should give rise to different and interesting physics. However, first we want to characterize the expansion of an exponential plasma before looking for new and interesting physics. The questions we are most interested in are:

1. Is the expansion hydrodynamic and driven by the electron thermal pressure gradient, or is it kinetic?

2. Can the exponential plasma be described by similar equations as the Gaussian plasma?

3. Are there characteristic length and time scales that can be used to characterize the plasma expansion?

3.3.2 Experimental Set Up

A full description of the experimental apparatus is found in Section 2.1. We form an exponential plasma by laser cooling and trapping Sr atoms in a purely magnetic trap, turning the magnetic field off, and photoionizing the atoms. Since we are interested in exploring if the expansion is predominantly hydrodynamic or kinetic, we vary both the density and the electron temperature. The combinations used are in Table 3.1.

$n_0(\times 10^{14}$ m$^{-3})$	T_e (K)
1	40
1	160
12	40
12	80
12	160
34	40
34	160

TABLE 3.1: The combinations of initial density and initial electron temperature used in the experiment studying the expansion of an exponential UNP.

In this experiment, we focus on plasmas with colder electrons (but still hot enough that recombination is not an issue) because the expansion is slower which allows us to more easily image and analyze the dynamics. Studying plasmas with hotter electrons required us to upgrade our imaging system because we needed to probe ions over a much larger detuning range than we could do with our setup. This has not been a problem for the Gaussian plasma experiments, despite using much hotter electrons in some experiments. This is likely due to a combination of smaller acceleration and focusing on early times.

3.3.3 Data and Results

Aspect Ratio Inversion

As discussed in Section 3.3.1, if the electron thermal pressure gradient drives the expansion of an exponential plasma, as described in Eq. 3.17, we expect to see an inversion of the aspect ratio because the acceleration is larger along the x-axis than the y-axis. Figure 3.3 shows a false color image of the plasma at three different points in the expansion: at 0 τ_{exp} or 100 ns (3.3A), 1.5 τ_{exp} or 17.6 μs (3.3B), and 2.5 τ_{exp} or 28.6 μs (3.3C). Figure 3.3A shows the initial aspect ratio where the plasma is smaller along the x-axis. Figure 3.3B shows the plasma when the size is roughly equal along both axes. Finally, Fig. 3.3C shows the inversion of the aspect ratio where the plasma is larger along the x-axis. This demonstrates that the acceleration is larger along the x-axis than the y-axis, suggestive that the plasma expansion is hydrodynamic. However, further analysis is needed to conclude that the electron thermal pressure gradient drives the expansion of an exponential plasma, as is true for Gaussian UNPs.

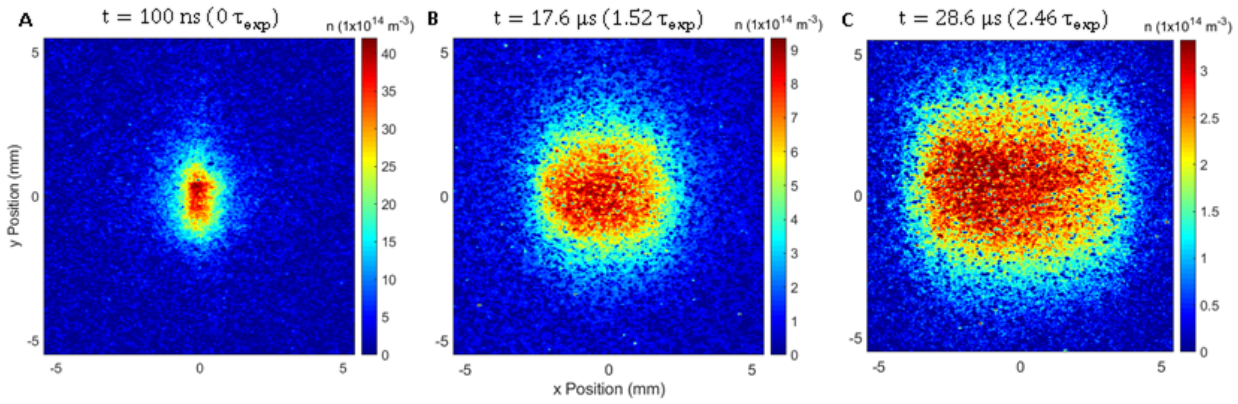

FIGURE 3.3: False-color density maps of an exponential UNP at (A) t = 0 τ_{exp}, (B) t = 1.5 τ_{exp}, and (C) t = 2.5 τ_{exp}. This figure shows an inversion of the size hierarchy as in (A) the plasma is smaller along the x-axis than the y-axis but in (C) the plasma is larger along the x-axis. Due to the hydrodynamic expansion, since it has a larger density gradient along the x-axis, it has a greater acceleration. Sharp transitions in the density are visible at the leading edge of expansion along the x-axis, suggesting wave steepening, which will be discussed in detail in Chapter 4. From [59].

Density Evolution

Because the acceleration for an exponential UNP is not linear in space (Eq. 3.18), an exponential UNP should not self-similarly expand, unlike a Gaussian UNP. Figure 3.4 shows the density x-transects and velocity x-transects for both a Gaussian (gray) and exponential (black) plasma. The density transects are shown with a 2D Gaussian fit for both plasmas - blue for the Gaussian plasma and purple for the exponential plasma. The initial fit of the density with an 2D exponential is included in Fig. 3.4A but not for subsequent times because it no longer describes the plasma. Even though the exponential plasma is not a Gaussian, the Gaussian fit captures the size of the plasma well, and is used to analyze the size evolution.

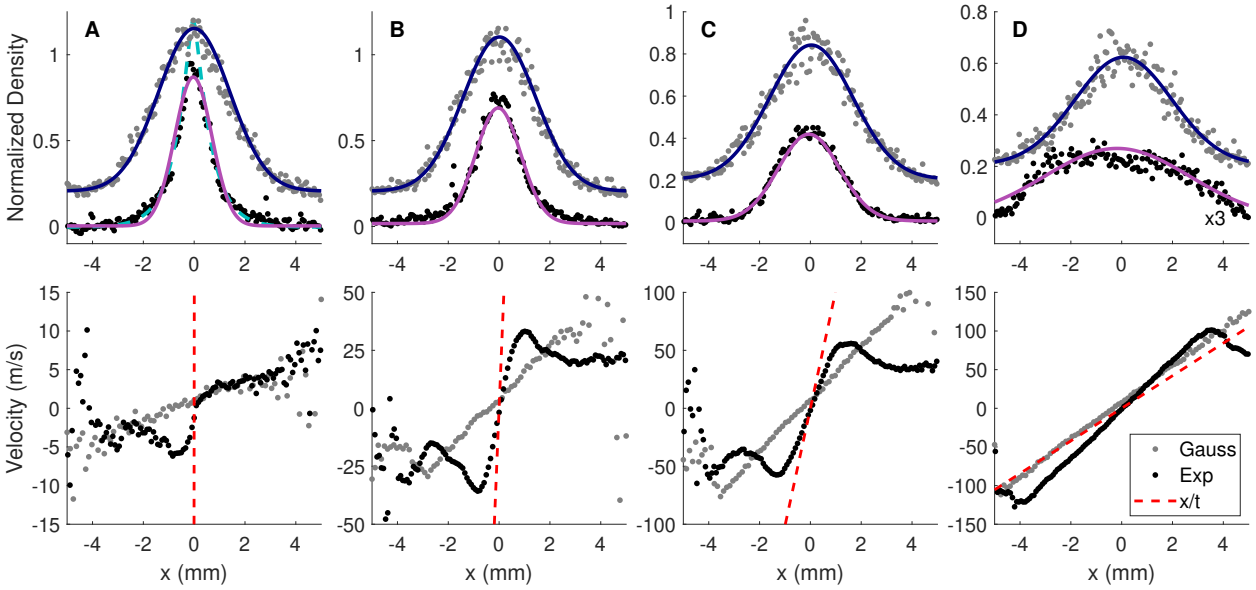

FIGURE 3.4: (Top) Density transects along the x-axis and (bottom) velocity x-transects for Gaussian (gray) and exponential (black) plasmas. The density is scaled by the initial peak density. The initial peak densities are 1.0×10^9 cm^{-3} and 3.5×10^9 cm^{-3} for Gaussian and exponential UNPs respectively. $T_e(0) = 40$ K for both plasmas. Density transects for the Gaussian plasmas are offset for clarity. The time after photoionization is (A) 0.34 $\pm$ 0.01 μs, (B) 5.7 $\pm$ 0.1 μs, (C) 14 $\pm$ 4 μs, and (D) 27 $\pm$ 3 μs. All density transects are fit Eq. 3.6 integrated over the LIF laser sheet thickness. The exponential plasma in (A) is also fit to Eq. 2.1 integrated over the LIF laser sheet thickness (dashed line). From [22].

As the top row of Fig. 3.4 shows, the Gaussian plasma self-similarly expands, maintaining a Gaussian density distribution throughout the evolution. In contrast, an exponential UNP quickly changes shape as the sharp peak quickly flattens out and the plasma becomes flatter in the center with a steep gradient at one edge. The second row of Fig. 3.4 will be discussed in the section on velocity below.

Figure 3.5 shows the density evolution of the center of the plasmas for different initial densities and electron temperatures. Figure 3.5A plots density as a function of time in unscaled units. For plasmas with the same initial density, higher electron temperatures cause the plasma to expand faster, which is consistent with a hydrodynamic model driven by the electron thermal pressure gradient.

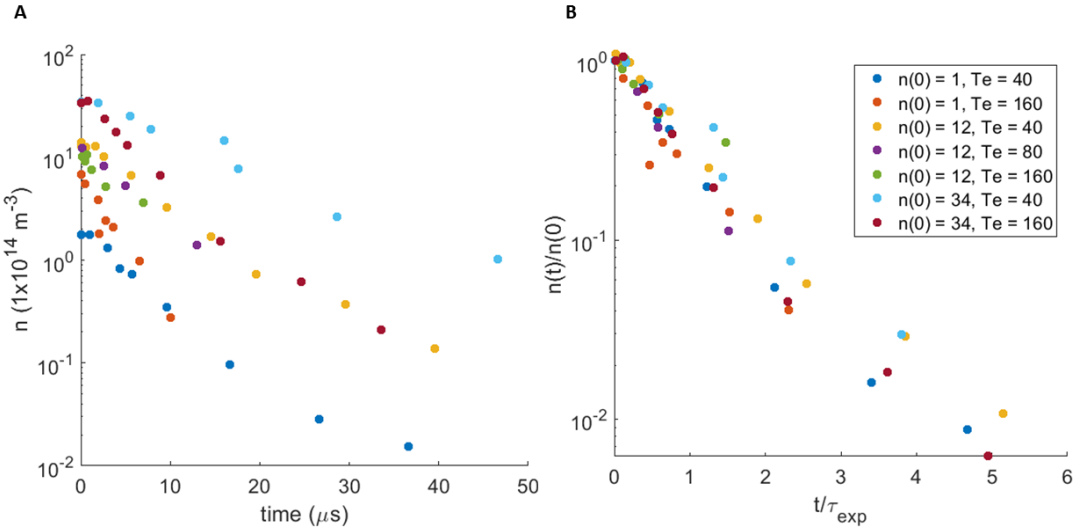

FIGURE 3.5: Evolution of the peak ion density (A) unscaled and (B) density normalized by initial peak ion density and time scaled by τ_{exp}. In the legend, initial density n(0) is in units of $\times 10^{14}\mathrm{m}^{-3}$ and electron temperature Te is in K. The normalized density evolution follows a universal curve when time is scaled by τ_{exp}, demonstrating that the electron thermal pressure gradient drives the expansion of of an exponential plasma, as in the hydrodynamic expansion of a Gaussian plasma. From [59].

Fig. 3.5B shows the density scaled by the initial density and the time by τ_{exp}. In this plot, the data collapses onto a universal curve. This shows that the expansion is

independent of the density, so the expansion is not due to a collisional process. This is consistent with a hydrodynamic model.

Since the data follows a universal curve when time is scaled by τ_{exp}, this further suggests that the expansion is driven by the electron thermal pressure gradient. Additionally, it shows that τ_{exp} is a significant timescale for the expansion of an exponential UNP.

Size Evolution

Figure 3.6 shows the size evolution of exponential UNPs with various initial densities and electron temperatures compared to a Gaussian UNP with $T_e(0) = 40$ K. To describe the size, the 2D density is fit to integrals over the LIF laser-sheet thickness of a 3D Gaussian (Eq. 3.6) instead of an exponential (Eq. 2.1) because very quickly after the plasma formation, the exponential fit no longer describes the plasma but the Gaussian still captures the size of the plasma throughout the evolution, as shown in the top row of Fig. 3.4. The RMS radii σ_x and σ_y are extracted from the fits. Due to cylindrical symmetry around the x-axis, $\sigma_y = \sigma_z$. The evolution of the geometric mean of the plasma size, $\sigma_m = (\sigma_x \sigma_y \sigma_z)^{1/3} = (\sigma_x \sigma_y^2)^{1/3}$, is shown in Fig. 3.6.

Figure 3.6A shows the size evolution in unscaled units. Similar to the discussion of the density evolution above, plasmas with the same initial size but higher initial electron temperatures expand faster, further suggesting that the expansion is driven by the electron thermal pressure gradient.

As with the density evolution in Fig. 3.5, Fig. 3.6B shows that when the data is scaled by the initial plasma size $\sigma_m(0)$ and the time scaled by τ_{exp}, the data follows a universal curve. This further confirms that the expansion is hydrodynamic. It also shows that τ_{exp} is a useful timescale for describing the expansion of an exponential plasma.

Fig. 3.6B shows the Gaussian plasma is well described by Eq. 3.14, which is expected. One significant difference is the exponential plasma expands faster than the Gaussian

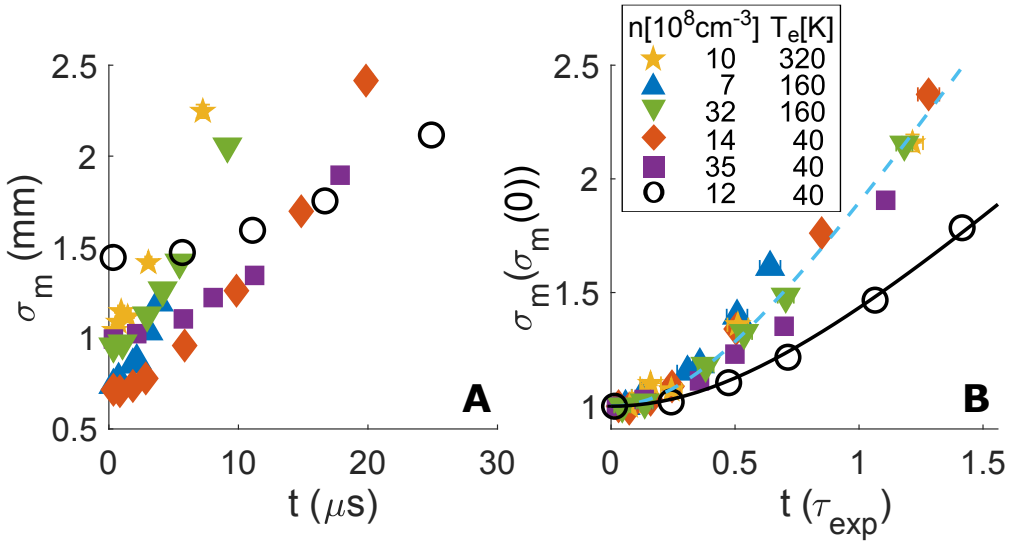

FIGURE 3.6: (A) Plasma size evolution. The size is the geometric mean of the size extracted from the Gaussian fit. The open circles are for a Gaussian plasma while the filled shapes are exponential UNPs with different initial conditions. As the electron temperature increases, the plasma expands faster, as expected for hydrodynamic expansion. (B) The normalized size as a function of scaled time with fits to Eq. 3.14 (black) and a modified Eq. 3.21 (light blue). In the legend, initial density n(0) is in units of $\times 10^{14}\mathrm{m}^{-3}$ and electron temperature Te is in K. From [59].

plasma. Equation 3.14 does not describe the size evolution. However, if

$$\tau_{exp} \rightarrow \beta \tau_{exp}, \tag{3.20}$$

where β is a dimensionless scalar that depends on the plasma initial conditions, Eq. 3.14 becomes

$$\frac{\sigma(t)}{\sigma_0} = \sqrt{1 + t^2/\beta^2 \tau_{exp}^2}. \tag{3.21}$$

The exponential UNP σ_m data is fit with Eq. 3.21, as shown by the light blue dashed curve in Fig. 3.6B. For exponential UNPs, $\beta = 0.63$, while for Gaussian UNPs $\beta = 1$. The size evolution is well described by this modified Gaussian UNP hydrodynamic equation, although $\beta = 0.63$ does not perfectly describe all initial conditions.

Velocity transects

Figure 3.7 shows the x-component of the expansion velocity along the x-axis for the same data in Fig. 3.4. Data with different initial densities and electron temperatures but for similar times scaled by $\beta\tau_{exp}$ are plotted together at four different times in the expansion. The velocity is scaled by $\tilde{v} = \sigma_m(0)/\beta\tau_{exp}$ and the position is scaled by $\sigma_m(0)$.

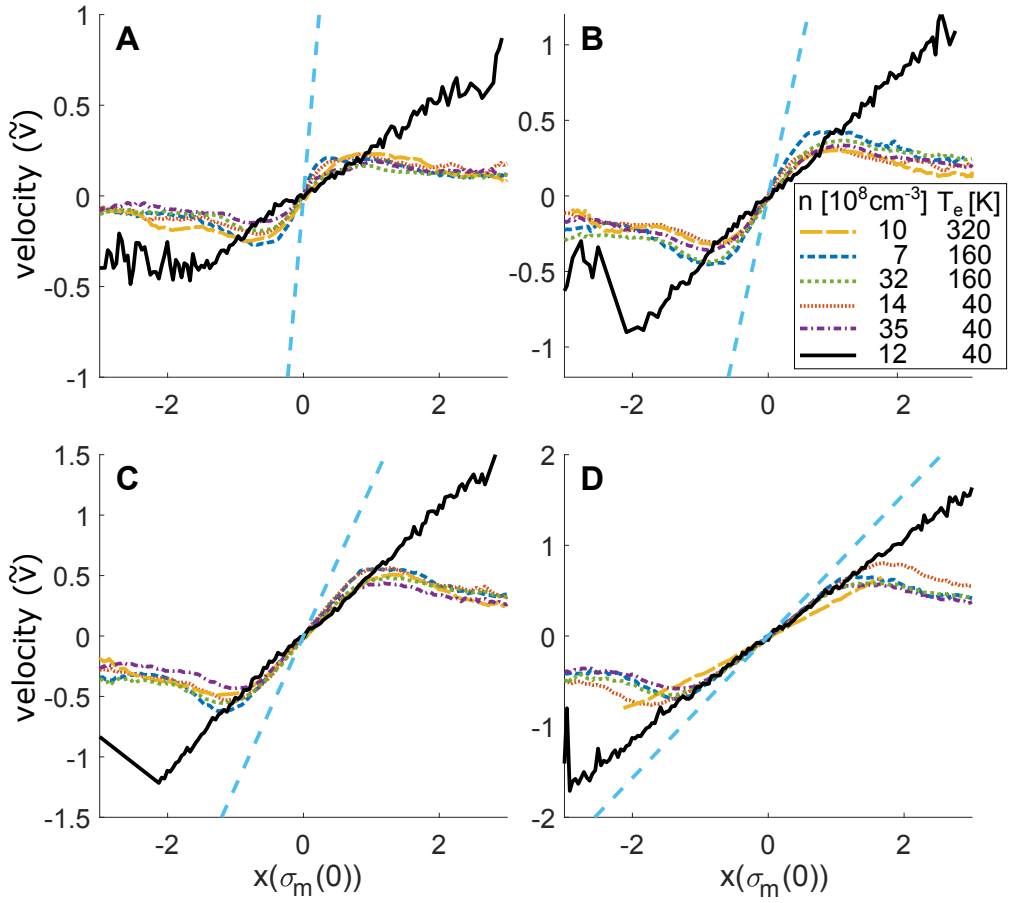

FIGURE 3.7: x-transects for the x-component of the velocity at $t/\beta\tau_{exp} = 0.23 \pm 0.02$ (A), 0.49 ± 0.09 (B), 0.80 ± 0.05 (C), 1.28 ± 0.35 (D). Velocity is in units of $\tilde{v} = \sigma_m(0)/\beta\tau_{exp} = \sqrt{k_B T_e(0)/m_i}/\beta$, and position is scaled by $\sigma_m(0)$. Initial peak density and $T_e(0)$ are shown in the legend. The light blue dashed line is the terminal velocity $\vec{u} = \vec{r}/t$. The solid line is a data for a Gaussian plasma. All other data are for exponential plasmas.From [59].

The scaled velocities follow universal curves, as was seen in the density (Fig. 3.5) and size (Fig. 3.6) evolutions above. This is further evidence that the expansion of the

exponential plasma is hydrodynamic.

The solid black data show the velocity transects for a Gaussian UNP. The velocity is linear throughout the plasma where the is sufficient plasma to make reliable measurements, or for $|x| \lesssim 2\sigma_m(0)$. This linear velocity is in agreement with Eq. 3.13, and is the signature of self-similar expansion. The velocity approaches $v = r/t$ for $t \gg \beta\tau_{exp}$, as shown in Figs. 3.4D (bottom) and 3.7D.

There are striking features where the exponential plasmas deviate from the Gaussian plasma. In scaled units, the initial velocity of the exponential plasma is much greater than the Gaussian plasma at the center, but is smaller than the Gaussian plasma for $x \gtrsim \sigma_m(0)$. At late times, shown in Figs. 3.7C and D, the velocity at the center of the exponential plasma is the same as the Gaussian, as both approach ballistic expansion given by $v = r/t$.

As expected from Eq. 3.19, the velocity is not linear throughout the plasma. However, Eq. 3.19 indicates that the velocity should be a step function initially, but Fig. 3.7A is not a step function. It is interesting that the velocity is linear at the center then quickly reaches a constant away from the center. The constant velocity at the edges of the plasma is in agreement with the hydrodynamic model. The linear velocity at the center of the plasma is interesting and subject of further investigation. Why does the velocity transect have that profile? Where does the linear part come from? Is there some other mechanism driving the expansion of the plasma at the center, like perhaps a Coulomb explosion? While these questions are beyond the scope of this thesis, the potential for a Coulomb explosion very early in the plasma expansion is discussed below.

The feature where there is faster ions overtaking slower ions is also interesting, and warrants further investigation, as if the velocity jump exceeds the sound speed, a shockwave would form. Since shockwaves have never been experimentally observed in UNPs despite theoretical predictions and experimental efforts, the observations of shockwaves in UNPs would open a new field of research. This is the subject of Chapters 4 and 5 of

this thesis.

Coulomb Explosion Derivation

One question that arises from the velocity transects is, "Why is the velocity constant at the edges of the plasma and linear in the center?" Due to the initial discontinuity of $\nabla n/n$ at the center of the plasma, it is possible that the electrons rapidly accelerate from the center of the plasma creating a net positive charge very early in the expansion. This charge imbalance where quasineutrality breaks down could cause a brief Coulomb explosion in the center of the plasma that eliminates the discontinuity. After a very brief period, the hole in electrons would fill back in as there is now a thermal pressure gradient and Coulomb well that would cause the electrons to accelerate back toward the center. In this section, we explore what a Coulomb explosion would look like in an exponential plasma and discuss how this compares to the data.

A charge imbalance would add another term to the hydrodynamic equation of motion

$$\dot{\vec{v}}_i = -\frac{k_B T_e}{m_i}\frac{\vec{\nabla} n}{n} + \frac{e}{m_i}\vec{E}. \tag{3.22}$$

Since we are interested in the behavior of a Coulomb explosion, we ignore the thermal pressure gradient. Equation 3.22 then becomes

$$\dot{\vec{v}}_i = \frac{e}{m_i}\vec{E}. \tag{3.23}$$

The derivation for the electric field produced by an exponentially decaying spherically symmetric pure ion charge distribution is found in Appendix C. The resulting electric

field is given by

$$\vec{E}(r) = \frac{en_0\sigma}{\epsilon_0}\left[\frac{2\sigma^2}{r^2}(1-e^{r/\sigma}) - \frac{2\sigma}{r}e^{-r/\sigma} - e^{-r/\sigma}\right]\hat{r}. \tag{3.24}$$

We solve for the acceleration given in Eq. 3.23 using Eq. 3.24.

$$\dot{\vec{v}}_i = \frac{e^2n_0\sigma}{m\epsilon_0}\left[\frac{2\sigma^2}{r^2}(1-e^{-r/\sigma}) - \frac{2\sigma}{r}e^{-r/\sigma} - e^{-r/\sigma}\right]\hat{r}. \tag{3.25}$$

Using the Taylor expansion of $e^{-r/\sigma}$and simplifying gives the ion acceleration

$$\dot{\vec{v}}_i = \frac{e^2n_0}{m\epsilon_0}\vec{r}. \tag{3.26}$$

The resulting ion velocity is

$$\vec{v}_i = \frac{e^2n_0}{m\epsilon_0}t\vec{r}, \tag{3.27}$$

which is linear in both position and time. This is in agreement with the linear portion of the velocity transects at the center of the exponential plasma, suggestive of Coulomb repulsion at the center.

The slope of the velocity transect from Eq. 3.27 is given by $\frac{e^2n_0t}{m\epsilon_0}$. Assuming there are no electrons at the center, this gives a slope of 9×10^6 s^{-1} at t_{exp} = 300 ns. The mean velocity gradient at the center of the plasma at $t_{exp} = 300ns$ is 1×10^5 s^{-1}, which is significantly smaller than the slope predicted by Eq. 3.27. There are a couple potential reasons for this discrepancy.

First, if there is a Coulomb explosion, this result only holds true while the density distribution is exponentially decaying. As is seen in the density transects in Fig. 3.4, the sharp peak quickly becomes rounded or flat. Once the peak is gone, the thermal pressure gradient does not rapidly drive the electrons from the center. The positive charge

combined with the electron thermal pressure gradient from the hole would attract the electrons back to the center restoring neutrality. Once the density distribution is flat, that portion of the plasma will ballistically expand with a velocity profile close to $v = r/t$, which is what we see at later times.

It could be that the Coulomb explosion is much stronger earlier, but we only see evidence of it long after that happened. As discussed in Sec. 1.4.4, the electrons move on $\sim$1 ns time scales, but the first plasma image is at 300 ns. It could be that there is a large charge imbalance in the first few ns that creates a very brief Coulomb explosion that we cannot see. Assuming there is a pure ion plasma at the center of the plasma and assuming the slope at the center of the velocity transect is from a Coulomb explosion, solving Eq. 3.27 for time gives a velocity gradient of 1×10^5 s^{-1} in just 5 ns - a time that cannot be resolved with our imaging system.

Additionally, it is highly unlikely that there is a purely ion plasma at the center. Instead, it is likely that there is a significant net positive charge that has an exponential distribution. In that case, the slope of the velocity transect can be used to determine the net charge n_0. Doing so yields a net positive charge density of 0.2×10^{14} m^{-3}, indicating about 2% of the electrons escape at the center. Since only 2% of the electrons escape, the assumption that the thermal pressure gradient can be ignored does not hold. This suggests that there could be a non-negligible net charge that accelerates the expansion at the center of the plasma, but that the effect enhances the electron thermal pressure gradient rather than is the dominant expansion mechanism.

A recent experiment showed the development of shockwaves through a Coulomb explosion by detuning the photoionization laser well above the ionization threshold so that all of the electrons escaped, leaving a pure ion plasma [72]. It would be interesting to do an experiment studying how the slope of the velocity transect changes with increasing

electron temperature, crossing over from the quasi-neutral regime to the definitively non-neutral regime and reproducing their results. This would require imaging the plasma for a shorter period of time, much earlier in the plasma expansion.

Temperature Evolution

While a hydrodynamic description assuming quasi-neutrality (Eq. 3.2) appears to capture the behavior of the exponential plasma very well, as discussed above, the assumption of quasi-neutrality is suspect near the plasma center. The Debye length for electrons (Eq. 1.3) for $n_e = 10 \times 10^{14}\,\mathrm{m}^{-3}$ and $T_e = 320\,\mathrm{K}$ is $40\,\mu$m, which is on the order of the length scale of the central peak, so significant non-neutrality is possible near the origin for high-temperature and low-density exponential plasmas.

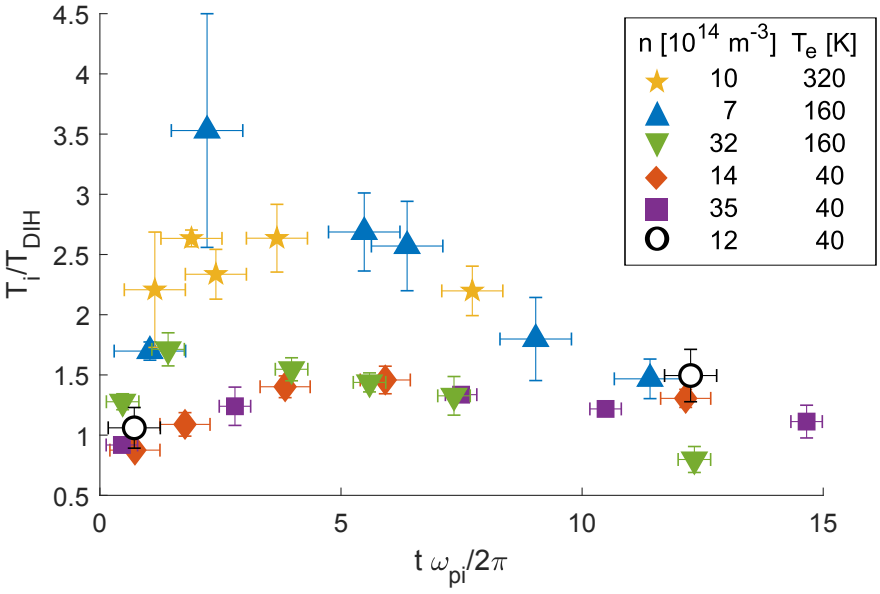

FIGURE 3.8: Temperature at the center of the plasma as a function of time. Temperature is scaled by the disorder-induced heating temperature and time is scaled by the ion plasma frequency. The significant heating seen in lower density and higher electron temperature data sets is suggestive of kinetic effects. From [22].

Figure 3.8 shows the ion temperature evolution at the center of the plasma. The temperature is scaled by T_{DIH} and the time by $2\pi/\omega_{pi}$ because T_{DIH} is the temperature that

the ions should equilibrate to in the first couple of ion plasma oscillations. For low $T_e(0)$, ions equilibrate to $T/T_{DIH} \sim 1$. Subsequent moderate heating on a longer timescale is likely due to dissipation of ion acoustic waves [23, 36] and electron-ion thermalization [66].

For $T_e(0) = 160\,\mathrm{K}$ and $T_e(0) = 320\,\mathrm{K}$, and more dramatically for lower ion density, however, ions rapidly reach $T/T_{DIH} \gtrsim 2.5$. This is suggestive that quasi-neutrality breaks down and, while the Gaussian hydrodynamic model works well, the plasma is not fully hydrodynamic. This extra heating could arise from plasma non-neutrality, which introduces additional Coulomb energy in the central region and potential subsequent Coulomb explosion, as discussed above. Alternatively, other kinetic effects could be introduced.

3.4 Conclusions

While the expansion of an exponential UNP does not have an analytic solution, the expansion is overall similar to the expansion of a Gaussian UNP. It is predominantly in the hydrodynamic regime, driven by the electron thermal pressure gradient. While it lacks the Gaussian UNP's signature self-similar expansion, nonetheless it can be described by similar characteristic length (σ_0) and time ($\beta\tau_{exp}$, where β = 1 for a Gaussian and β = 0.63 for an exponential) scales as the Gaussian UNP.

In the exponential UNPs, the ions at the center undergo significant heating for higher electron temperature and especially lower density. This suggests that while the plasma is predominantly hydrodynamic, there could be significant non-neutrality at the center causing a Coulomb explosion or other kinetic effects. This would be interesting to investigate further, both experimentally and computationally.

There are some significant differences in the density and velocity evolution, giving rise to new and interesting physics. The density and velocity x-transects show potential signs of wave steepening and shockwave development, which warrant further study. The development of shockwaves in exponential UNPs is discussed in Chapter 4 and the characterization is studied in Chapter 5.

Chapter 4

Shockwave Development Through Wave Steepening

This chapter is based on the research published in [73].

The initial evolution of an exponential UNP is described in Chapter 3. In the early-time $T_e(0) = 160$ K data, there were hints of shockwaves to be further investigated. In this chapter, we observe the development of shockwaves through wave steepening in exponential UNPs, while Chapter 5 explores what impacts shock formation.

This experiment studies exponential plasmas with $n(0) = 15 \times 10^{14}$ m^{-3} and $T_e(0) = 160$ K. As explained in Sec. 2.3.2, the transfer cavity needed to be upgraded so we could image ions over a much larger velocity range in order to conduct this experiment. While we included the $T_e(0) = 160$ K data in the expansion experiment, this experiment focuses on later times where the shock develops - when we could not image the ions in the previous experiment.

Additionally, the hydrodynamic expansion experiment described in Chapter 3 included data at $T_e(0) = 40$ K, where the hints of a shockwave were not seen. In order to explore the possibility of a shockwave, we needed more data later in the expansion when the shock develops and using a relatively high initial electron temperature.

This chapter gives an introduction to shockwaves, describes the simulation that was created to model the plasmas, discusses the experimental results, and explores the possibility of systematic errors in our measurements.

4.1 Shockwave Introduction

A shockwave is commonly defined as when the relative flow velocity exceeds the local sound speed, preventing information of the oncoming shock from propagating before it [74, 75]. This can occur when a driver moves through a medium, like an airplane flying through the air, or one population of particles moves through a background fluid with a relative speed exceeding the sound speed [76]. This is characterized by a Mach number $M > 1$, where for our system we define M as

$$M = \frac{v_{rel}}{v_s}, \tag{4.1}$$

where v_{rel} is the relative velocity on either side of the shock front, and v_s is the sound speed in the medium. For an unmagnetized UNP, the sound speed is the ion acoustic wave speed for hydrodynamic ions and kinetic electrons, given by

$$v_{IAW} = \sqrt{\frac{k_B}{m_i}(T_e + \gamma_i T_i)}, \tag{4.2}$$

where k_B is the Boltzmann constant, m_i is the ion mass, T_e is the electron temperature, T_i is the ion temperature, and γ_i is the adiabatic index for the ions. For our systems, $\gamma_i = 5/3$ because the density compression due to a sound wave is isentropic. Since $T_e \gg T_i$, Eq. 4.2 becomes

$$v_{IAW} = \sqrt{\frac{k_B T_e}{m_i}}. \tag{4.3}$$

In addition to $M > 1$, shockwaves are characterized by an abrupt change in pressure, temperature, and density over a small region [77, 78]. This can occur when nonlinear propagation effects cause the leading density gradient to steepen, or wave steepening [79]. Shockwaves can be seen throughout nature in different media and have many applications. Shockwaves commonly used to break apart kidney stones [80]. They are induced in ICF plasmas to ignite the fusion reaction [13]. In plasmas, shockwaves have been observed in the solar wind [81], supernova remnants [82], and laser-induced plasmas [83].

Since the creation of the first UNP [14], shockwaves in this environment have been of great interest. Shockwaves have been predicted to form in the low-density outer edge of Gaussian UNPs as they expand into vacuum [68, 69], but have not been experimentally observed because the density is too low for the experimental sensitivity. Shockwaves have also been predicted to develop in UNPs with non-Maxwellian electrons [84]. Additionally, shocks are predicted to form from a hydrodynamic model of colliding molecular UNPs [85].

As discussed in 1.5.1, during the electron equilibration process, electrons escape from the plasma until a Coulomb well traps the remaining ∼95% of electrons [14]. The net positive charge is predominently on the peripheral of the plasma. More recent MD simulations of a Gaussian UNP showed that this non-neutrality at the plasma edge can give shock-like features [46].

Computational work indicates that shocks can be induced in UNPs if the plasma has an initial large density gradient. Early plasma modeling in a very different context shows that a plasma with an initial step-function density distribution exhibits wave-steepening and the formation of a shockwave as it expands into vacuum [86]. Other work shows that these sharp gradients are maintained as the plasma expands and discusses the critical role of charge separation [87].

Experiments that created increasing density depletions in Gaussian UNPs produced

streaming plasmas, crossing from the hydrodynamic [21, 36, 37] to kinetic regime [23]. While shockwaves were not observed, these experiments suggested that creating a large enough density gradient could give rise to shocks.

Shockwaves have been observed in ultracold plasmas formed by photoionizing atoms well above the ionization threshold creating a pure-ion plasma that forms shockwaves as the plasma Coulomb explodes [72].

4.2 Plasma Fluid Simulation

The Solar Physics Research Group at Rice University developed a multipurpose plasma simulation called SPRUCE [88]. SPRUCE is a quasi-neutral 2D fluid model that uses separate energy equations for the electrons and ions, one continuity equation, and one momentum equation. Barton's method, which is a differentiation method for discontinuous fluid problems that yield shock conditions without non-physical oscillations present in other schemes [89], is used to solve the transport derivatives while all other derivatives are solved using a second-order central finite difference method. A second-order Runge-Kutta method is used for time integration [88]. These equations are solved on a uniform Cartesian grid with a domain that is much larger than the actual plasma size. For our experiments, we only have data for $|x|, |y| \leq 5$ mm, while the simulation's domain is $|x|, |y| \leq 12$ mm.

The simulation is initialized with the initial experimental data. The density and ion temperature are interpolated from the data, while the electron temperature is assumed to be uniform. Since the simulation domain is significantly larger than the plasma size, the density beyond the image is determined from a 2D exponential fit to the initial density distribution. A small uniform background that is 10^{-4} of the peak density is added to the density to mitigate instabilities where the density is very small.

The electron temperature is assumed to be uniform, and is initialized from the data. As discussed in Sec. 1.5.1, because the electron mean free path is on the order of the plasma size, the electrons are in global thermal equilibrium throughout the plasma expansion. At each time step, the electron temperature is replaced with the mean electron temperature

$$\bar{T}_e = \frac{1}{N} \int n T_e(x, y) dx dx, \tag{4.4}$$

where $N = \int n dx dy$. This simulation gives the electron temperature, which is essential in calculating the ion acoustic wave speed and determining the Mach number. The electron temperature from the simulation is shown in Fig. 4.1.

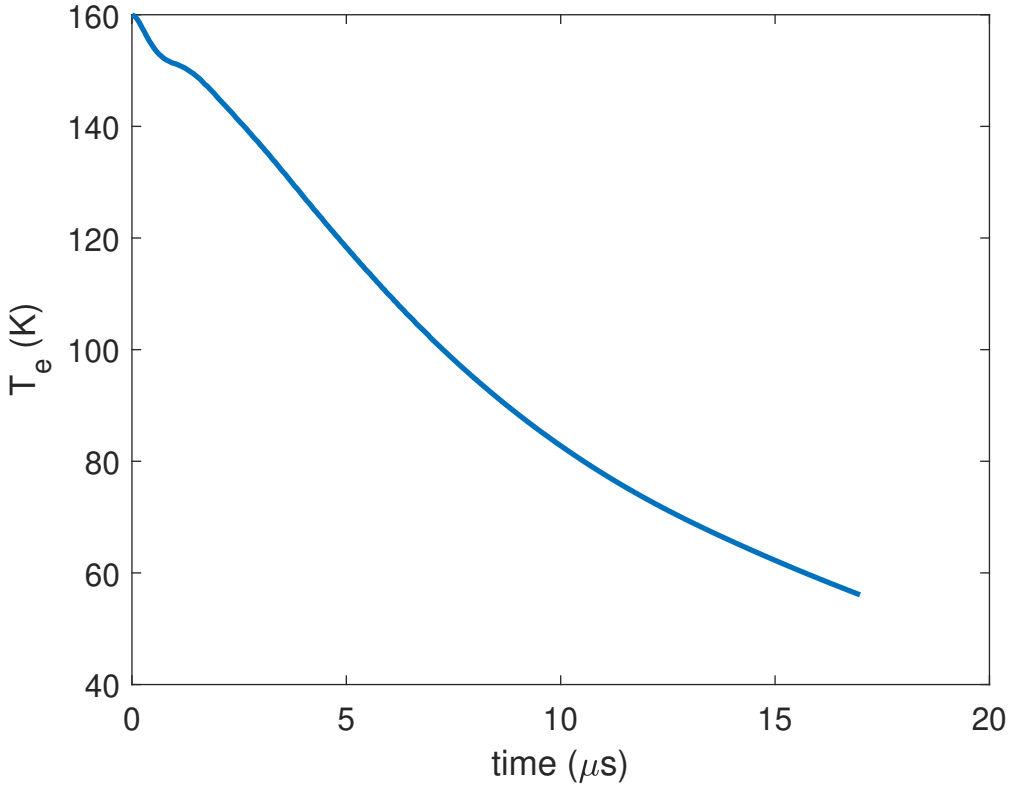

FIGURE 4.1: The electron temperature evolution from SPRUCE, a 2D, two-fluid plasma simulation.

Because this is a 2D simulation, the ion flux out of the central plane is neglected, causing the absolute density to be higher than in the experiments. This does not affect the plasma expansion or the sound speed. In Fig. 4.3, which will be discussed later, the density from the simulation is scaled to match the corresponding peak density from experimental data. While the absolute density is higher in the simulation, the simulation effectively captures the evolution of the plasma shape, as shown in Fig. 4.3, where the experimental data is in the different markers and the simulation results are the solid lines. The simulation also effectively captures the velocity evolution as shown in Fig. 4.4. The density, velocity, and ion temperature evolution of the 3D plasma is discussed in more detail in Secs. 4.3, 4.4, and 4.6 respectively.

4.3 Wave Steepening in Density

The initial expansion of the density is described in detail in Section 3.3.3. Here we focus more on later time information, while still including early time data.

Figure 4.2 shows false-color images of the exponential UNP at early time (300 ns expansion, 4.2a) and late time (12 μs expansion, 4.2b). In Fig. 4.2b, the density is relatively constant within $|x| \lesssim 2.5$ mm, showing a density plateau. Sharp density gradients are seen at the edge of the plasma along the x-axis, indicative of wave steepening.

The density evolution is shown in more detail in Fig. 4.3, showing the density along the $y = z = 0$ transect. The symbols are the measurements from the experiment at different times while the lines are from a simulation that is described in section 4.2. The sharp peak quickly flattens out as the plasma expands. As the plasma expands, the size of the flat region increases while the maximum density decreases. The leading edge of the plasma expansion accelerates with time, creating a density plateau with a sharp jump

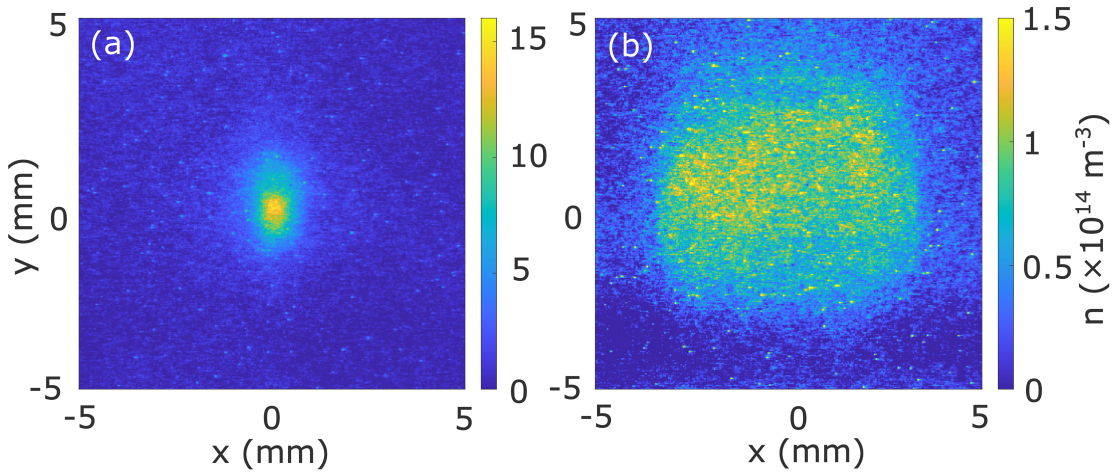

FIGURE 4.2: False color images of the density in a cut through the plasma center at (a) 0.3 μs and (b) 12 μs after photoionization. Tighter confinement along the x-axis of the atoms and the resulting plasma creates a larger density gradient and hydrodynamic pressure driving expansion along that axis. Sharp transitions in the density are visible at the leading edge of expansion along the x-axis in (b), indicative of wave steepening and shock formation. From [73].

in density, which is most clearly seen at 12 μs. This is evidence of wave steepening, where a high-density front is expanding into a low-density region.

4.4 Velocity Jump

Figure 4.4 shows the velocity x-transects for different times in the plasma expansion, corresponding to the density transects in Fig. 4.3. Like in Fig. 4.3, in Fig. 4.4, the symbols are the data and the lines are from the simulation described in Section 4.2. The velocity is scaled by the ion acoustic wave speed at that time ($v_{IAW}(t)$), which is described in detail in Section 4.5.

As described in Section 3.3.3, the velocity transects are linear at the center, reach extrema, decrease, and are constant at the edge of the plasma. This is in stark contrast with Gaussian plasmas [19], where the velocity increases linearly from the center of the plasma

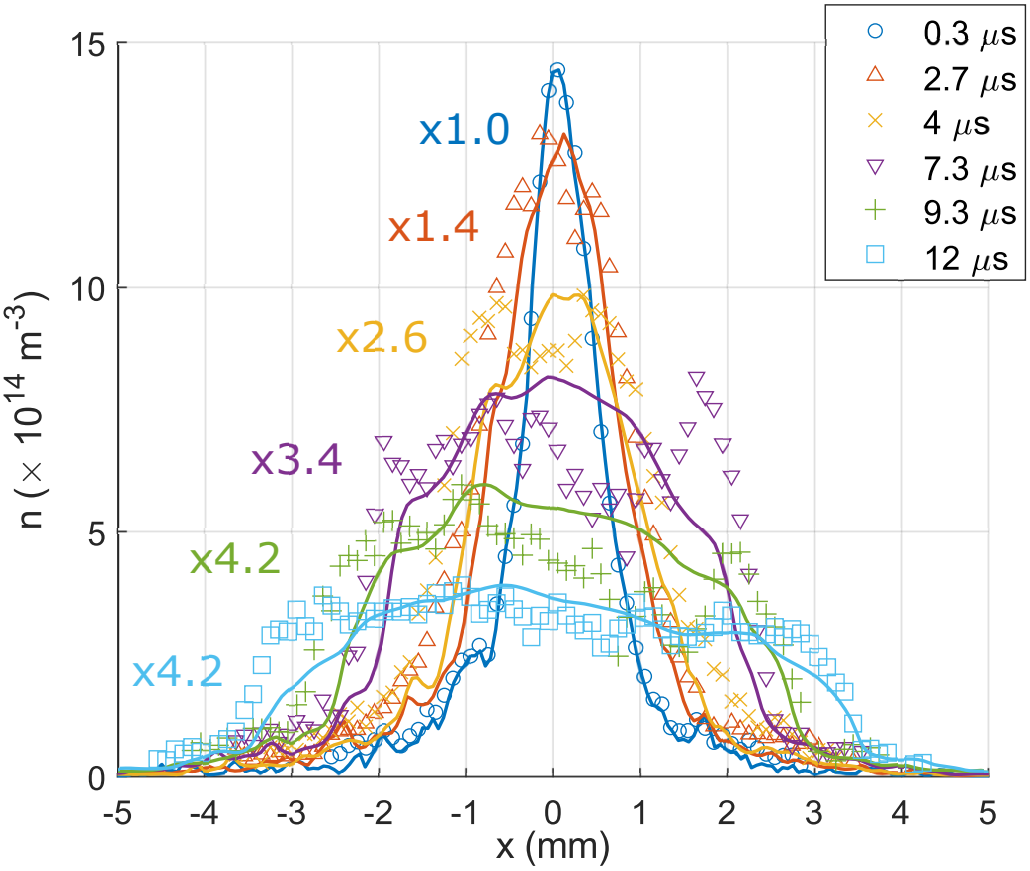

FIGURE 4.3: Density x-transects at different times in the plasma evolution. The plasma is initially sharply peaked with its exponential profile. As the plasma evolves, first the peak flattens, forming a plateau. Later in the plasma expansion, a density jump develops at the advancing front, as seen at 12 μs. This is suggestive of wave-steepening.

throughout the plasma. The maximum velocity for a Gaussian plasma is at the edge of the plasma, where the plasma does not have neighboring plasma to expand into.

At the center of the plasma, the initial acceleration is much larger for the exponential plasma than the Gaussian plasma. However, away from the center of the plasma, the Gaussian plasma has a larger initial acceleration than the exponential plasma. This means exponential plasmas have the potential to develop velocity extrema that are not at the edge of the plasma like with Gaussian plasmas, as shown in Fig. 4.4.

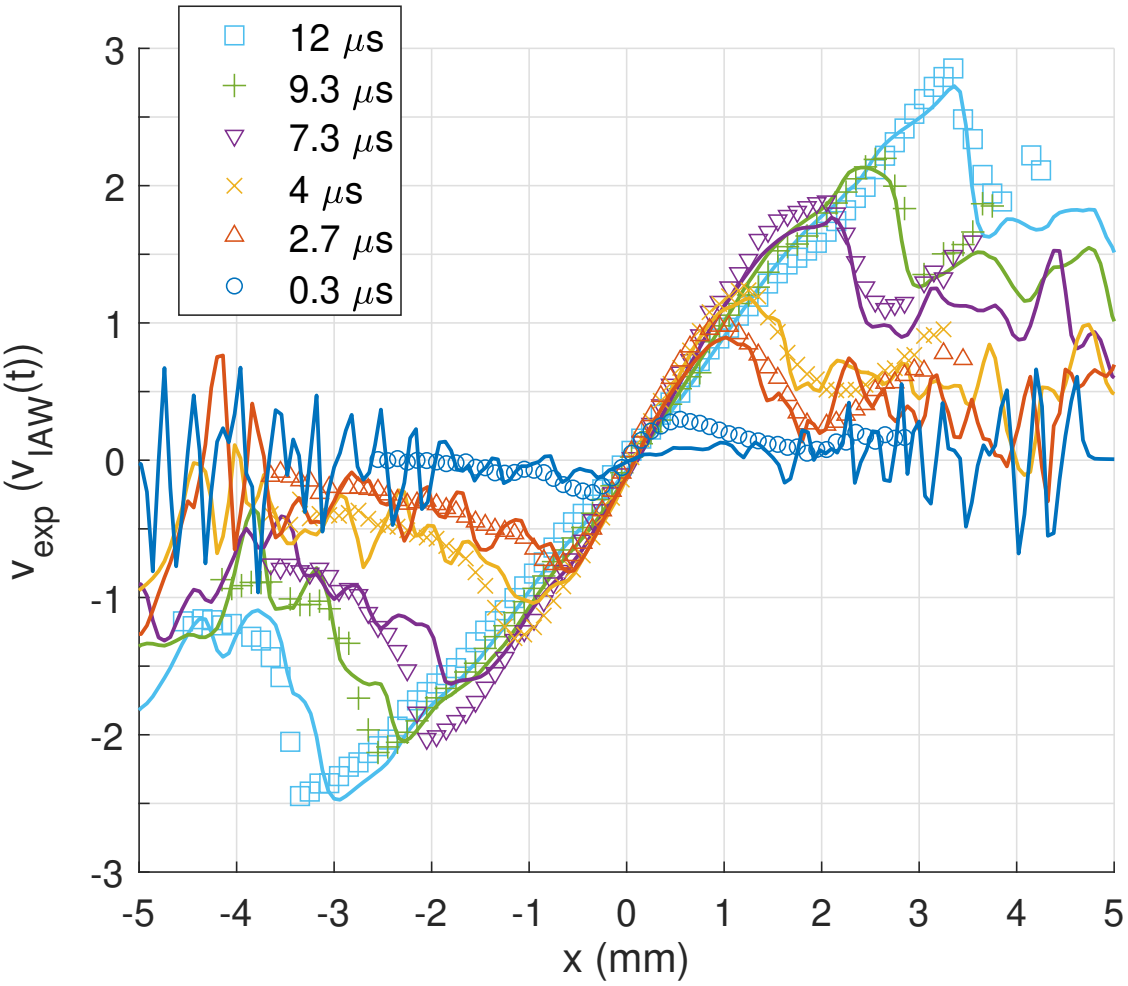

FIGURE 4.4: The x-component of the expansion velocity x-transects scaled by the ion acoustic wave speed $v_{IAW}(t)$ at different times in the plasma expansion. The times are indicated in the legend. The expansion velocity is linear in the center of the plasma, reaches a peak, and decays to a constant at the edges of plasma. As the plasma expands, the velocity peaks develop into a jump with a significant decrease in velocity over a short distance, as seen in $t_{exp} \gtrsim 7\mu s$.

At the plasma expands, the peaks in the velocity form a jump where the velocity significantly decreases over a small region. This is most clearly seen in $t_{exp} \gtrsim 7\mu s$. Additionally, these peaks correspond to the edges of the density plateau seen in Fig. 4.3. At the velocity peaks, high-density and high-velocity plasma expands into low-density and low-velocity plasma, leading to wave steepening.

The magnitude of the velocity jump is an indicator of whether the jump of velocity and density represents a shockwave. This is discussed in more detail in Section 4.5.

4.5 Mach number

We are interested in seeing if M > 1 in our plasmas. As Fig. 4.4 shows, the ions expand faster than the sound speed, and even get close to Mach 3. However, it is the relative velocity of the high-density, high-velocity plasma expanding into the low-density, low-velocity region that matters, as that is the shock front.

As Eq. 4.3 shows, the electron temperature is essential in calculating v_{IAW}. The initial electron temperature is set by how far above the ionization threshold the ionization laser is detuned. Unfortunately, we are unable to measure the electron temperature, and thus only have indirect information on the evolution of T_e. To estimate the electron temperature, we use three methods. The upper limit is assuming the electrons do not cool, and thus remain at the initial temperature set by the detuning laser. While inelastic collisions can cause the electrons to heat [90], these effects are negligible for our densities and electron temperatures.

The lower limit is determined by estimating the cooling due to adiabatic expansion. Because we have relatively hot electrons and fairly low densities, the electron collisions are primarily elastic, and collisions between electrons and ions can be ignored. The equation for the temperature evolution as a system adiabatically cools is given by

$$T_e(t) = T_e(0)\frac{V(0)^{\gamma-1}}{V(t)^{\gamma-1}}. \tag{4.5}$$

$V = 4/3\pi\sigma_{GM}^3$, where $\sigma_{GM} = (\sigma_x\sigma_y\sigma_z)^{1/3}$ is the geometric mean of the size from the fit to Eq. 3.6. Due to symmetry, $\sigma_y = \sigma_z$ and $\sigma_{GM} = (\sigma_x\sigma_y^2)^{1/3}$. Substituting this and $\gamma = 5/3$

into Eq. 4.5 and this becomes

$$T_e(t) = T_e(0)\frac{\sigma_{GM}(0)^2}{\sigma_{GM}(t)^2}, \tag{4.6}$$

which from Eq. 3.21 can be rewritten as

$$T_e(t) = \frac{T_e(0)}{1 + (\frac{t}{\beta\tau_{exp}})^2}, \tag{4.7}$$

which is Eq. 3.12, but with $\tau_{exp} \to \beta\tau_{exp}$ since this is an exponential plasma not a Gaussian plasma. Equation 4.7 is preferred to Eq. 4.5 because at later times, the 2D fit to the plasma fails to accurately describe the plasma size, and so should not be used to determine the electron temperature.

The most trustworthy electron temperature estimate is from the SPRUCE simulations described in Section 4.2.

Figure 4.5 shows the Mach number as a function of time for the left side of the plasma. For early times, it is less than 1, but after ~ 7 μs, the Mach number exceeds 1 and remains above 1 for the duration of the data. After about 15 μs, the shock front propagates off the camera's viewing area. This is strong evidence that a shockwave develops in the UNPs.

4.6 Ion Temperature

Figure 4.6 shows the ion temperature transects along the x-axis throughout the plasma expansion, corresponding to the same data in Figs. 4.3 and 4.4. The temperature is offset by an amount that is proportional to time, and the offset is included in the legend.

At $t_{exp} = 0.3\mu s$, ion temperature is relatively smooth. Disorder-induced heating (DIH), which is described in Sec. 1.5.2, causes the ions to quickly heat from the ~ 10 mK atom temperature in the magnetic trap to ~ 1 K. For the maximum density of $14 \times 10^{14}\text{m}^{-3}$,

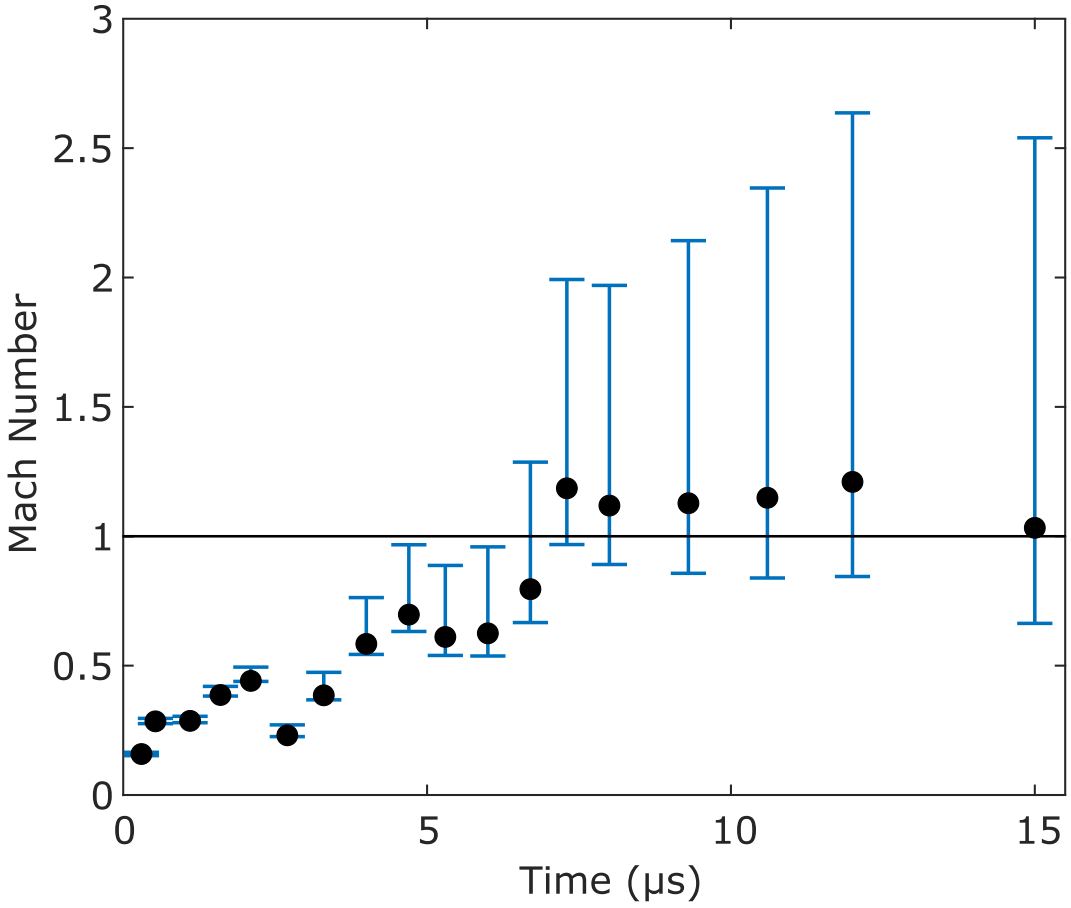

FIGURE 4.5: Mach number evolution for the plasma front for $x < 0$. Upper and lower bounds are described in the text. As the jumps in density and velocity develop, the Mach number surpasses Mach 1, suggestive of shock formation. From [73].

T_{DIH} = 1.2 K. However, the maximum temperature measured at 0.3 μs expansion is 2.6 K, which over a factor of 2 larger than T_{DIH}. This extra heating is likely caused by kinetic effects and initial non-neutrality at the sharp density peak in the center. As the plasma expands, the center adiabatically cools, as expected.

An interesting feature in the ion temperature transects is the development of localized heating. This is seen as spikes in the temperature develop, and reach maximum temperatures of over 20 K at 12 μs. Figure 4.7 shows the density, velocity, and temperature transects plotted on top of each other for $|x| < 0$ mm at 5.3 μs (a) and 12.0 μs (b). As this figure shows, the heating occurs where the density and velocity gradients are largest,

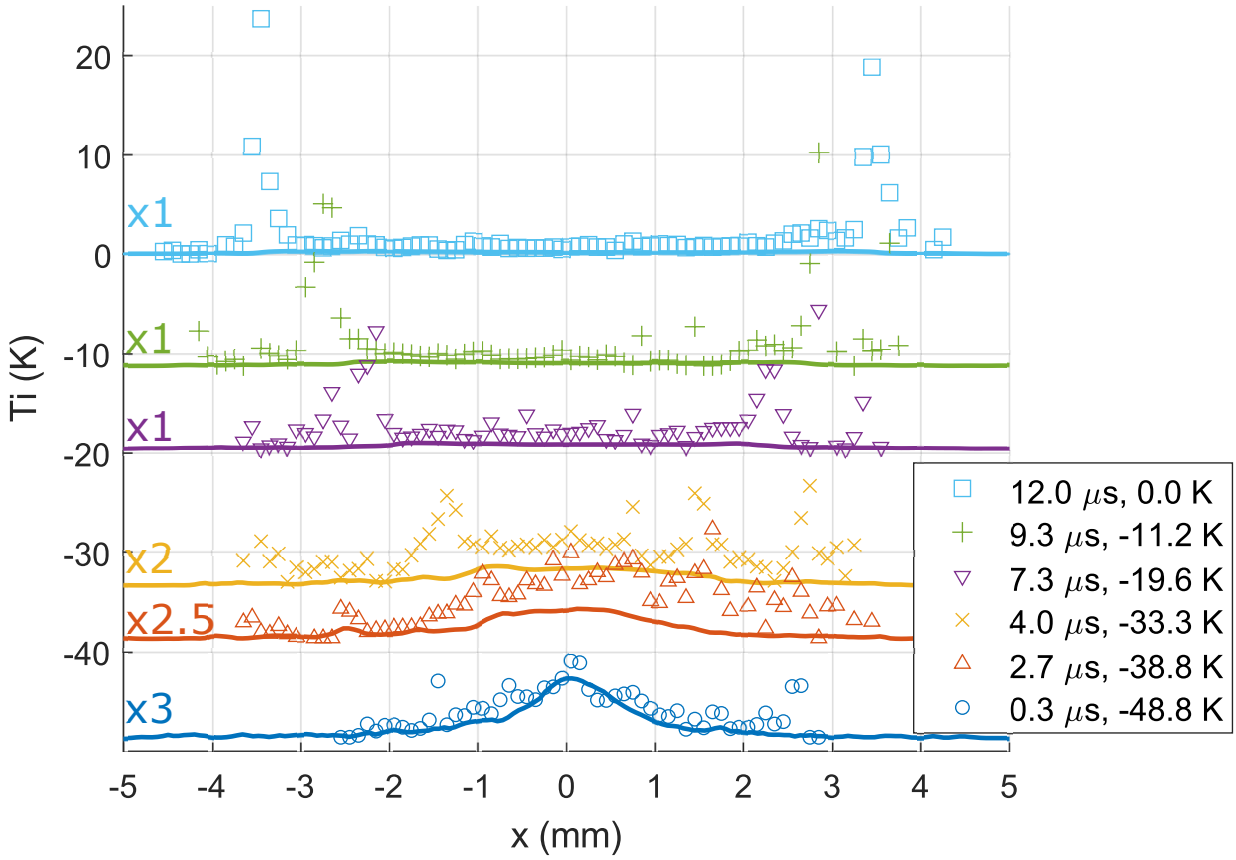

FIGURE 4.6: The ion temperature transects at different times in the plasma expansion, as indicated by the legend. For clarity, the temperatures are offset by an amount proportional to expansion time and is given in the legend. Initially, the maximum temperature is at the center of the plasma, which is expected because DIH depends on the density, and the maximum density is at the center. As the plasma expands, adiabatic cooling is predominantly seen but a temperature spike forms on either side of the plasma. The temperature spike increases with time.

overlapping with the shock front. The simulations, given by the solid lines in Figs. 4.6 and 4.7 only show a small rise in the temperature, suggesting that the temperature spikes are due to kinetic effects.

Because we measure the temperature over a finite region and the velocity gradients are quite large, it is important to examine if the localized heating is due to artificial broadening of the spectra. This is discussed in great detail in Section 4.7.

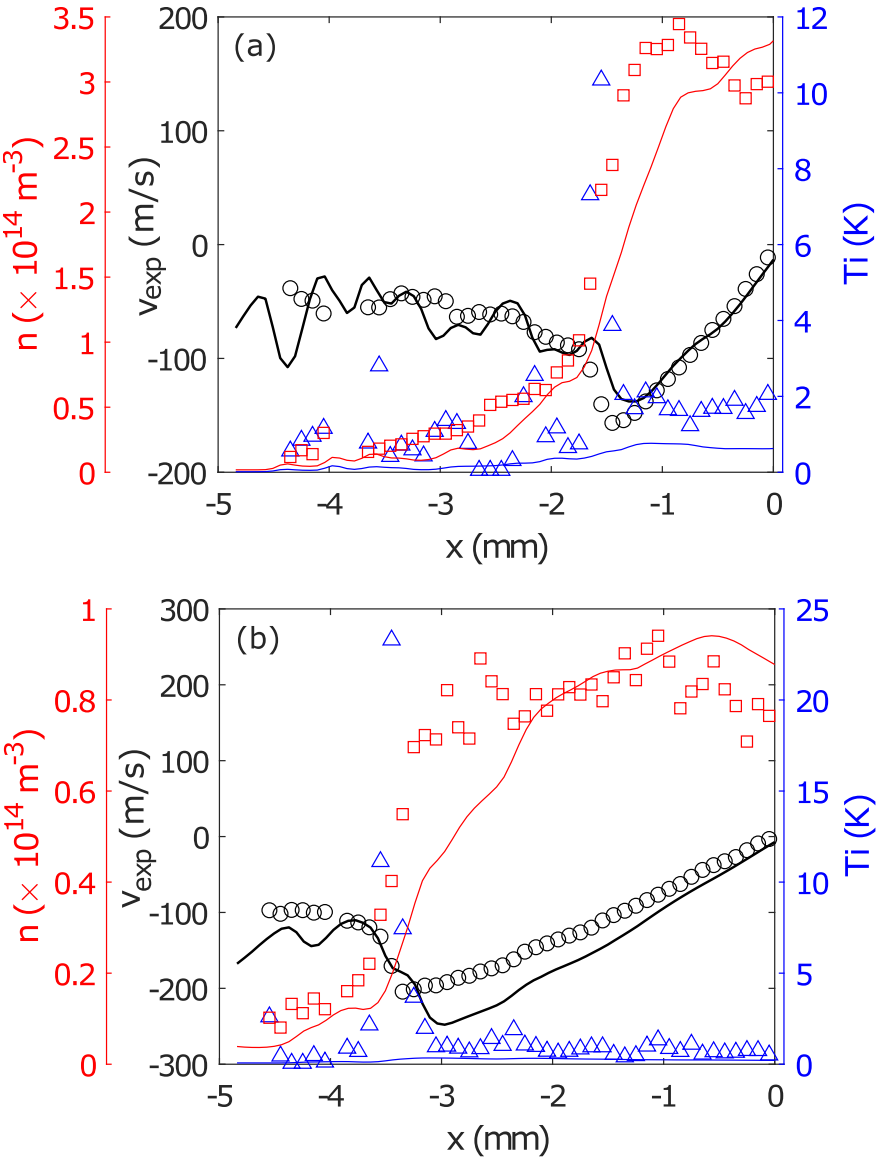

FIGURE 4.7: X-transects for the density (□), expansion velocity (○), and ion temperature (△) for the left half of the plasma at (a) 5.3 μs and (b) 12.0 μs expansion times. The jumps in density and velocity as well as the temperature spikes overlap spatially. Solid lines are numerical simulations. From [73].

4.7 Systematics

Since the localized heating shown in Figs. 4.6 and 4.7 overlaps with where there are large velocity gradients and the spectra are measured over finite regions, it is possible that the large temperatures measured in Figs. 4.6 and 4.7 are due to artificial broadening of the

spectra. Here we investigate the velocity-gradient broadening. We studied this several ways.

4.7.1 Velocity Gradient and Resolution

The first method used to determine if the large temperatures are due to artificial broadening is by estimating the temperature due to the velocity gradient over the region size. It is very approximate, but gives intuition for the underlying physics. The region size used has a width of 0.1 mm. The smallest region size that we can use is 0.026 mm, which is limited by the pixel width of the camera and the binning done when the data was taken.

Using the equation

$$k_B T_i = m\Delta v^2, \tag{4.8}$$

using $1/2 k_B T_i$ instead of $3/2 k_B T_i$ because the temperature and velocity are only measured along one axis. Δv is the velocity spread over the analysis region of 0.1 mm and is given by

$$\Delta v = \frac{dv}{dx}\Delta x, \tag{4.9}$$

where Δx is the analysis region width. This means the estimated velocity gradient broadening would give a temperature of

$$T_{broad} = \frac{m_i}{k_B}\left(\frac{dv}{dx}\right)^2 \Delta x^2. \tag{4.10}$$

Table 4.1 shows the average velocity gradient at the center of the plasma, the average ion temperature, and the calculated temperature due to velocity gradient broadening (Eq. 4.10) setting Δx = 0.1 mm. The ion temperature is roughly the same as the broadening estimate from Eq. 4.10, suggesting that broadening contributes significantly to the measured temperatures. In reality the ions are probably significantly cooler than measured.

This method of estimating the broadening gives an upper limit, as it does not take into account the spectrum, which is how we measure the temperature.

$t_{exp}(\mu s)$	$\frac{dv}{dx}$ plasma center (s^{-1})	T_i measured (K)	T_{ibroad} (K)
2.7	1.6×10^5	2.7	2.7
4	1.6×10^5	2.3	2.7
7.3	1.2×10^5	1.7	1.5
9.3	8.9×10^4	1.0	0.83
12	7.6×10^4	0.75	0.61

TABLE 4.1: Estimated broadening due to the velocity gradient over a 0.1 mm region at the center of the plasma at different expansion times.

Likewise, Table 4.2 shows the maximum velocity gradient for the shock front (as illustrated in Fig. 4.7), the corresponding temperature, and the calculated temperature due to the velocity gradient broadening using Eq. 4.10 setting Δx = 0.1 mm. Unlike with Table 4.1, the measured temperatures are significantly larger than the calculation for the velocity gradient broadening. In order to measure 11.8 K at the shock front at 7.3 μs, a region size of 0.14 mm is needed. If the resolution of our system is off and is actually 0.14 mm, then there would be approximately 3.0 K due to broadening at the center of the plasma, but we measure ion temperatures of 1.7 K. This suggests that, while there is indeed broadening, velocity gradient broadening does not account for the temperature spikes seen.

Furthermore, the velocity gradients for both the shock front and the center of the plasma are on the same order of magnitude, but with different signs. If the large temperatures in the shock front were solely due to velocity gradient broadening, then the temperatures measured in the center of the plasma would be equally large. At 4 μs, the center and the front both have velocity gradients of $1.6 \times 10^5 s^{-1}$, which yields 2.7 K of broadening from Eq. 4.10. However, the center of the plasma is 2.3 K and the shock front is 4.5 K - a factor of 2 larger.

$t_{exp}(\mu s)$	$\lvert\frac{dv}{dx}\rvert$ max (s^{-1})	T_i measured (K)	T_{ibroad} (K)
2.7	9.3×10^4	2.6	0.91
4	1.6×10^5	4.5	2.7
7.3	2.4×10^5	11.8	6.1
9.3	2.8×10^5	16.4	8.3
12	3.6×10^5	23.7	13.7

TABLE 4.2: Estimated broadening due to the velocity gradient over a 0.1 mm region in the velocity jump where the temperature spike is seen. The velocity gradients are similar to the center of the plasma as shown in Table 4.1, but the measured temperatures at the center are significantly smaller. The measured temperatures at the velocity jump are about a factor of 2 larger than the estimated broadening temperature, suggesting that broadening alone cannot account for the large temperatures measured.

Fig. 4.8 plots the measured and calculated ion temperatures for the edge and center of the plasma as a function of velocity gradient. The points are measurements while the line is from Eq. 4.10. The center of the plasma is well described by Eq. 4.10, but the measurements at the front are significantly hotter. This figure tells the same story as Tables 4.1 and 4.2, but presented differently.

4.7.2 Spectrum Analysis Varying Region Size

The second method used to determine if the measured ion temperature are artificially increased due to large velocity gradients measured over finite regions was by varying the region size in the analysis. The region widths used were 0.026 mm, 0.052 mm, 0.1 mm, 0.2 mm, 0.4 mm, and 0.8 mm.

Figure 4.9 shows the temperature transects for different region sizes in the analysis, the density transect (black line), and the velocity transect (red line). Up to a region width of 0.2 mm, the measured temperatures are roughly constant. Significant heating is seen for 0.4 mm and 0.8 mm. This behavior is expected for a system with a resolution of 0.1 mm.

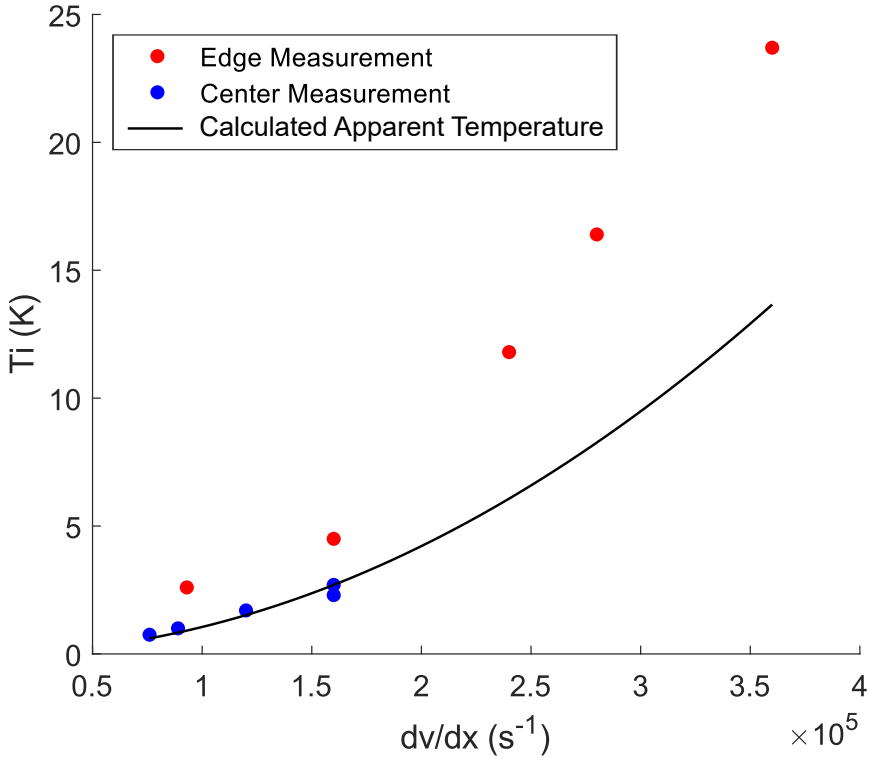

FIGURE 4.8: Measured ion temperatures for the edge (red circles) and center (blue circles) of the plasma and the calculated broadening (black line) vs. velocity gradient. The temperature at the center of the plasma is well described by Eq. 4.10, indicating that most of the temperature measured is due to artificial broadening. However, in the shock front, the temperature is significantly larger than the calculated broadening. This means that broadening does not account for all of the ion temperature.

An interesting feature of Fig. 4.9 is how the temperature spikes shift outward as the analysis region size increases. This is likely due to a combination of effects, which will be more clear after reading Section 4.7.3. Both the velocity gradient and the density gradient play a significant role in the measured ion temperature. A large density gradient can help mask the effect of a large velocity gradient. The velocity gradient is quite large where the spike is, including where the shifted spike is for the 0.8 mm region size. However, at that location, the density gradient is significantly smaller, causing the measured maximum temperature to shift outward where there is a smaller density gradient.

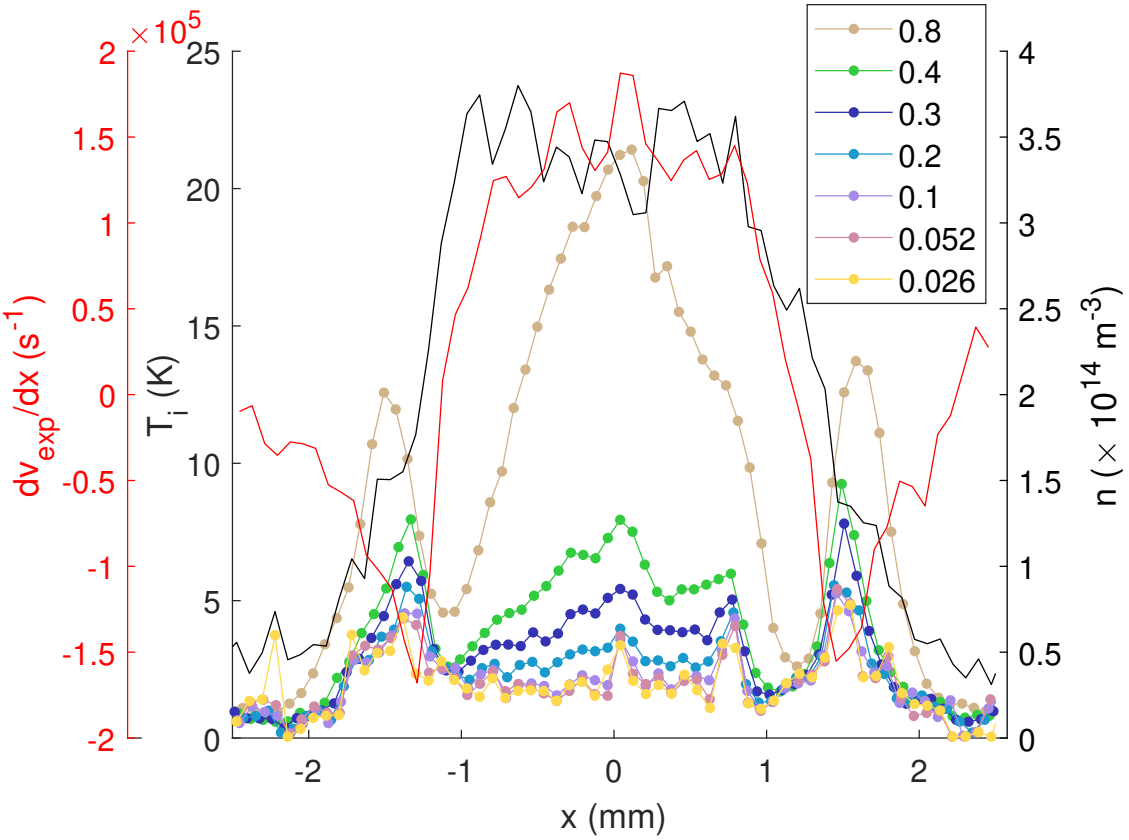

FIGURE 4.9: Ion temperature x-transects at 4 μs expansion time for different analysis regions sizes (left black axis), the ion density (black line, right axis), and the expansion velocity gradient (red line, left red axis). The analysis region widths are given in the legend in mm. The ion temperatures are the same up to a region width of 0.1 mm, which is expected since the resolution of the optical system is 0.1 mm.

4.7.3 Spectrum Simulation

The questions that we are most interested in answering are

1. What is the real temperature at the shock front? Or how much broadening do we see at the shock front, given the dv/dx and dn/dx at the shock front?

2. Holding all else constant, what Δv within an analysis region would be needed in order to lead to a broadening of the spectrum by enough to increase the measured temperature by 10 K above the actual temperature? Can that be accounted for by the region size used in the analysis and resolution of the imaging system?

We answer these questions by creating a simulated spectrum for a finite region with a velocity gradient. This is the final and most robust method for determining whether the large temperatures measured are real or due to artificial broadening.

Description of the Program

The spectrum simulation builds on the spectrum model developed by Grant Gorman in [25]. This model obtains the fluorescence signal by solving the rate equations. It is a powerful model that can also simulate the spectrum in a magnetic field and determine the spin polarization of the ions. Because the experiments conducted for this thesis only use unmagnetized plasmas, velocity-gradient broadening of magnetized ions is beyond the scope of this study.

The spectrum simulation divides the analysis region into sub-regions that are small enough such that broadening within each sub-region due to the spread in hydrodynamic or mean velocity is negligible, as illustrated in Fig. 4.10. Each sub-region has a different spectrum corresponding to its mean density, velocity, and temperature. The spectrum for the entire region is the average spectrum of the sub-regions. The values of important quantities for the first and last sub-region are given by

$$[n_0, \;\; n_0 + \Delta n] \tag{4.11}$$

$$[T_{i0}, \;\; T_{i0} + \Delta T_i] \tag{4.12}$$

$$[v_0 - \Delta v/2, \;\; v_0 - \Delta v/2], \tag{4.13}$$

where $\Delta n, \Delta T_i$, and Δv are the respective spread in density, ion temperature, and velocity over the region due to the corresponding gradient and region width. The density, temperature, and velocity are linearly distributed throughout the region. The density and

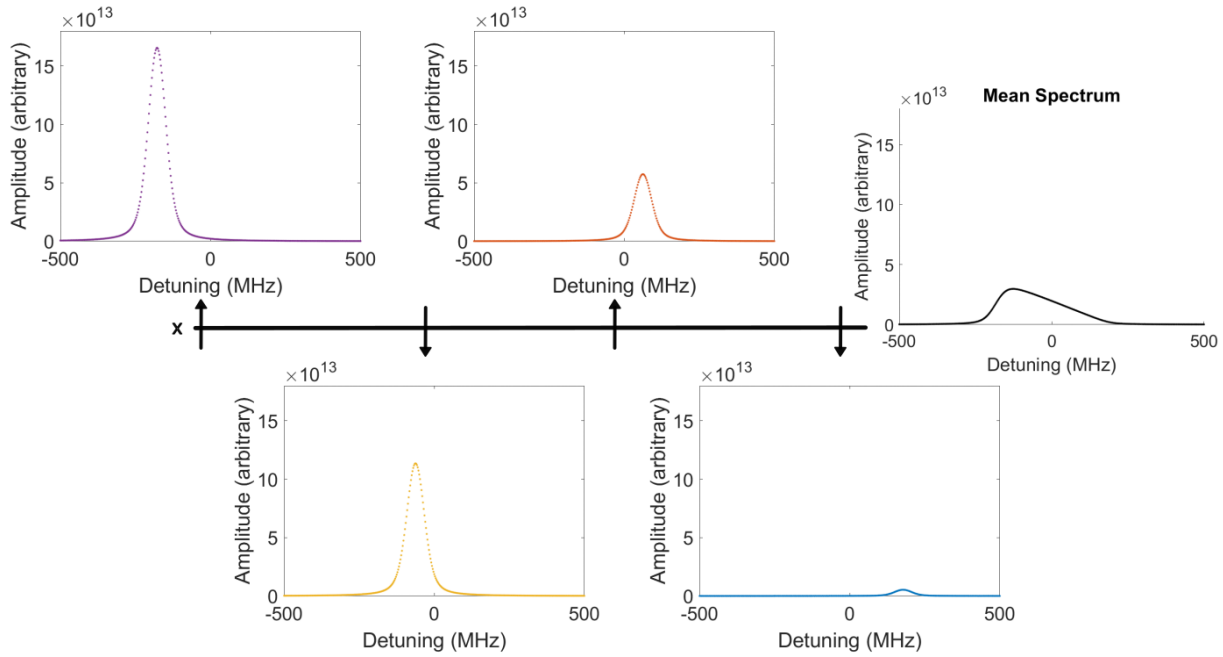

FIGURE 4.10: Illustration of what the spectrum simulation does. Over an analysis region, the velocity, density, and temperature can vary significantly. The simulation divides a region into many sub-regions that are small enough to ignore broadening due to spread in hydrodynamic velocities. It creates a spectrum for each sub-region corresponding to its density, velocity, and temperature, then creates the spectrum for the entire region from the mean of the sub-spectra. This can result in a region spectrum that deviates from a Voigt profile, like the one in this figure. In this figure, the velocity and density spread are exaggerated to illustrate the point.

temperature are not centered around n_0 or T_{i0} because if they are small and the gradients are large, centering the density and temperature around n_0 and T_{i0} could cause them to become negative, which is not physical. The velocity, however, is centered around v_0. For simplicity, $v_0 = 0$ for all cases in this thesis, but the simulation works for $v_0 \neq 0$.

The program then creates the spectrum for each sub-region using that sub-region's velocity, density, and temperature. The spectrum for the entire region is determined from the mean of the spectra for the sub-regions.

Figure 4.10 shows the spectra at four locations in a sample analysis region, corresponding to four different densities and velocities due to the gradients. On the right, the figure

shows the mean spectrum from all of the spectra in the region. None of the spectra in our data look like the mean spectrum in Fig. 4.10 due to greatly exaggerated gradients to clearly illustrate the point.

While the simulation was created to be as general as possible, and thus can include a temperature gradient, for our experiments, we assume that the temperature is uniform. For completeness, we still explore how a temperature gradient influences the measured spectrum in the discussion of this model.

Proof of Concept

To demonstrate that the spectrum simulation works, it was tested for no gradients with a variety of initial temperatures. In figures like Figs. 4.11 and 4.12, the left side shows four different sub-region spectra and the right shows the mean spectrum with the fit. For the left figures, the legend refers to the sub-region index.

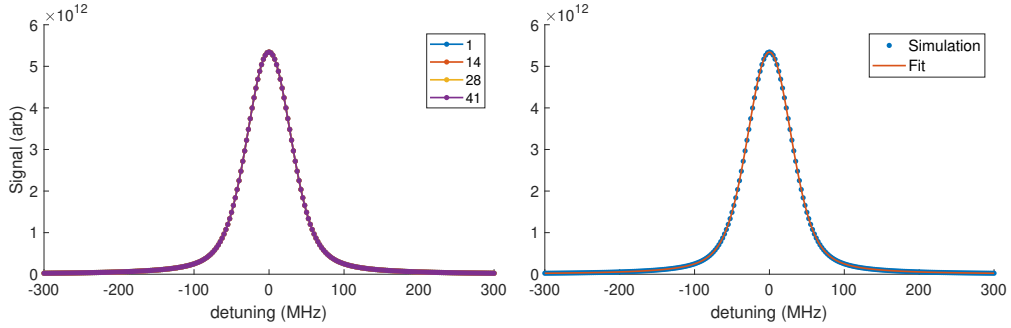

FIGURE 4.11: Spectrum simulation with sample spectra from four different sub-regions (left, indices for the sub-regions given in the legend) and the mean spectrum with the Voigt profile fit (right). The initial conditions are $n_0 = 1 \times 10^{14}\, m^{-3}$ and $T_{i0} = 1$ K, with no gradients.

Figure 4.11, $n_0 = 1 \times 10^{14}$ m^{-3}, $T_{i0} = 1$ K, $v_0 = 0$ m/s, and all gradients = 0. Only one spectrum can be seen on the left side, which is expected for no velocity gradient. The density, velocity, and temperature from the fit to the mean spectrum exactly match the input values, also as expected.

Varying Velocity

When adding in a velocity gradient while holding temperature and density constant, with a sufficiently large gradient, one would expect the mean spectrum to become a top hat. This is shown in Fig. 4.12 with a Δv of 100 m/s, showing that the spectrum simulation program works as it should. For T_i = 1 K, a Δv of 100 m/s gives a measured ion temperature of 14 K, or it broadens the spectrum by 13 K.

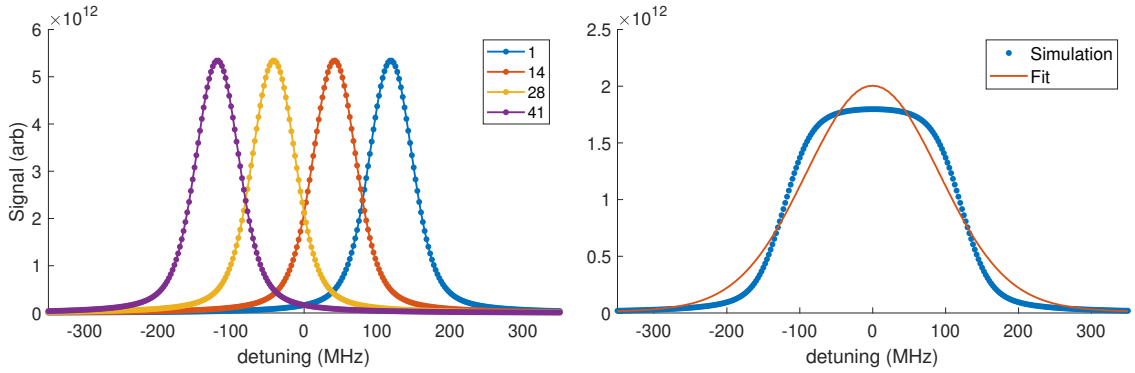

FIGURE 4.12: Simulated spectrum with $\Delta v = 100$ m/s and $T_{i0} = 1$ K. This creates a mean spectrum with a top-hat shape. The ion temperature extracted from the fit to the mean spectrum is 14 K, yielding 13 K of artificial broadening due to the velocity gradient.

However, as Fig. 4.13 shows, the top hat from the velocity gradient can be hidden if the temperature is greater. For an ion temperature of 10 K, the measured temperature is 21 K, giving 11 K of broadening for a velocity gradient of 100 m/s. The actual 10 K ion temperature gives 2 K less broadening than the actual 1 K ion temperature, both of which have Δv = 100 m/s. Additionally, the mean spectrum for the hotter ions is well described by the Voigt profile, indicating that how the gradients impact the line shape is complicated and not immediately obvious when looking at the spectra alone.

In the experimental data, we do not see spectra that are clearly flat on the top, like in Fig. 4.12. This is likely due to two reasons: first, the experimental data is significantly noisier than the simulations. Second, likely there is a significant contribution to the measured temperature from real heat, which masks the top hat effect, as shown in Fig. 4.13

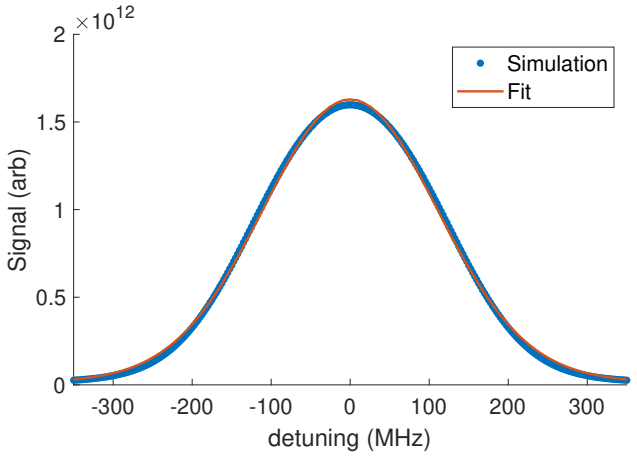

FIGURE 4.13: Mean spectrum for Δv = 100 m/s and $T_{i0} = 10$ K. Because T_{i0} is relatively large, the spectrum maintains a Voigt profile, but the measured temperature is 21 K, giving 11 K of artificial broadening.

Figure 4.14 shows the simulated spectra for cold (50 mK) ions with varying velocity spreads of Δv = 10, 50, 100, and 200 m/s. As the velocity gradient increases, the lineshape changes and the spectrum becomes significantly wider.

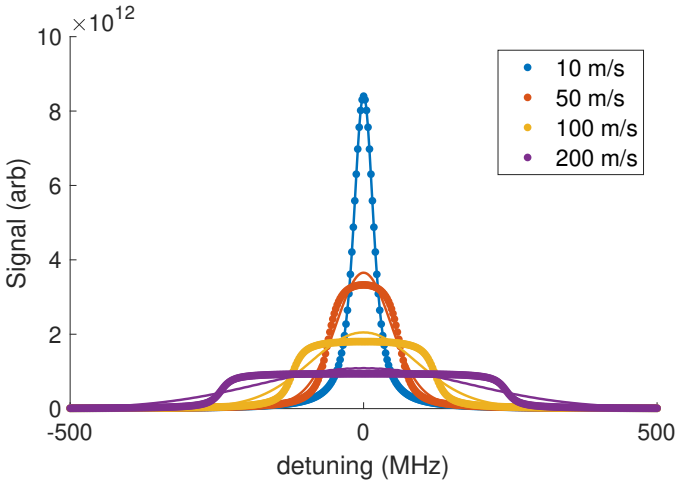

FIGURE 4.14: Simulated spectra for cold (50 mK) ions varying Δv. The lineshape changes as the velocity gradient increases.

The velocity gradient broadening is further illustrated in Figure 4.15, which shows the difference between the temperature measured from the spectrum and the actual temperature as a function of velocity gradient for a 0.1 mm wide region. The legend indicates the different actual ion temperatures used. At low temperatures, even a small velocity gradient has a significant impact on the measured temperature. For the 0.01 K real temperature, even at the smallest velocity gradients, the temperature increases by at least a factor of 10. All real ion temperatures have 100 mK of broadening at

a gradient of 1×10^5 s^{-1} - which causes the measured temperature to double for the 100 mK real temperature. For a gradient of 1×10^5 s^{-1}, the temperature is broadened by about 10 K for all cases.

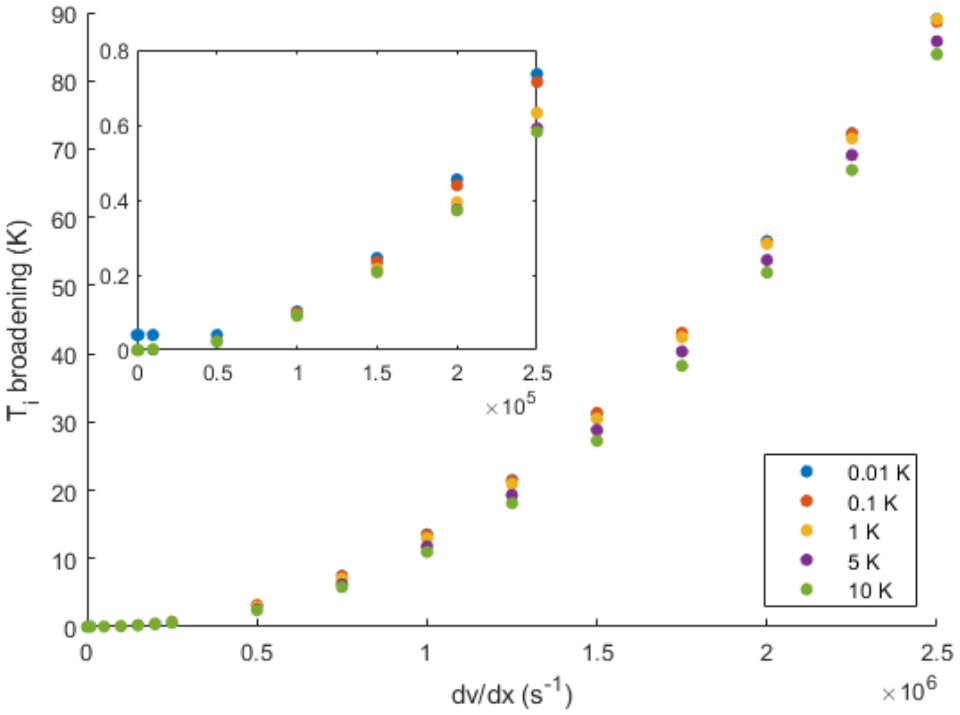

FIGURE 4.15: Broadening (T_i measured - T_{i0}) as a function of velocity gradient using the spectrum simulation. The input ion temperature is given in the legend. This shows that, for small ion temperatures, the vast majority of the measured temperature is due to velocity gradient broadening, but for larger temperatures, the broadening is not significant until larger gradients.

Varying T_i

We are also interested in how the ion temperature impacts the measured temperature in the simulated spectra. Figure 4.16 shows the simulated spectra for an ion temperature range of 1, 5, and 10 K. The temperatures extracted from the fit to the simulated spectra are 0.53, 2.00, and 3.73 K, respectively which is close to $\Delta T_i/2 + T_i0$ - the mean temperature over the region. For $\Delta T_i = 1$ K, the measured temperature overestimates the mean

temperature while for $\Delta T_i = 10$ K, the measured temperature underestimates the mean temperature.

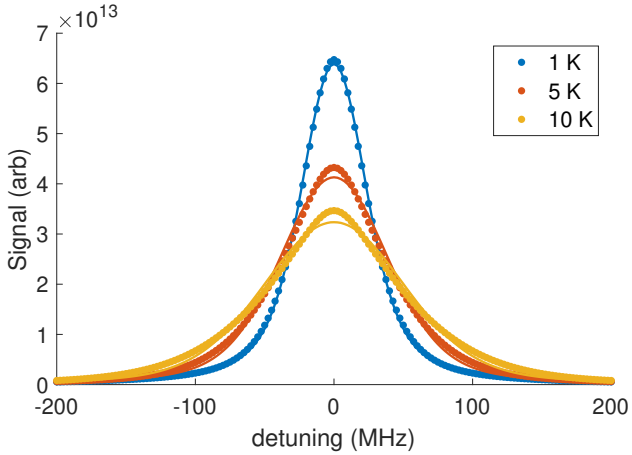

FIGURE 4.16: Simulated spectra with fits to a Voigt profile for varying the ion temperature spread (indicated in the legend) while holding the velocity and density constant at 0 m/s and 10×10^{14} m^{-3} respectively. While the spectra deviate from a Voigt profile, the Voigt profile still describes the spectrum well. The measured density underestimates the actual density, but by > 5%, which is within the experimental tolerance and would be considered the same.

An interesting feature of varying the ion temperature is the impact on the measured density. Figure 4.16 uses uniform ion densities of $10 \times 10^{14} m^{-3}$. In both cases, the measured density underestimates the actual density, but only by 0.8% and 3.5% respectively. This is within our experimental tolerance, so we would consider it the same.

Another interesting feature is how the spectrum deviates from the expected Voigt profile. The center is more sharply peaked and the wings are underestimated by the fit. However, the spectrum is still reasonably well described by the Voigt profile. This demonstrates that an ion temperature gradient does not impact the line shape as much as a much as a velocity gradient.

Varying Density

Finally, we are interested in how a density gradient impacts the temperature measurement. Having a density gradient alone does not change anything.

Adding a velocity gradient to the density gradient makes the spectrum more interesting, as shown in Figs. 4.17 and 4.18. For relatively small Δn and large Δv, the mean spectrum looks trapezoidal, as shown in Fig. 4.17. For large Δn and Δv, the mean spectrum becomes triangular, as sown in Fig. 4.18.

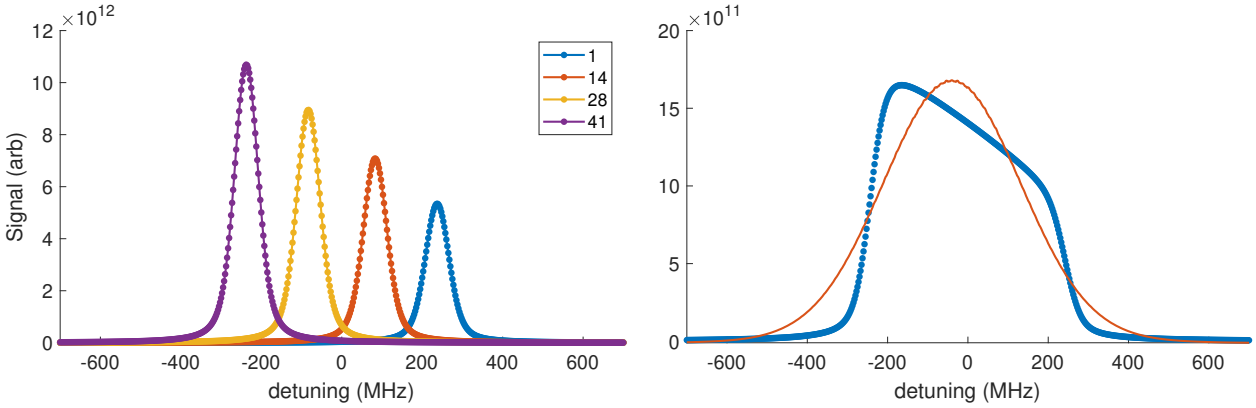

FIGURE 4.17: (Left) Sample spectrum for four different sub-regions with the region index indicated in the legend and (Right) the simulated spectrum with Voigt profile fit for $n_0 = 1 \times 10^{14}$ m^{-3}, $\Delta n = 1 \times 10^{14}$ m^{-3}, $T_i = 1$ K, and $\Delta v = 200$ m/s. The mean spectrum deviates significantly from a Voigt profile, an is trapezoidal in shape. The measured temperature is 52 K, which yields 51 K due to velocity gradient broadening.

The velocity gradient combined with the density gradient does have a significant impact on the temperature measurement. In both cases, $n_0 = 1 \times 10^{14}$ m^{-3}, $T_i = 1$ K, and $\Delta v = 200$ m/s. For $\Delta n = 1 \times 10^{14}$ m^{-3} (Fig. 4.17) and 30×10^{14} m^{-3} (Fig. 4.18), the measured temperatures are 52 K and 29 K, respectively. This yields 51 K and 28 K of broadening. There is significantly less broadening as the density gradient increases. This is significant because in the shock front of our experiments, as shown in Fig. 4.7, the large velocity gradients overlap with large density gradients, which helps mitigate the effects of the broadening due to the velocity gradient.

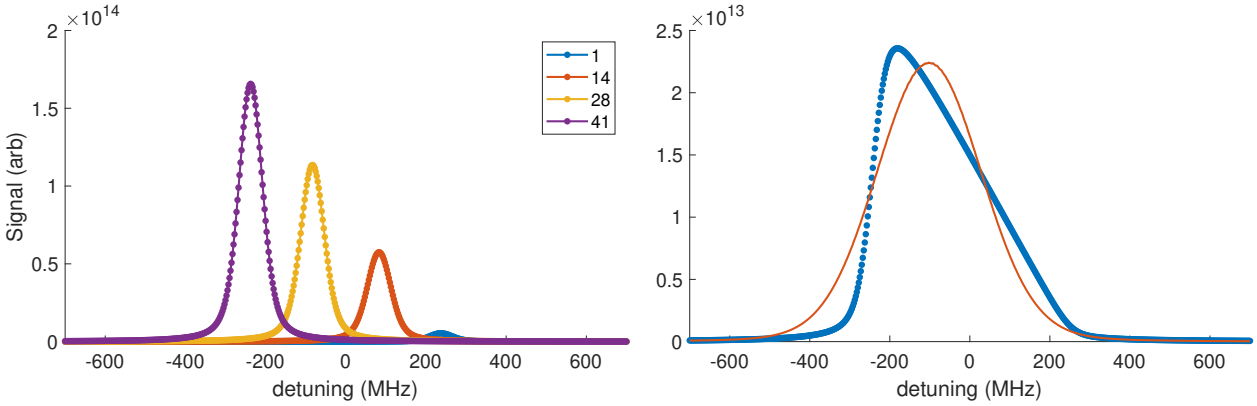

FIGURE 4.18: Simulated spectrum for $n_0 = 1 \times 10^{14}$ m^{-3}, $\Delta n = 30 \times 10^{14}$ m^{-3}, $T_i = 1$ K, and $\Delta v = 200$ m/s. The measured temperature is 29 K, giving 28 K due to artificial broadneing.

Another note is the density from the fit to the simulated spectrum is slightly higher than the density of $n + \Delta n/2$ that is seen in the case without a velocity gradient. This is only a 6% and 0.9% error respectively, which is within our experimental tolerance.

4.7.4 Main Questions

Here I return to the questions posed at the beginning of this section.

1. Holding all else constant, what Δv do we need to broaden by 10 K? Can that be accounted for by the region size used in the analysis and resolution of the imaging system?

For a 0.1 mm region size, to get Δv = 100 m/s, the gradient has to be 1×10^6s$^{-}1$. The largest velocity gradient seen in the data is 6×10^5 s^{-1}, which is about a factor of 2 less than the velocity needed to cause 10 K of broadening.

The ion temperatures are over 40 K when we see those gradients. As Fig. 4.15 shows, in order to get 40 K of broadening, the velocity gradient has to be about 1.7×10^6 s^{-1}. indicating that the temperature spike, while partially due to the broadening, is not only due to

the broadening. In order for the temperature to be completely caused by the broadening, the velocity gradient needs to be a factor of 3 larger than the largest velocity gradients in the data. This cannot be accounted for by the region size or the resolution. While some of the temperature is due to artificial broadening, there is still significant heating in the shock front.

Additionally, Fig. 4.15 assumes uniform density, but as Fig. 4.7 shows, there is a significant density gradient where there is the large velocity gradient and temperature spike. As was shown above, adding a density gradient to the velocity gradient decreases the broadening. This means that in the shock front, the density gradient will help mitigate the impact of the velocity gradient on artificial broadening.

2. What is the real temperature at the shock front? Or how much broadening do we see at the shock front, given the dv/dx and dn/dx at the shock front?

The largest dv/dx in the data is 4.95×10^5 s^{-1}. This corresponds to $dn/dx = 2.67 \times 10^{17}$ m^{-4}. Using those values in the spectrum simulation program, the broadening is at worst 5.1 K, and does not account for the 29 K measured.

To achieve a measured temperature of 29 K from the fit to the simulated spectrum using $dv/dx = 4.95 \times 10^5$ s^{-1} and $dn/dx = 2.67 \times 10^{17}$ m^{-4}, the real ion temperature is T_{i0} = 25 K.

4.7.5 Future work

The spectrum simulation that I developed can be a subject of future research into real spectra versus measured spectra. There are several directions this research can go as well as ways to improve the simulation.

It would be nice to add in fitting capabilities given a velocity, density, velocity gradient, and density gradient to extract the real ion temperature. While a Voigt profile can easily be fit to the simulation, fitting the simulation to the measured spectrum would be extremely powerful.

Currently the simulation only works for linear densities and velocities. Generalizing the program so any density and velocity distribution can be used would make it significantly more powerful. This would allow for studies such as how the kink in the velocity transect impacts the spectrum.

Finally, adding in temporal effects would be interesting. In the UNP experiments, we image the plasmas over a finite time. If there is significant acceleration, then there could be artificial broadening if the imaging time is too large.

4.8 Conclusions

We have presented evidence of wave steepening and signatures of shock formation in exponential UNPs, establishing that by sculpting the initial density distribution, shockwaves can develop in UNPs. As the plasma expands, wave steepening is seen in both the density and velocity transects as a large gradient develops. These features overlap with regional ion heating. Additionally, the Mach number exceeds unity

While the question of whether a shockwave forms has been answered, this research has sparked several other interesting questions, including: What impacts the shock development? Is it caused by kinetic effects or is it a hydrodynamic/collisional effect? This is the subject of Chapter 5. Additionally, expanding the field of view for the plasma imaging would allow further study of the shock propagation and whether is continues to grow or eventually dissipates.

Chapter 5

Shockwave Characterization

Chapter 4 established that wave steepening and shockwaves can develop in exponential UNPs. In this chapter, we further study the shock development in UNPs, investigating what impacts shock formation. To test whether it is due to hydrodynamics or is a kinetic effect, we vary the density, the shape, and the electron temperature.

A different parameter is varied in each section. Each section includes two figures. The first is a grid figure that shows the density (top row), velocity (middle row), and ion temperature (bottom row) x-transects at three different points in the plasma evolution. All of these figures will be called the "x-transect grid." The velocity is scaled by $v_{IAW}(t)$ using $T_e(t)$ from the SPRUCE simulation (described in Sec. 4.2). All of the data sets at a similar time scaled by τ_{exp} are plotted together for three different times in the three columns.

The second figure in each section shows the Mach number as a function of time for each set on a different subplot. All of these figures will be called "Mach number evolution." As done for the Mach number analysis in Sec. 4.5, the solid data calculates $v_{IAW}(t)$ using $T_e(t)$ from the SPRUCE simulation for that data set. The upper bound is calculated using the estimate of $T_e(t)$ from adiabatic expansion, given by Eq. 4.7. The lower bound uses $T_e(0)$, which is set by how far the photoionizing laser is detuned above the ionization threshold.

5.1 Varying Density

To see if shock development is due to a kinetic effect, we vary the initial density by a factor of 4. This will indicate if collisions impact shockwave development. The density was varied by decreasing the photoionization beam's power so fewer atoms are ionized. This allows the density distribution to be the same, only varying one parameter.

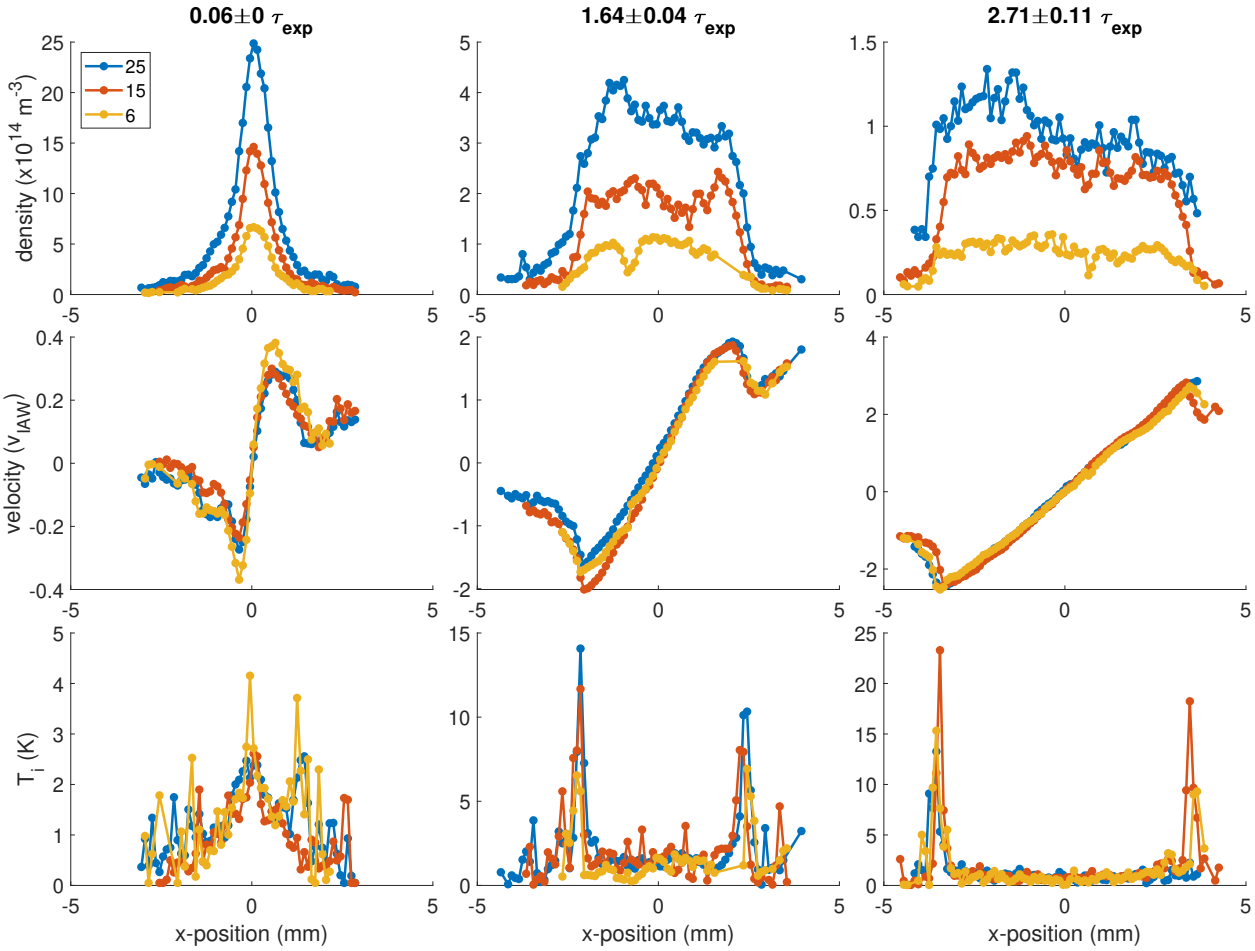

FIGURE 5.1: The density (top), velocity (middle) and ion temperature (bottom) x-transects for initial peak densities of 25 (blue), 15 (red), and 6 (yellow) $\times 10^{14}$ m^{-3}. The velocity is scaled by v_{IAW}. Each column shows the three data sets at similar expansion times scaled by τ_{exp}. While the peak density is different, there is not an appreciable difference in the plasma shape, velocity, or temperature, indicating that the collisionality does not play a role in the shock development for the range of densities in this experiment.

Figure 5.1 shows the x-transect grid described above for initial peak densities of 25 $\times 10^{14}$ m^{-3} (blue), 15 $\times 10^{14}$ m^{-3} (red), and 6 $\times 10^{14}$ m^{-3} (yellow) for 0.1 τ_{exp}, 1.6 τ_{exp}, and 2.7 τ_{exp}. While the peak density is different, there is not an appreciable difference in the density distribution or the velocity and ion temperature. This indicates that collisions do not play a role in the shock development over the range of densities used in this experiment. Hydrodynamic descriptions tend to break down when the mean free path (MFP) becomes larger than the relevant length scale. Varying the density, and thus the MFP, by a factor of four without seeing any difference in behavior suggests that the sock behavior is not sensitive to or indicative of breakdown of the hydrodynamic description caused by kinetics.

The velocity transects collapse onto universal curves, showing that $v_{IAW} = \sigma_/\tau_{exp}$ is a useful scaling factor. As discussed in Secs. 3.1 and 3.2, $\tau_{exp} = \sqrt{\frac{m_i}{k_B T_{e0}}}\sigma_0$ (Eq. 3.8) comes from the hydrodynamic expansion of a Gaussian plasma due to the electron thermal pressure gradient. One of the key results discussed in Sec. 3.3.3 was that, while exponential UNPs do not have analytic solutions describing their expansion, they can be described by similar expansion parameters, like σ_0 and τ_{exp}. Thus the universality seen in the velocity transects scaled by v_{IAW} suggests that the electron thermal pressure gradient could play a role in the shock development.

Figure 5.2 shows the Mach number evolution for the three different initial densities. The Mach number exceeds and remains above 1 in all three cases. There is not a significant difference between the three densities, further indicating that collisions do not impact shock development over the density range used, and that the shock development is likely due to a hydrodynamic effect.

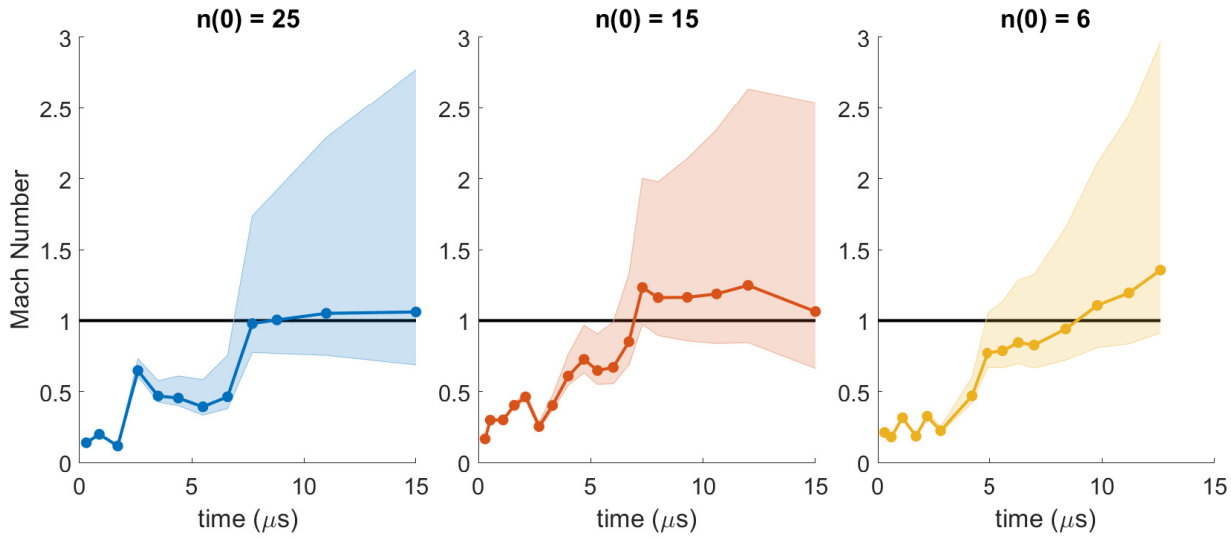

FIGURE 5.2: The Mach number as a function of time for initial densities of 25 (left), 15 (middle), and 6 (right) $\times 10^{14}$ m^{-3}. In all three cases, the Mach number exceeds and remains above 1. There is not a significant difference between the Mach numbers for the three densities studied in this experiment.

5.2 Varying Te

Since the hydrodynamic acceleration of a UNP, given by Eq. 3.5, depends on $\nabla n/n$ and T_e, we first vary the initial electron temperature to see if it drives the formation of shockwaves. The four temperatures used were 60 K, 160 K, 320 K, and 454 K. Using higher temperatures becomes difficult because τ_{exp} becomes very small, presenting challenges for imaging the plasma.

Figure 5.3 shows the x-transect grid described above. The initial electron temperature of 60 K is blue, 160 K is red, 320 K is yellow, and 454 K is purple. The three columns show 0.1 τ_{exp}, 0.9 τ_{exp}, and 2.5 τ_{exp}. There is not a significant difference in the density transect evolution.

The velocity transects have the same shapes for all four $T_e(0)$. For the three higher temperature sets, the velocity transects collapse onto universal curves, showing that they are still dominated by hydrodynamics and the electron thermal pressure gradient. Wave

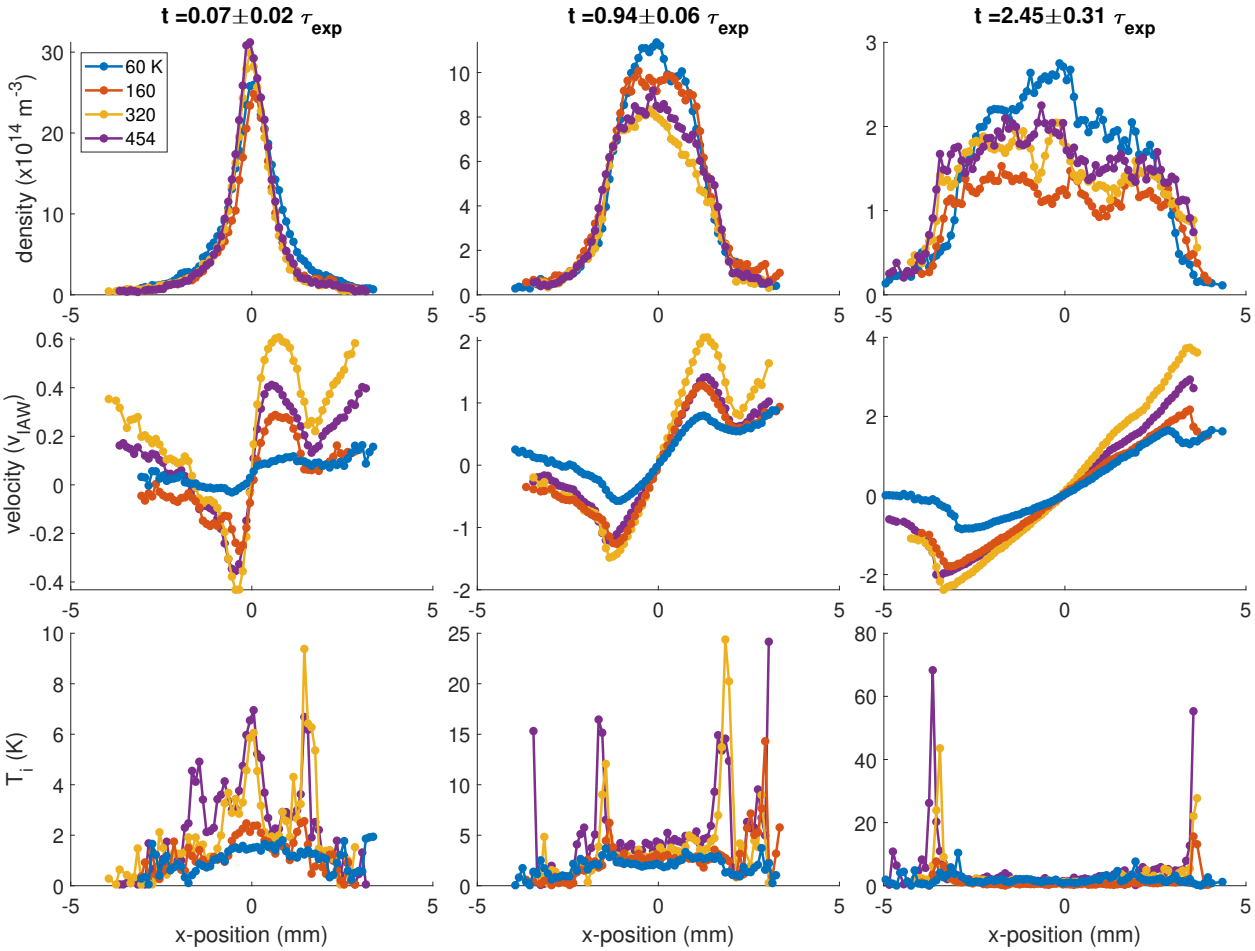

FIGURE 5.3: The density (top), velocity (middle) and ion temperature (bottom) x-transects for initial electron temperatures of 60 K (blue), 160 K (red), 320 K (yellow), and 454 K. The velocity is scaled by v_{IAW}. Each column shows the three data sets at similar expansion times scaled by τ_{exp}. There is not an appreciable difference in the density evolution. The velocity transects collapse onto a universal curve for the higher temperature data with the 60 K data still having the same profile, just not the same slope or extrema. Spikes in the ion temperature develop in all four sets, with more heating in the higher T_e data.

steepening is seen in the velocity transects for all four sets. The velocity transect for the 60 K data consistently has a significantly smaller gradient than the three other higher temperature sets. The 60 K data also goes to 0 m/s on the left edge of the plasma while the other three sets have a higher velocity. The reason for this difference is unclear.

The initial ion temperature is much higher for the 320 K and 454 K data. This is likely

due to velocity gradient broadening as described in Sec. 4.7. While the velocity transects shown have the same slope for the three higher electron temperature sets, the unscaled velocity is higher for the higher temperature data since $v_{IAW} \propto \sqrt{T_e}$ (Eq. 4.3). The unscaled velocity for the 60 K set is still lower than the other three sets. The larger velocity gradient in the higher initial electron temperature sets will cause more velocity-gradient broadening, thus higher temperatures at the center of the plasma initially.

As the plasma expands, the spike in the temperature develops in all four sets, but is much more pronounced for the higher temperature data. Part of this is due to broadening, but the spectrum simulation described in Sec. 4.7.3 shows that broadening does not account for all of the measured temperature.

Figure 5.4 shows the Mach number evolution for this study. In all four cases, the Mach number exceeds one and stays above one for several μs, until the shock front propagates off the camera's field of view. This shows that the electron temperature does not have a significant impact on the shock formation.

5.3 Varying Shape

Since the density does not impact the shock formation, the shockwaves are likely due to a hydrodynamic effect rather than a kinetic effect. The electron temperature also does not impact the shock formation, so it likely points to the density distribution, especially since shocks are not seen in Gaussian UNPs with the same electron temperatures and peak densities used in these exponential UNP experiments. In this section, we vary $\nabla n/n$ in two ways: vary the MOT current and vary the atom expansion time before photoionization.

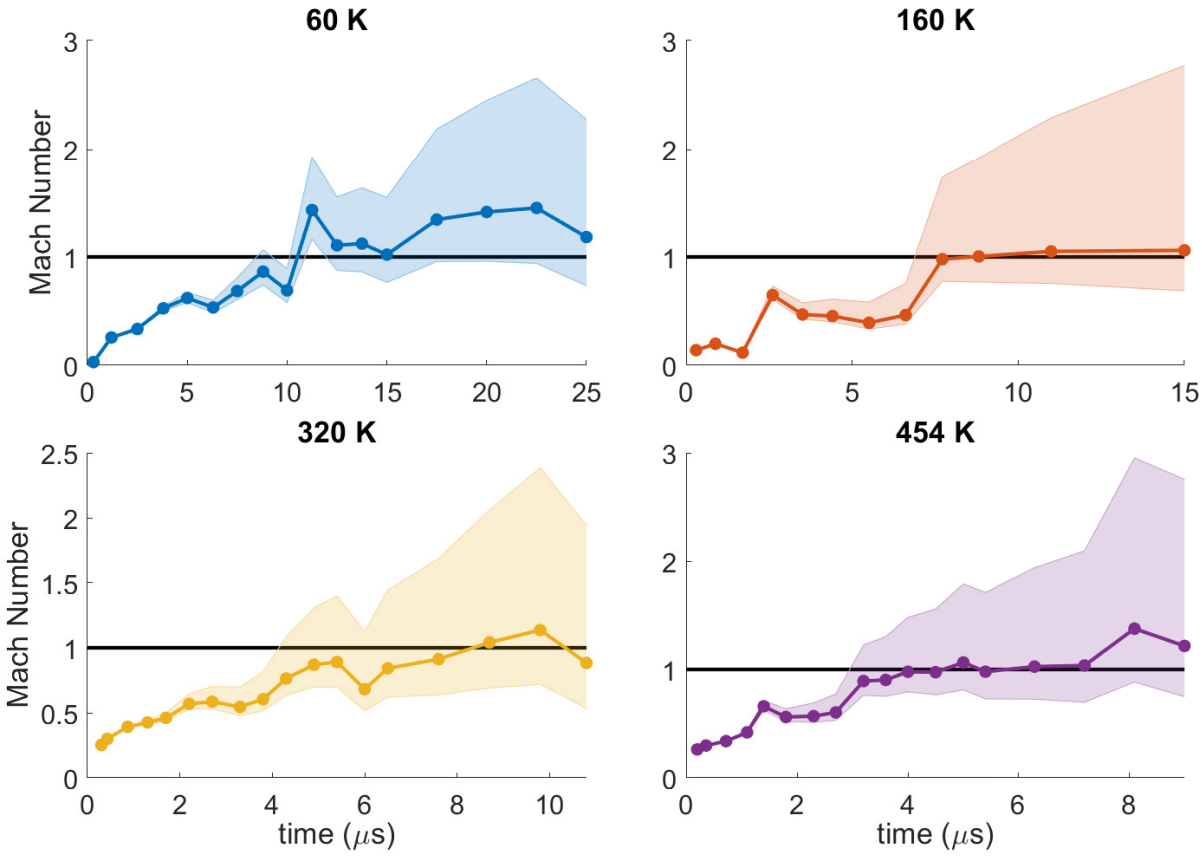

FIGURE 5.4: The Mach number as a function of time for initial electron temperatures of 60 K, 160 K, 320 K, and 454 K. In all three cases, the Mach number exceeds and remains above 1

.

5.3.1 Varying MOT Current

First, the MOT current is varied. The size of the atomic cloud in the magnetic trap is determined by the magnetic field gradient. This is controlled by the amount of current that is run through the anti-Helmholtz coils uses to create the MOT and magnetic trap. Decreasing the MOT current increases the plasma size while maintaining the exponential profile. For an exponential plasma, $\nabla n/n = 1/\sigma_0$, so decreasing the MOT current decreases $\nabla n/n$, which decreases the acceleration due to the electron thermal pressure gradient (Eq. 3.2).

In the experiments discussed in Chapters 3 and 4, 85 A was used for the MOT coils.

This is the maximum current that the power supply can output. In this experiment, we used MOT currents of 85 A, 60 A, and 40 A. As the current decreases, the peak density decreases, so we matched the peak density in the higher current experiments to the 40 A data set by adjusting the power in the photoionization beam.

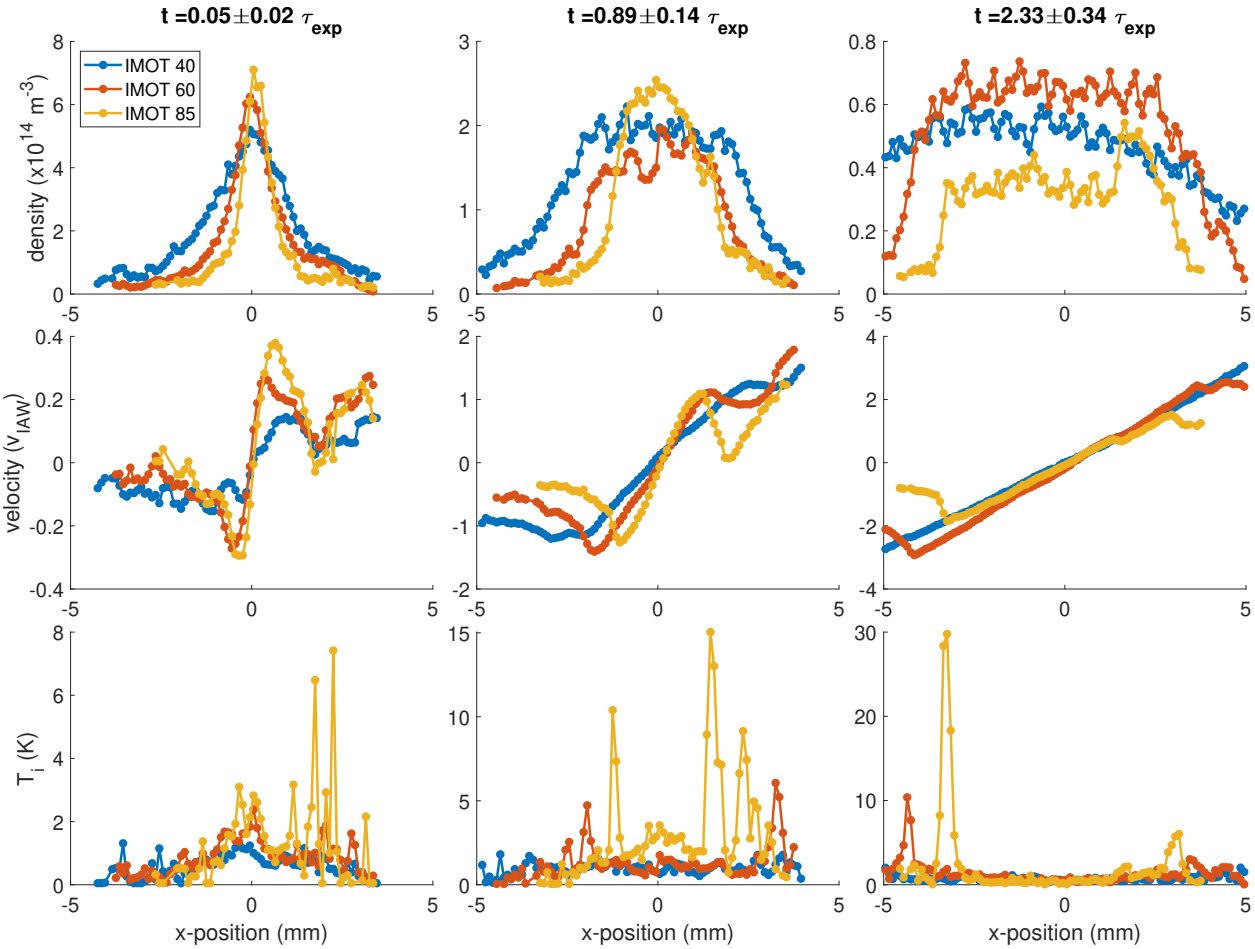

FIGURE 5.5: The density (top), velocity (middle) and ion temperature (bottom) x-transects for different density distributions MOT currents of 40 A (blue), 60 A (red), and 85 A (yellow). The MOT current was varied to vary the density distribution. The velocity is scaled by $v_{IAW}(t)$. Each column shows the three data sets at similar expansion times scaled by τ_{exp}. Wave steepening is seen in the density and velocity transects for the 60 A and 85 A sets, but not the 40 A set, suggesting that the density distribution is essential in shockwave formation.

The x-transect grid is shown in Fig. 5.5 for 0.05 τ_{exp}, 0.9 τ_{exp}, and 2.3 τ_{exp} with MOT currents of 40 A (blue), 60 A (red), and 85 A (yellow). The density transects generally

have the same exponential shape with the size increasing as the MOT current decreases. The left side of the 40 A set is more linear. This could be due to non-uniformities in the ionization beam or water spots on the windows, as described in Sec. 2.3.5.

The 60 A and 85 A sets expand similarly, forming a plateau with a sharp density jump. This is not seen in the 40 A set while it is on the camera. Since it is much larger than the other plasmas, the 40 A set expands off the field of view fairly quickly. However, from how the plasma evolves while it is in view, it is not expected to show signs of wave steepening in the density.

The velocity transects for the 60 A and 85 A sets collapse on universal curves with the extrema locations corresponding to the location of the jump in density. Wave steepening also develops in the velocity x-transects for these two sets. The velocity transect for the 40 A does not show wave steepening.

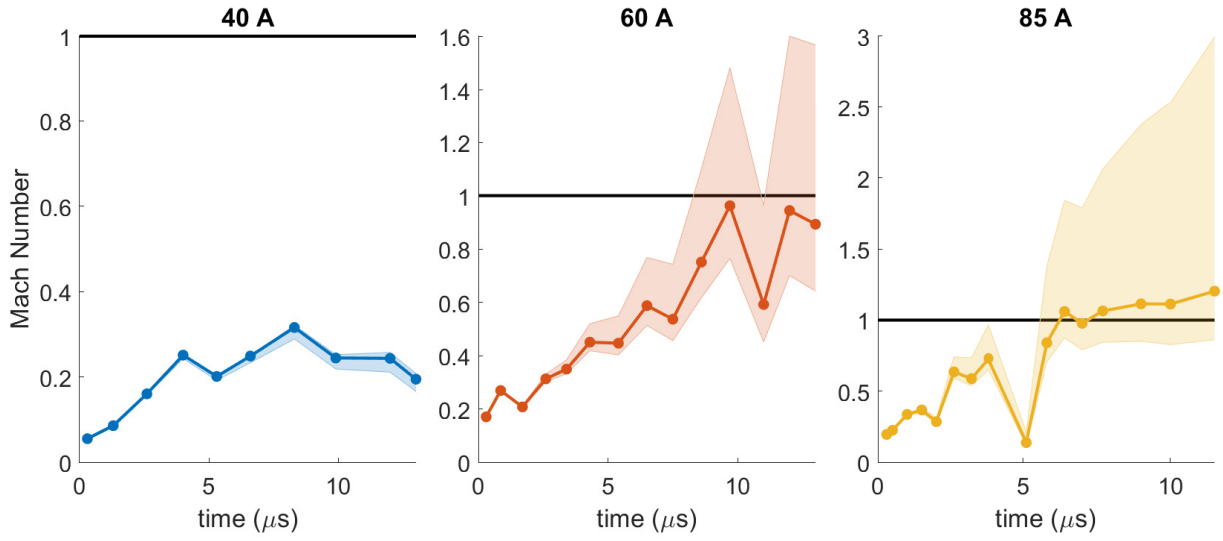

FIGURE 5.6: The Mach number as a function of time for MOT currents of 40 A (left), 60 A (middle), and 85 A (right). Only in the 85 A case does the Mach number exceed 1. In the 60 A case, it approaches 1, but does not pass 1. In the 40 A case, the Mach number remains significantly below 1.

The temperature transects are most illuminating. Large temperature spikes of 15-30

K develop in the 85 A set. The 60 A set also has temperature spikes, but they are much smaller at around 5-10 K. The 40 A set does not develop temperature spikes.

The Mach number evolution is shown in Fig. 5.6. The 85 A set exceeds Mach 1 and stays above 1 for several μs. The 60 A case approaches 1, but does not achieve Mach 1. The 40 A case has a maximum Mach number of approximately 0.3. A shockwave does develop in 85 A case. The 60 A set shows signs that a shockwave could develop, although the Mach number may not actually exceed 1. The 40 A set does not show any signs of shockwave development. This shows that the density distribution does play a role in shockwave development.

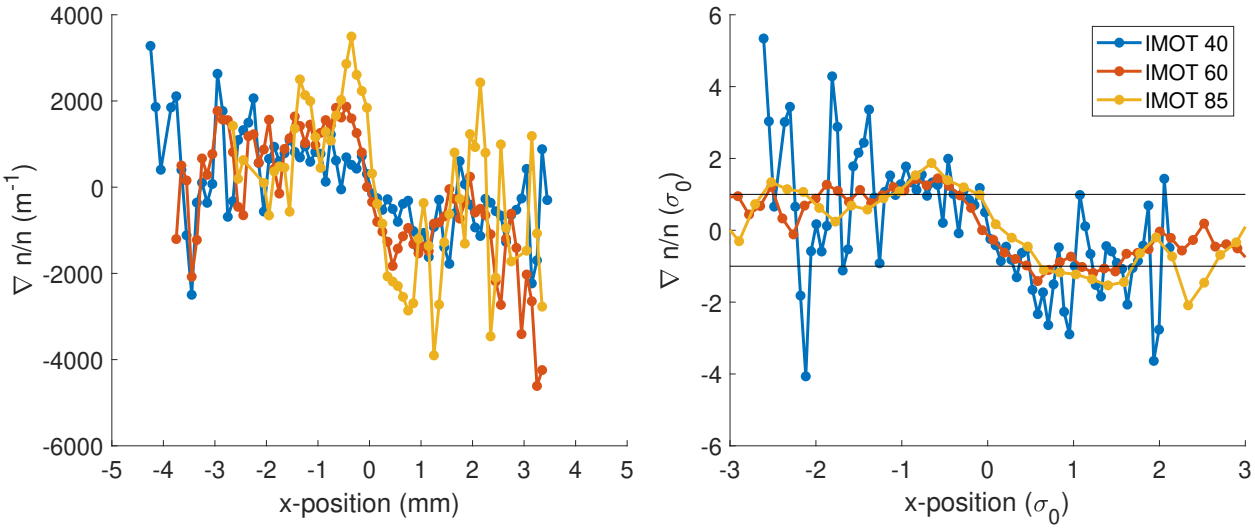

FIGURE 5.7: Initial $\nabla n/n$ x-transect scaled by $1/\sigma_0$ for exponential UNPs formed using MOT coil currents of 40 A (blue), 60 A (red), and 85 A (yellow). For a perfect exponential UNP, this should be a step function at 1 for $x < 0$ and -1 for $x \geq 0$, which is not seen in the data, confirming that the UNPs are not perfectly exponential. They collapse onto a universal curve.

If the electron thermal pressure gradient is fundamental to the shockwave formation, but T_e does not play a role, then $\nabla n/n$ should be analyzed. Figure 5.7 shows the $\nabla n/n$ x-transect. The left side is in unscaled units and the right side is scaled by σ_0. For a perfectly exponential plasma, this figure would be a step function that is 1 for $x < 0$ and

-1 for $x \geq 0$ when scaled by σ_0. The black lines in the right figure show $\nabla n/n = \pm 1$. These transects deviate from the ideal step function. This is because the density distribution deviates from a perfect exponential.

In unscaled units, $\nabla n/n$ increases as the MOT current increases. Interestingly, in scaled units, $\nabla n/n$ is the same for all three cases.

It would be illuminating to take more data between 60 A and 85 A to see the crossover from M < 1 and M > 1. Also, it would be nice to use larger currents in order to increase $\nabla n/n$, but that would require a new current source.

5.3.2 Varying Atom Expansion Time

The other way the shape was varied was by varying the amount of time the atomic cloud ballistically expands after turning off the magnetic trap before photoionizing. As the cloud expands, the sharp peak at the center rounds out and the density distribution approaches a Gaussian. This allows us to see if the discontinuity at the center causes the shockwave.

Figure 5.8 shows the x-transect grids for 0 ms (blue), 1.5 ms (red), and 2.5 ms (yellow) atom expansion times at 0.05, 1.3, and 2.2 τ_{exp}. There are clear deviations in the initial density distribution. As the atoms expand more before photoionization, the cloud gets wider and the peak is rounded. In the 1.5 ms set, the transects evolve similarly to the 0 ms set with a sharp density jump developing. At 1.3 τ_{exp}, the density gradient for the 1.5 ms set is not quite as steep as the 0 ms set, but they are very similar at 2.2 τ_{exp}. The 2.5 ms set is a different case. It does not form the plateau with sharp jumps in density like other data sets discussed in this thesis. Instead it approaches more of a Gaussian shape, but it does not self-similarly expand when it reaches that shape because its velocity profile is not linear throughout the entire plasma.

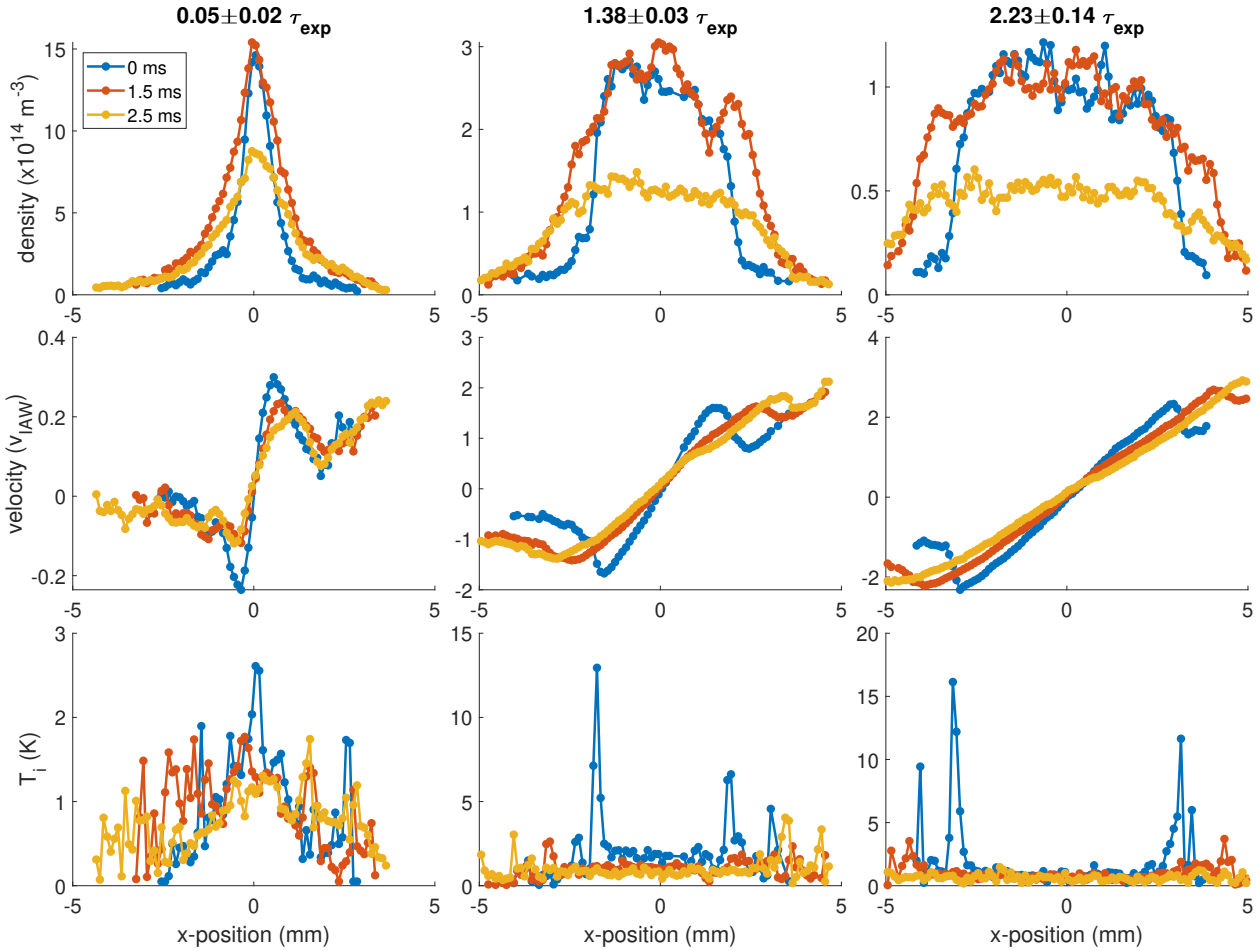

FIGURE 5.8: The density (top), velocity (middle) and ion temperature (bottom) x-transects for different density distributions attained by varying the time the atomic cloud expands after being released from the magnetic trap before photoionization. Atom expansion times shown are of 0 ms (blue), 1.5 ms (red), and 2.5 ms (yellow). The velocity is scaled by $v_{IAW}(t)$. Each column shows the three data sets at similar expansion times scaled by τ_{exp}. Wave steepening is seen in the density transects for the 0 ms and 1.5 ms sets, but not the 2.5 ms set. Wave steepening is also seen in the velocity transect for the 0 ms set, but not the other sets. Large temperature spikes develop in the 0 ms set while small spikes develop in the 1.5 ms set. The 2.5 ms set does not develop temperature spikes. This suggests that the density distribution is essential in shockwave formation.

The velocity transects also show significant deviations. Initially the velocity profiles are fairly similar, with the 0 ms data being slightly steeper and reaching larger extrema. At the later times, the 0 ms data has a significantly larger slope in the central linear section and shows signs of wave steepening. The other two sets do not develop a kink in the

velocity transect. This suggests that these data sets do not develop shock waves.

The ion temperature transects further suggest that the 1.5 ms and 2.5 ms data sets do not develop shockwaves. The 0 ms data develops large temperature spikes. The 1.5 ms set has a very small temperature spike of about 3 K, which is not a striking feature compared to the nearly 15 K seen in the 0 m set. This significantly smaller ion temperature spike could simply be due to the higher density, larger velocity ions expanding into the lower density, slower ions, creating a small amount compressive heating. The 2.5 ms set does not develop a temperature spike. Because the 1.5 ms and 2.5 ms data sets lack the signatures of shockwave formation in the x-transects, neither of these data sets are expected to have Mach numbers close to 1.

Figure 5.9 shows the Mach number evolution for all of the different times the atoms expanded before ionization. These times include 0 ms, 0.5 ms, 1.0 ms, 1.5 ms, 2.0 ms, and 2.5 ms. For the 0 ms time, the Mach number exceeds 1 and remains above 1 for several μs. The 0.5 ms set passes Mach 1 at the last time point before the front expanded beyond the field of range of the camera. None of the longer expansion times approach Mach 1. This shows that the density distribution plays a significant role in shock formation.

Lastly, Fig. 5.10 shows the initial $\nabla n/n$ x-transects in unscaled unites (left) and scaled by σ_0 (right) for 0 ms, 1.5 ms, and 2.5 atom expansion times. Like in Fig. 5.7, in scaled units, $\nabla n/n$ collapses onto a universal curve, showing that $\nabla n/n$ and σ_0 are significant scaling parameters. In unscaled units, $\nabla n/n$ is about a factor of 3 greater for the 0 ms atom expansion data compared to 1.5 ms and 2.5 ms expansion times.

In the observation of shockwaves, the possibility of a Coulomb explosion was discussed in Sec. 3.3.3 and App. C. Further investigation is needed, but it is possible that the sharp peak causes the electrons to rapidly accelerate away from the center of the plasma, creating a charge imbalance and a very brief Coulomb explosion. A larger charge imbalance would be expected for a steeper density gradient, which would create a stronger

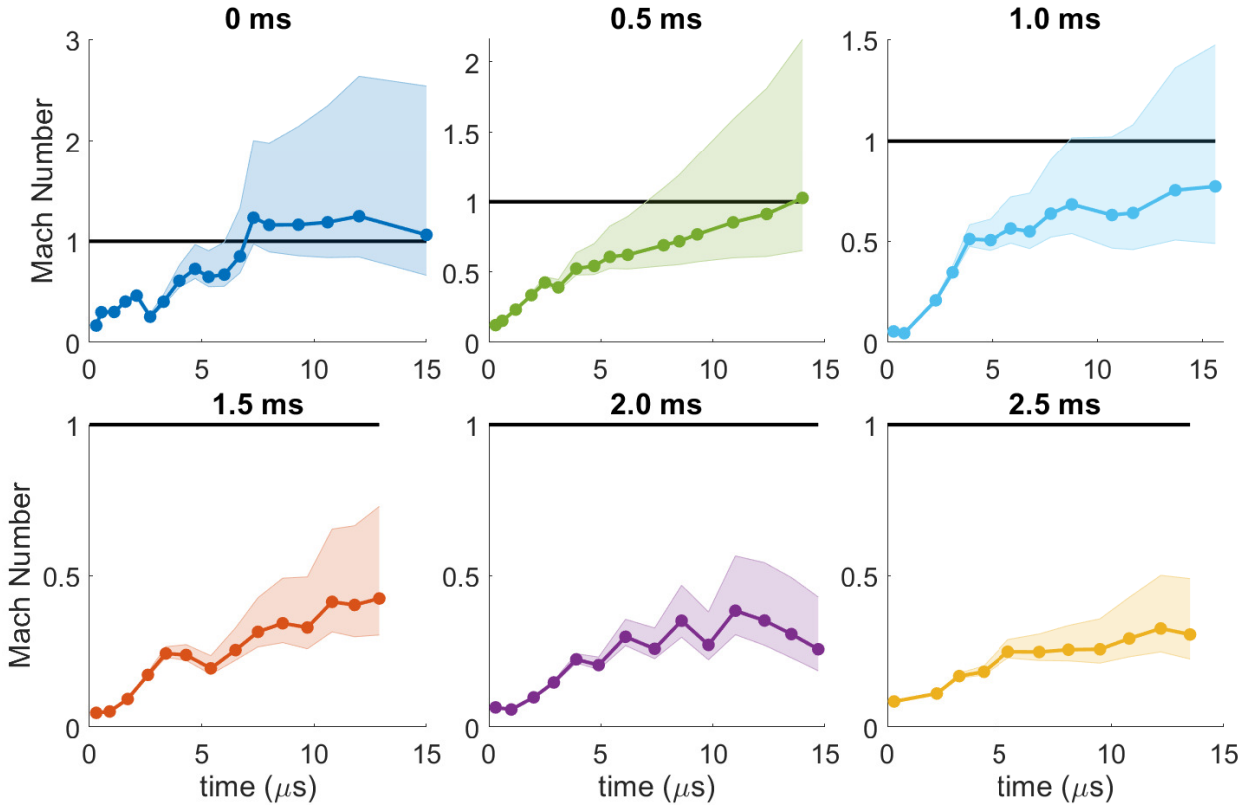

FIGURE 5.9: The Mach number as a function of time for plasmas formed by varying the amount of time the atomic cloud expands before photoionization. Atomic expansion times are given in the titles. Only the 0 ms set exceeds Mach 1 and remains above 1 for several μs. The last point of the 0.5 ms set does achieve Mach 1, but the plasma expands off the camera range, so it is unknown what happens after that. For the longer atomic cloud expansion times, the Mach number remains significantly below 1.

Coulomb explosion. In both methods of varying the density distribution, the gradient at the center was impacted. One possible explanation for why $\nabla n/n$ determines if shockwaves develop is the sharp peak at the center allows for a Coulomb explosion. More work is needed to fully disentangle the influences of the various factors. It would be very nice to be able to diagnose the electrons experimentally. Additionally, an MD simulation for very early times ($\sim$100 ns) would shed light on what the electrons do at the center of the plasma, showing whether or not there is a significant charge imbalance early in the expansion.

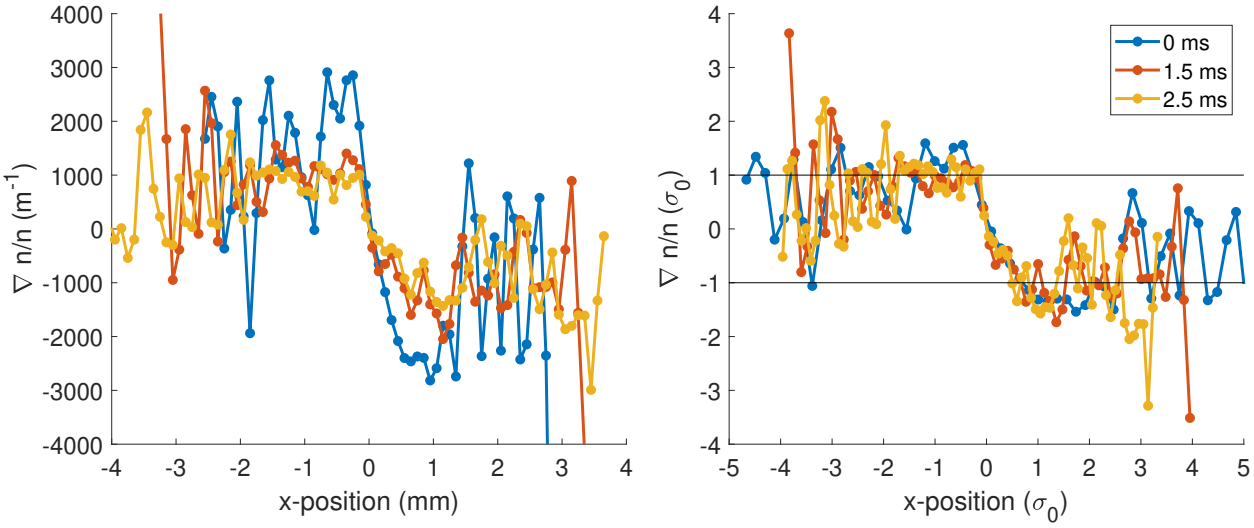

FIGURE 5.10: Initial $\nabla n/n$ x-transect scaled by $1/\sigma_0$ for exponential UNPs formed by varying how long the atomic cloud expands before photoionization. Atomic expansion times shown here are 0 ms (blue), 1.5 ms (red), and 2.5 ms (yellow). For a perfect exponential UNP, this should be a step function at 1 for $x < 0$ and -1 for $x \geq 0$, which is not seen in the data, confirming that the UNPs are not perfectly exponential. Despite the differences in the initial density distribution, they collapse onto a universal curve.

5.4 Conclusions and Future Work

In these experiments, the development of shockwaves was investigated by varying the initial peak density, the electron temperature, and the density distribution.

There was no difference seen for the range of peak densities used, suggesting that the shock formation is not due to the breakdown of hydrodynamics due to kinetics.

Expanding this study to include a much larger density range would be interesting, especially at low densities where the crossover from the kinetic to hydrodynamic regime can be seen. The density range is limited by our experimental apparatus. We used the maximum density that can be loaded into our magnetic trap. Lower densities become challenging to image, especially at later times when the shockwave forms, which is what

we are most interested in. It would be nice to have a larger density range. One fairly simple improvement that could be made is increasing the power and stability of the imaging beam. Increasing the atom number will be more challenging because that will mean breaking vacuum to replace the ion pumps and/or the windows that have water marks as discussed in Sec. 2.3.5.

The electron temperature also did not impact the shockwave formation over the range used in this experiment, indicating that if it is a hydrodynamic effect, it is due to the density distribution.

The density distribution was varied using two methods: varying the current in the coil used to produce the quadrupole magnetic field for the MOT and magnetic trap, and varying how long the atomic cloud expands after being released from the trap before photoionization. Changing the MOT current keeps an exponential density distribution but decreases the density gradient, decreasing the acceleration due the electron thermal pressure gradient. Allowing the atomic cloud to ballistically expand causes the sharp peak at the center to round out, fundamentally changing the shape of the plasma. As the MOT current was lowered, the shockwaves disappeared. Likewise, as the atoms expanded longer before photoionization, the shockwaves disappeared. The density distribution has a significant impact on shock formation, but it is unclear why.

It would be interesting to do a more detailed study varying the MOT current more - filling in more currents between 60 A and 85 A, mapping out the critical current needed to see shockwaves, and investigating what changes in the plasma physics to give rise to the shocks. Additionally, upgrading the current source to a current source that can output much higher current would allow for the study of even more sharply peaked plasmas. Do these plasmas achieve even higher Mach numbers, or is there something in the plasma that limits the shock strength?

Another way to potentially create stronger shocks is by incorporating optical molasses

into the experiment. Traditionally, optical molasses uses a laser beam that is red detuned from resonance so it is Doppler shifted onto resonance with an atom when the atom's velocity opposes the laser beam propagation [58]. In absorbing the photon, the atom gets a momentum kick in the direction opposite its motion, slowing the atom down. Similarly, the laser beam is blue detuned, then the atom gets a momentum kick in the direction of its motion, speeding it up. This can be applied to the ions in a UNP. The laser detuning(s) would be chosen so that the fast ions accelerate and/or the slow ions decelerate. Keeping the lasers on resonance with the targeted ion populations that are accelerating as the plasma expands will present a challenge. Likely, the lasers would only be applied for a brief time after expansion velocities have developed. Power broadening can be used to increase the velocity range that is on resonance, especially because temperature is not of critical importance for this experiment. This would be done with a 408 nm laser on the ${}^2S_{1/2} - {}^2P_{3/2}$ transition so that it does not interfere with imaging. Can you create a stronger shock by manipulating the ion velocities with lasers?

Chapter 6

Conclusion

6.1 Summary

Ultracold neutral plasmas are a powerful plasma simulator, having been used to study many different effects.

UNPs have been used extensively to study plasma expansion with a variety of initial conditions. In this thesis, we studied the expansion of a UNP with an initial exponentially decaying density distribution and compared it to the well-known expansion of a Gaussian UNP. The expansion is predominantly in the hydrodynamic regime and is driven by the electron thermal pressure gradient, like with Gaussian UNPs. σ_0 and τ_{exp} are significant scaling parameters for exponential UNPs too, but with $\tau_{exp} \rightarrow \beta\tau_{exp}$, where β = 1 for Gaussian UNPs and β = 0.63 for exponential UNPs.

Since the beginning of the field, it has been predicted that shockwaves should develop in UNPs, but they had never been experimentally observed. We report the first observation of shockwaves in UNPs, opening a new avenue of research for UNPs. With the right initial conditions, exponential UNPs can show wave steepening and shock formation. The density distribution determines whether shockwaves develop. Varying the peak density and the electron temperature did not impact shock formation for the ranges

used in this study. This suggests that shock formation is likely a hydrodynamic effect and is caused by the electron thermal pressure gradient. Further simulation and modeling work is needed to fully understand the shockwave formation.

The shape of the velocity transect is puzzling. One possible explanation for the shape of the velocity transect is that the sharp cusp at the center of the plasma causes the electrons to rapidly accelerate from the center creating a charge imbalance. This charge imbalance creates a brief Coulomb explosion in the very early time of the plasma evolution. More data and simulations are needed to explore if there is a Coulomb explosion.

6.2 Future Horizons

As always happens with research, when you set out to answer one question, many, many more questions arise. This work has answered a couple of questions, but has opened many doors for future work, both with shockwaves and with UNPs in general. A lot of future directions have already been discussed in previous chapters; most will not be repeated. Here are just a few ideas for additional projects.

6.2.1 Modify Initial Density Distribution

In the experiments in this thesis, we changed the initial density distribution to decrease the density gradient, which caused the shocks to not develop. What would happen if the density gradient was increased? Do the shocks get stronger? There are a few ways this could be done. First is increasing the current in the MOT coils. This will require a new current source.

The other way would be sculpting the density distribution by changing the ionization beam's intensity distribution. Using a filter on the ionization beam that changes the intensity profile so that the beam is significantly more intense at the center than the edges

would allow for more atoms to be ionized at the center of the plasma than the edges, increasing the density gradient. This filter would likely be a custom filter, but Thorlabs makes reverse apodizing ND filters that transform uniform beams into Gaussians.

Blocking half of the ionization beam to ionize only half of plasma could create and even steeper gradient at the cusp. This can be done easily with a knife edge.

6.2.2 Electron Dynamics

The SPRUCE simulation [88] agrees well with our experimental data [73], so we can trust the electron temperature from those simulations. However, it would be nice to be able to measure the electrons experimentally. Adding a Faraday cup [91], wire mesh [35], or another similar device would allow for electron diagnostics and provide deeper insight into the electron dynamics, rather than inferring the electron dynamics from the ion dynamics. This would also allow us to see if there is a charge imbalance in the plasma. If there is a charge imbalance, there will be an early-time electron signal followed by a later electron and ion signal as the plasma expands [91]. Measurements of the electron dynamics would also allow for further confirmation of simulations.

6.2.3 Spectrum Simulation

The spectrum simulation has allowed us to rule out velocity gradient broadening as the sole cause of the large temperature spikes seen at the shock front. However, we have only been able to place bounds on the ion temperature. It would be nice to fit the spectra with the simulation to extract the true temperature. The spectrum simulation is extremely slow, so this is not currently feasible.

6.2.4 Imaging System

It would be informative to study the plasma expansion for longer. This would require changing the magnification on the imaging system so it is no longer a 1:1 optical relay. Due to the current setup and calibration requirements, this is not a simple modification. It would be very nice if the system was designed so that the magnification can easily be changed between $\times 1$, $\times 1/2$, and $\times 2$. This would allow us to study what happens at later times and would give us better resolution at different parts of the plasma. Questions that could be answered include: Do the shocks strengthen or dissipate? What is happening at the center of the plasma? How much do the temperature spikes decrease if a $\times 2$ magnification is used? How much do they increase for a $\times 1/2$ magnification?

Additionally, the experiment studying the magnetic confinement of a UNP [24] that is not discussed in this thesis was limited by the magnification of the imaging system. It would be very interesting to see what the plasma does in the stronger field,

6.2.5 Quasi-neturality Breakdown

Shockwaves have been seen in ultracold plasmas that were photoionized well above the ionization threshold so all of the electrons escape, creating an ion-only plasma that Coulomb explodes [92]. Another interesting experiment would be increasing the electron temperature until quasi-neutrality breaks down, and until a definitive Coulomb explosion is observed. How does the plasma expansion change as there is a larger charge imbalance?

6.2.6 Laser Cooling with Stimulated Emission

UNPs are a promising platform for studying strongly coupled plasma physics. However, DIH limits $\Gamma \lesssim 3$. To probe deeper into the strongly coupled regime, either the atoms

need to be ordered before ionization [54, 56, 57] or heat needs to be removed from the ions after DIH [29]. Using optical molasses [58], laser cooling cooled the ions in the center of the plasma enough to reach $\Gamma = 11$, which was a major breakthrough. However, even larger Γ is desirable to study effects like Coulomb crystallization. The achievable Γ is limited by how long the ions can be cooled, while the ultimate limit on Γ is due to heating caused by electron-ion collisions.

Cooling the ions for longer is desirable and can be achieved by increasing the lifetime of the plasma. This would require increasing the size of the plasma, which would require more efficient loading of atoms into the magnetic trap so there is enough signal to image the ions at a later time. This would require significant, nontrivial upgrades to the vacuum chamber and is not very feasible.

Alternatively, instead of increasing the time the ions are cooled, increasing the laser cooling rate would increase the range of achievable Γ. In a somewhat recent result, stimulated emission was used to accelerate atoms [93]. When an atom scatters thousands of photons through spontaneous emission, the net momentum change of the atom only comes from absorbing photons from the laser beam. However, in this work, the atoms received a momentum kick from absorption and emission as the photon was emitted in the laser beam's direction. The pulses that cause absorption and emission propagate in opposite directions. It would be interesting to apply this work to UNPs, which would double the number of momentum kicks the ions receive and double the cooling efficiency.

6.2.7 Laser Cooling Using an Anti-MOT

An anti-MOT could be used to laser cool the ions [59], building upon the optical molasses results [29]. The linear expansion velocity adds a term in the MOT force equation that can cancel the Zeeman shift. This allows for all of the ions in the UNP to be on resonance with

the cooling beams. Additionally, the magnetic confinement slows the expansion [24] and would allow for more time to cool, further increasing the Γ that can be achieved.

This would also allow the study of strong coupling in a magnetic field, but it is unfortunate that this magnetizes the plasma. The center of the plasma is unmagnetized, but that is a very small region. This could limit the physics that is studied at higher Γ.

In conclusion, the field of UNPs has a bright future with endless possibilities of interesting and exciting work to do for experimental, theoretical, and computational physicists.

Appendix A

System Upgrades

MOT Autorelocker

Figure A.1 shows the circuit diagram for the MOT doubling cavity's locking circuit. The circuit's input is an error signal produced from the MOT cavity 461 nm photodiode signal. Despite the deceptive "output to laser" label, the output does not go to the laser, but goes to the MOT doubling cavity. There is a switch that can send the ramp or the locking signal to the output.

The original MOT lock circuit diagram was drawn by tracing the PCB. The top and bottom sketches of the PCB are included in Figs. A.2 and A.3 respectively. There are several circuits made throughout the lab with this PCB, but the documentation has been lost. These images are included should anyone need to trace another one of these circuits.

Since we had a lot of problems with the MOT lock being extremely sensitive to vibrations and frequently unlocking, we replaced the lock with an autorelocker, removing the need for the MOTsitter and the graduate student needing to manually relock it every time it unlocks. This circuit was built by Priyansh Lunia. This circuit is fast enough to relock the MOT cavity before the SatAbs unlocks, which is essential. Once the SatAbs unlocks, the experiment has to be stopped and any data taken in that scan has to be thrown out.

A nice addition to this would be a slow lock made from an Arduino to adjust the DC

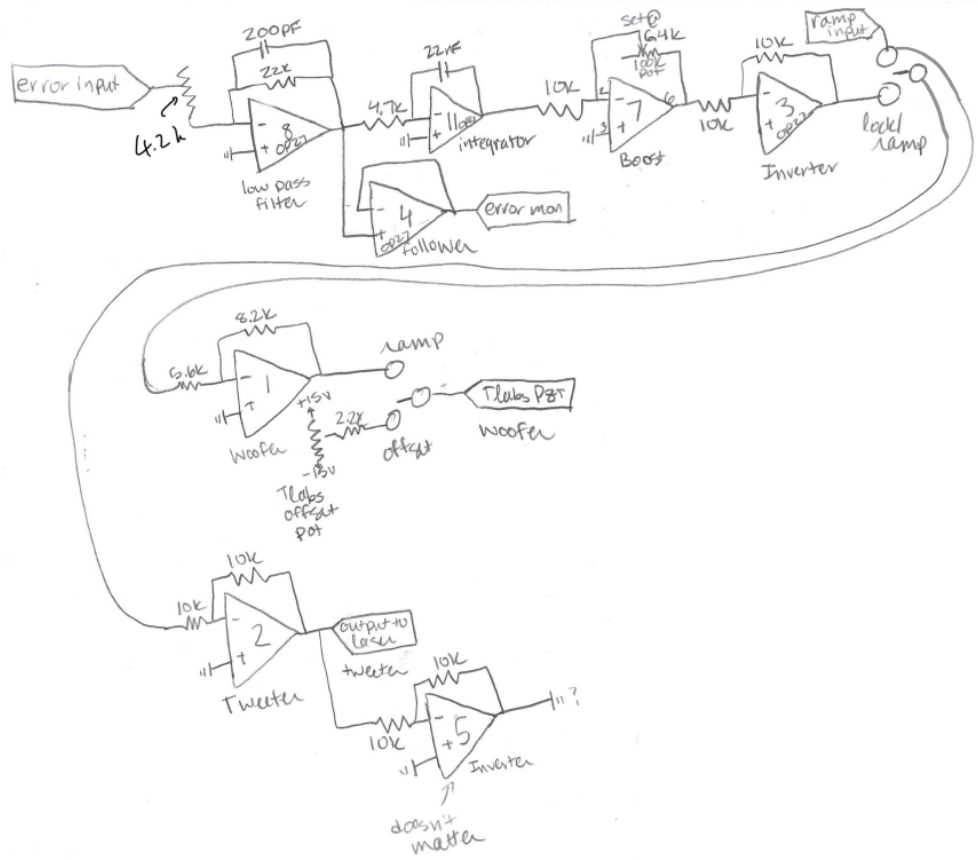

FIGURE A.1: The original MOT doubling cavity locking circuit diagram, acquired by tracing the PCB. This was used to make the autorelocker for the MOT doubling cavity.

offset that drifts over time. However, we can typically go a few hours without having to manually adjust the offset, so it's not the end of the world and we usually catch it before the MOT unlocks. This would really only be necessary if we wanted to take data overnight without having to stay in the lab all night, but there are other bigger problems that prevent that.

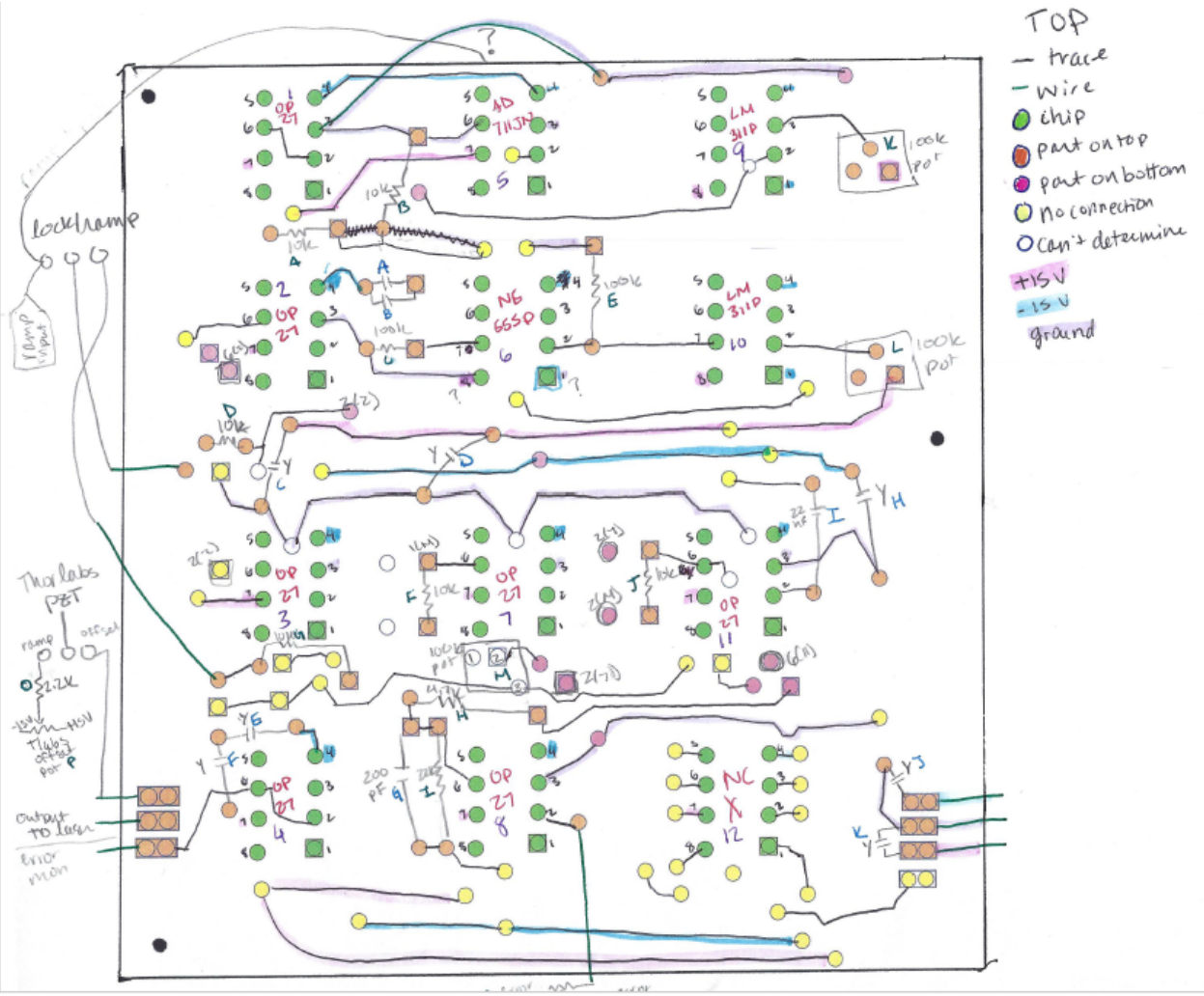

FIGURE A.2: A sketch of the top of the PCB for the original MOT doubling cavity locking circuit. A legend is included on the top right so the color coding is clear. This is especially useful should a future student need to make a circuit using one of the extra PCBs, or should they need to trace another circuit that was made from the same PCB.

A.0.1 New heater coil on atom source

Here I describe the atomic source system in great detail. We replaced the nozzle heater coil an the strontium in January and February 2023. Unfortunately, this meant we had to break vacuum.

Figure **??** is a picture of the atom source. It has two main parts: the flange with the

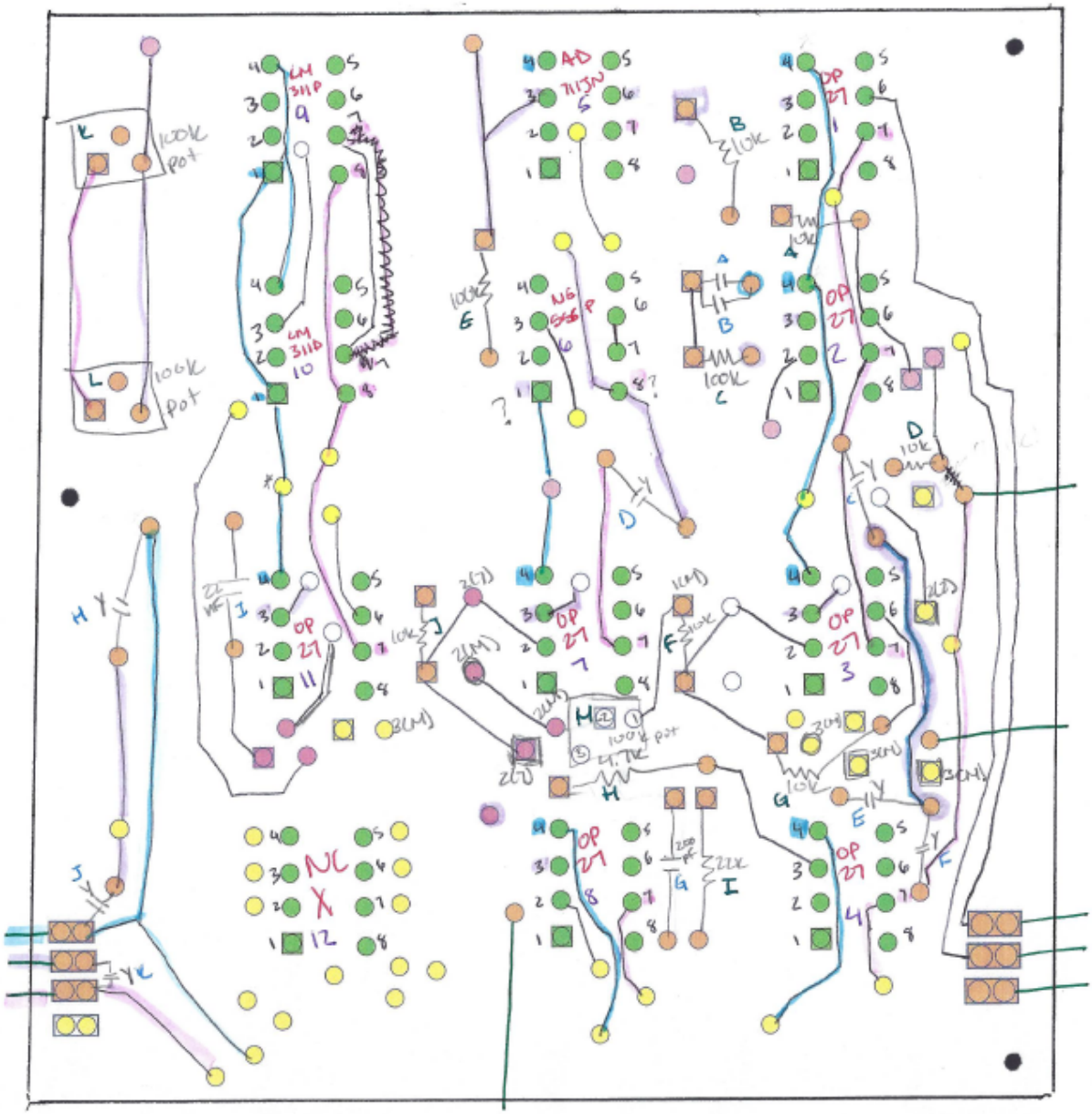

FIGURE A.3: The bottom of the original MOT doubling cavity locking circuit.The legend for the color coding can be found in Fig. A.2.

fire rods and feedthrough (left through center), and the nozzle (right). The flange is what connects the atom source to the vacuum chamber. The fire rods are in the tube that is fixed to the flange. They heat the strontium so it sublimates, creating the free atoms that

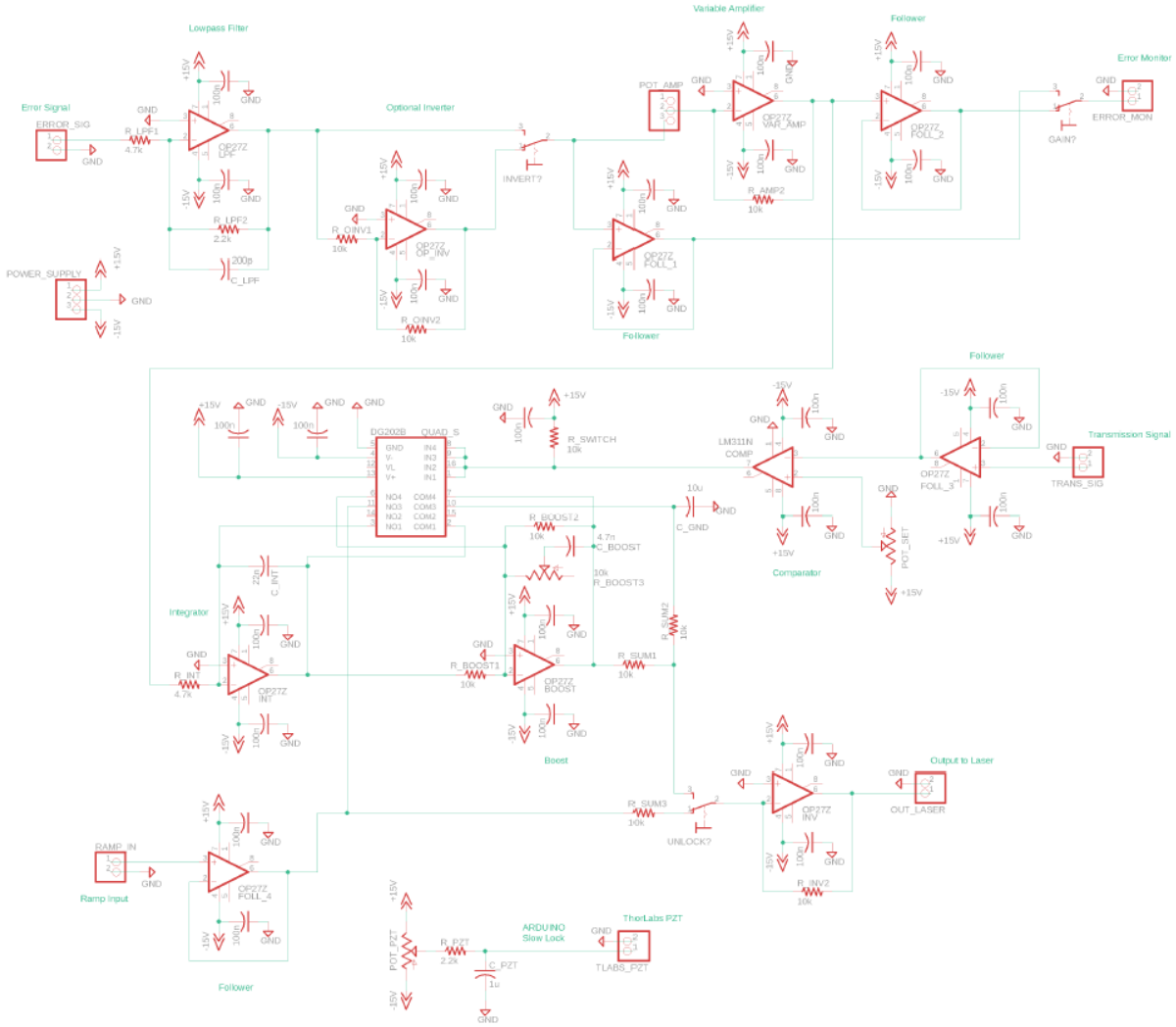

FIGURE A.4: The circuit diagram for the MOT autorelocker, created by Priyansh Lunia.

flow through a small hole in the nozzle.

The nozzle, shown in Fig. A.5, is held to the rest of the strontium source with three screws. The tip of the nozzle is far from the fire rods, creating a thermal gradient that allows the strontium atoms to stick inside the nozzle hole and clog the nozzle. To prevent that, the nozzle is wrapped with UHV compatible heater wire. The wire is held in place with a clamp. When the experiment is not in use, the fire rods are turned off, but the

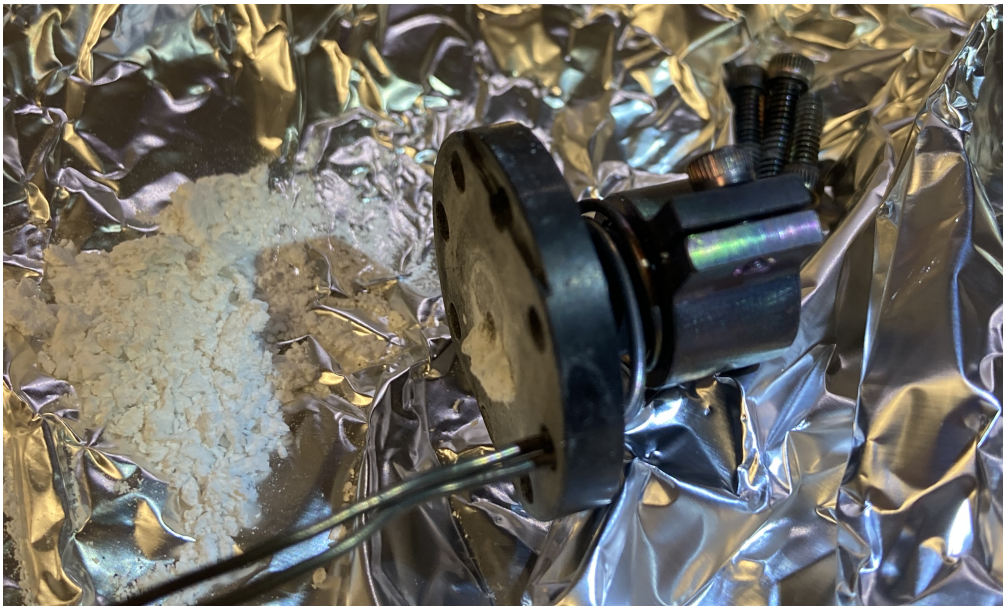

FIGURE A.5: The nozzle removed from the rest of the atom source. The white powder is oxidized strontium.The tip of the nozzle is wrapped in UHV compatible heater wire. The coil is under the clamp that is on the right side.

nozzle heater is always left on to prevent any clogs. After many years of continual use, the heater wire failed and the nozzle clogged, requiring us to fix it.

Figure A.6 shows the strontium source with the nozzle removed and the cavity filled with strontium exposed. Pure strontium is a normal metalic silver color, but it quickly oxidizes when exposed to air and becomes a white powder that can be clearly seen in Fig. A.5.

As shown in Fig. **??**, there are also two wires on the feedthrough that are used to power the heater on the nozzle. Only one of the feedthrough wires is used because the heater wire is a coaxial wire, so the core is connected to the feedthrough, and then the core is shorted to the jacket using a barrel connector on the other end. The jacket is in contact with the nozzle and so completes the circuit through the chamber, which is grounded.

Figure A.7 shows the nozzle without the clamp. The tip of the nozzle is wrapped in heater wire. There are four layers. The bottom layer has seven wraps, the second layer

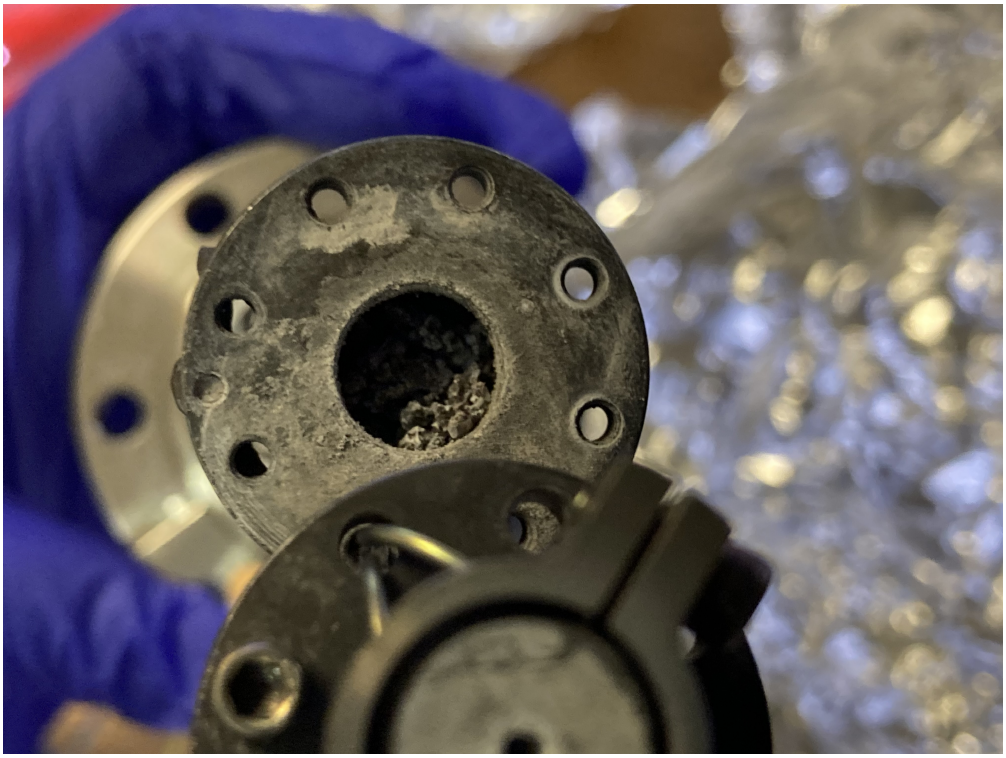

FIGURE A.6: The strontium source viewed from the nozzle with the nozzle removed and the strontium exposed. Part of the nozzle is shown at the bottom of the picture. This angle shows the hole in the nozzle that the atoms come through.

has six wraps, the third layer has six wraps, and the top layer has seven wraps. The seventh wrap on the top and bottom layers are fairly loose and are to help get the wire in the right position to actually wrap the nozzle. Each layer is very tightly wrapped so that neighboring loops on the same layer are touching. Figure A.8 shows the nozzle with just one layer of the coil. This better shows how tightly wrapped the coil is.

The ends of the wire are fed through the same hole. This is important because it allows you to put the nozzle on the source before loading it with strontium, and then just rotating it into place and quickly adding the screws. This cuts down on the time it takes to seal the nozzle compared to feeding the wire through two holes after loading the strontium. This is important because the longer the strontium is exposed to air the more it oxidizes.

FIGURE A.7: The nozzle with the clamp removed, showing how the top layer of heater wire was wrapped. Both ends of the wire were fed through the same hole.

Figure A.9 shows the heater wire that we used. This is just included for documentation purposes.

Nozzle Voltage (V)	Nozzle current (A)	Temperature at the source (C)
28.3	0.52	224
26.0	0.45	208
25.5	0.44	204

TABLE A.1: Different voltages and currents applied to the nozzle and the resulting temperature read by the fire rod controller with the fire rods off. The voltage and current were measured by the power supply.

Figure A.10 shows the ends of the heater wire that was removed from the nozzle. The end at the top with a black section is the end that was connected to the feedthrough. The

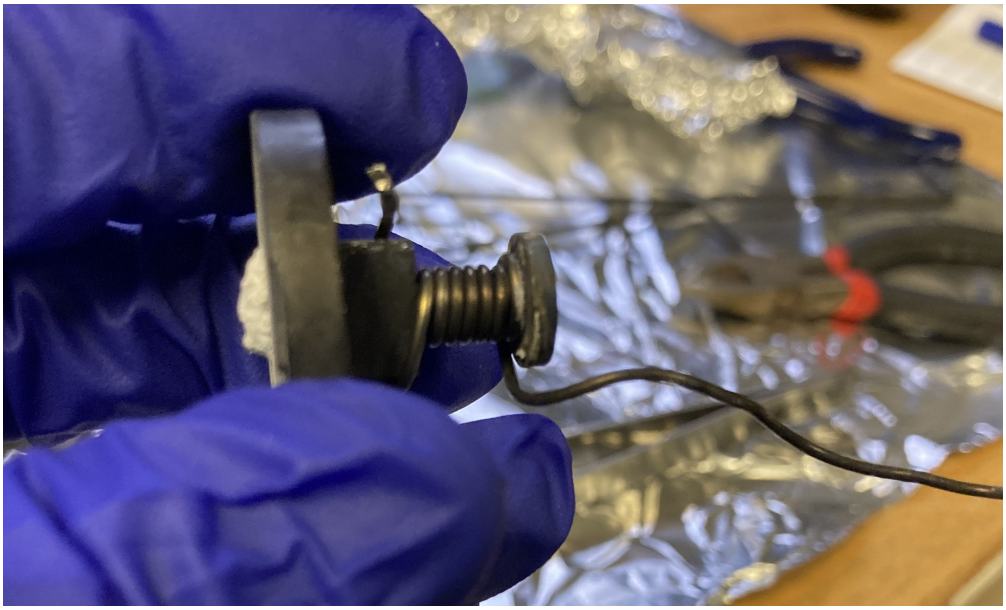

FIGURE A.8: The nozzle with only the bottom layer of the heater wire. The coil is wrapped very tightly so there is no space for each wrap to move laterally.

black section is the crimp. Soldier cannot be used because it is not UHV compatible. The other end on the bottom shows the small amount of the core that was exposed. This is folded back onto the outer jacket and held in place with a barrel connector.

The crimp was the failure mechanism, so we needed to come up with a better solution. In the end, we just used a barrel connector and a different crimp, as shown in Fig. A.11. It is not very stable as a small amount of stress will undoubtedly cause the core to snap, but it gets the job done for now.

While the barrel connector and crimp is efficient and works, it is not a robust long-term solution. I designed a custom plate that uses alumina (a UHV compatible electrical insulator that can withstand the heat from the fire rods) to hold it in place. It was significantly more expensive than the barrel connector, it had a pretty substantial lead time, and it was extremely difficult to find a supplier who could make an alumina plate that was thin enough to fit between the feedthrough wire and the atom source tube. This device is

FIGURE A.9: The heater wire that we use to warm the nozzle on the strontium atom source.

described in Appendix A.1.

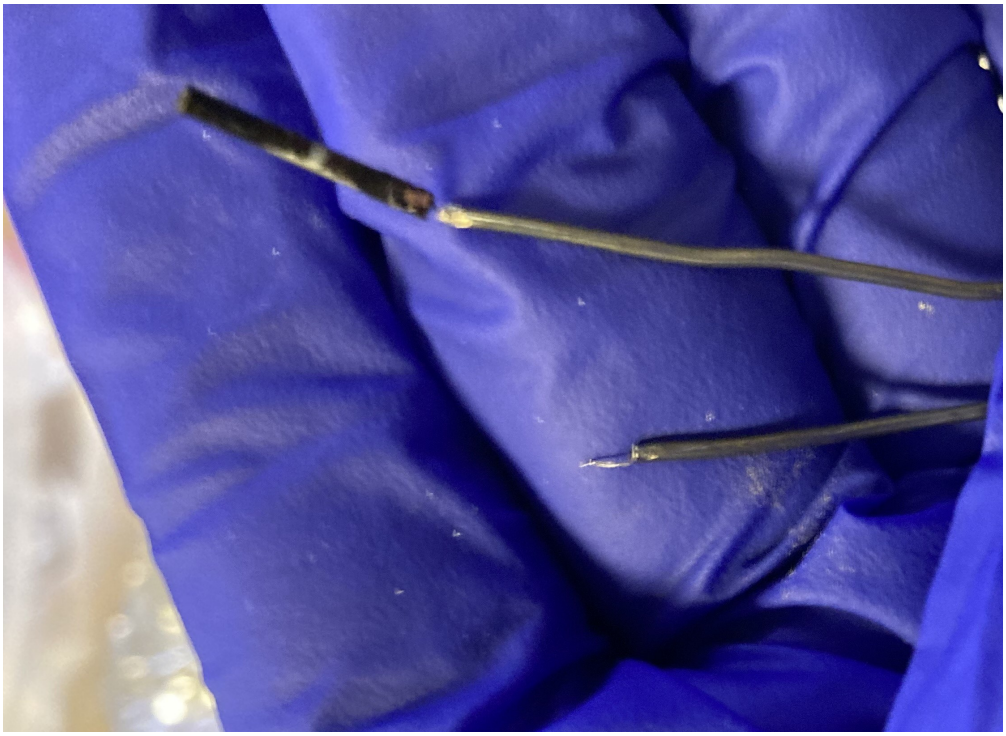

FIGURE A.10: The ends of the heater wire that was removed from the nozzle. The top end was crimped to the feedthrough using the black crimp shown. The end in the bottom of the picture shows a small amount of the core that was stripped. It was shorted to the jacket with a UHV compatible barrel connector.

A.1 Robust UHV Compatible Connector for Atomic Source Nozzle Heater

As described above, we needed to design a device to connect the core of the heater wire to the feedthrough. It needs to be robust, strain relieving to protect the delicate core of the heater wire, UHV compatible, and able to withstand temperatures of 500 C. It also needs to be electrically insulating to prevent shorting to the vacuum chamber.

This device is shown in Figs. A.12-A.16. It uses alumina and stainless steel. The feedthrough and core are connected electrically through a stainless steel plate. The wires and stainless steel are sandwiched by alumina plates, a ceramic that is compatible with

FIGURE A.11: The new connection between the feedthrough and the core of the heater wire. A male electrical contact is crimped to the heater wire core. The barrel connector is fixed to the feedthrough and the contact.

UHV and can withstand high temperatures. The layers are held together with alumina screws. The bottom (light pink) is an alumina plate and the base for the rest of the device. The holes on this plate are tapped. On the second layer is a stainless plate (green) that is about 2/3 the length of the base plate. It is short enough that it will not touch the outer jacket of the heater wire, which would create a short. It's height is the radius of the heater wire so that the core does not need to bend to make contact with the plate, minimizing the strain on the core. The third layer is the different wires. The feedthrough (black) is on the left. The core (very small red, not visible in every view) is in the center. The full heater wire (blue) is on the right. The top layer is made of three separate alumina plates with through holes. Using three pieces instead of one allows the appropriate pressure to be applied to each wire, all of which have different diameters, ensuring a good electrical

connection is made.

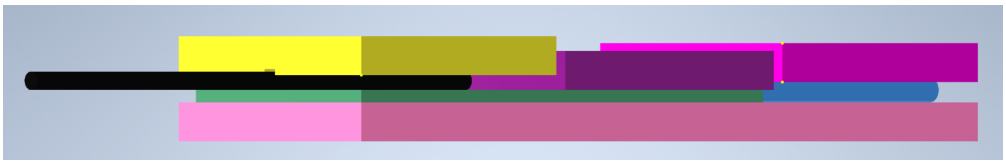

FIGURE A.12: The angled side view of the alumina connector showing the three different pieces that clamp the feedthrough (left, yellow), the heater wire core (middle, purple), and the heater wire (right, pink). The feedthrough is the black rod (left), the core of the heater wire is the tiny red line that is hidden in most views (middle), and the heater wire with the jacket is the blue rod (right). The green slab is a stainless steel plate that makes the electrical connection between the feedthrough and the heater wire core.

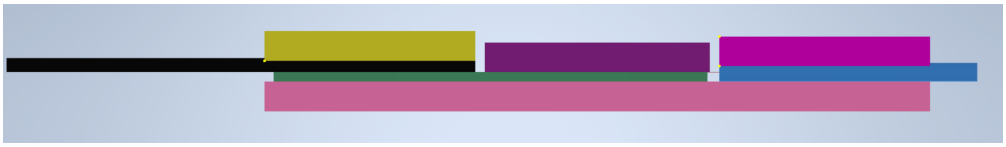

FIGURE A.13: Straight-on side view of the alumina connector design.

As can be seen in the top view in Fig. A.14, the holes on the right side of the middle piece are shifted to be as close to the edge as the manufacturer will allow. This is so pressure is immediately applied to the core in case the core is very short. Ideally, the core will extend at least half way through the middle alumina plate, so having the screws that close to the edge is likely unnecessary, but in case the core breaks, it is a good backup over having to re-wrap the nozzle.

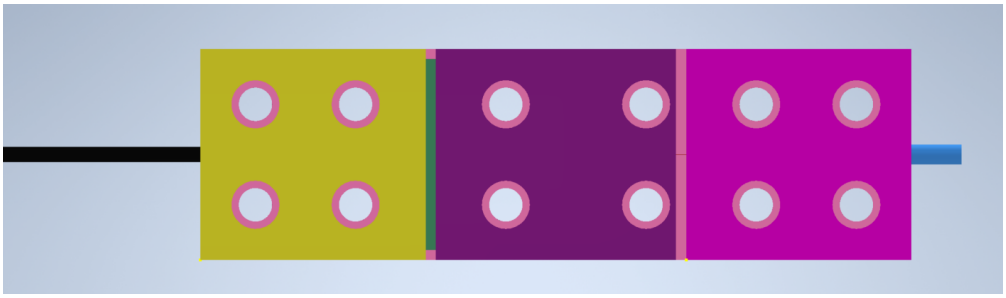

FIGURE A.14: Top view of the alumina connector design.

Figures A.15 and A.16 show the short sides of the device. There is a rectangular channel on both. The wires rest in the channel. They are narrower than the diameter of the wire so there are two points of contact. Ideally it would be exactly the diameter of the wire so there are 3 points of contact, but we cannot count on that level of precision. If it is too wide, there will only be 1 point of contact. We want at least 2 for stability.

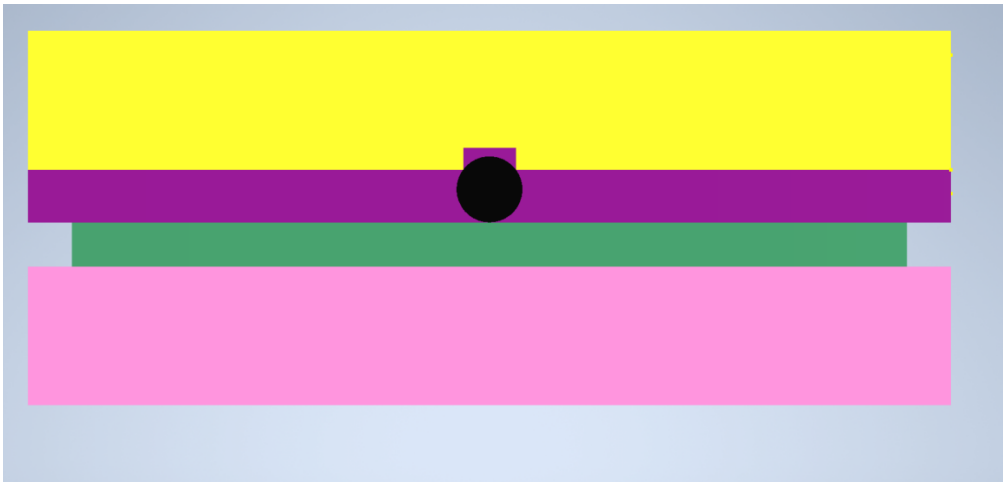

FIGURE A.15: View of the alumina connector from the feedthrough side.

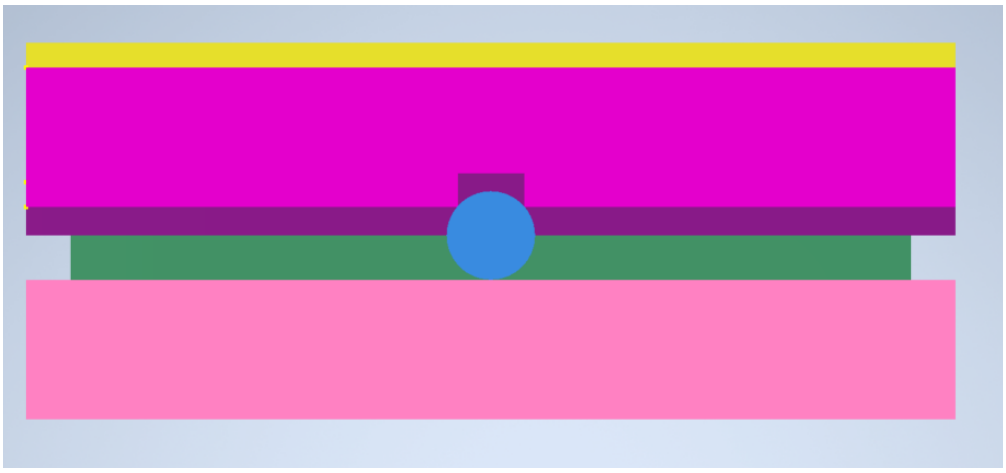

FIGURE A.16: View of the lumina connector from the heater wire side.

Appendix B

Temperature and Humidity Logger Detailed Write Up and Code

B.1 How to Build the Temperature and Humidity Logger

Supplies

- Arduino Mega 2560
- Sparkfun Protoboard shield
- 2 DHT22 sensors
- OSEPP real time clock & microSD breakout
- 16x2 LCD with 10 kΩ potentiometer
- Power adaptor for Arduino so you don't have to power the Arduino from the computer

Building the Circuit

First assemble the protoshield as described in the link above. The DHT22 sensors were soldered to long wires that were twisted together. Below is a picture of how to wire the DHT22s (found on Google). They are connected to D7 and D8 on the protoshield rather than pin 2. The 10k resistor was soldered to the protoboard. The sensor connected to D7 is DHT1 on the LCD. The sensor connected to D8 is DHT2 on the LCD. The two sensors have D7 or D8 written on the back in sharpie.

Next wire the RTC and microSD breakout. The RTCSD-01 has to be connected to different pins of the Mega than the Uno.

- SCL to Mega communication 21
- SDA to Mega communication 20
- VCC to +5 V
- GND to GND
- SCLK to Mega D52
- MISO to Mega D50
- MOSI to Mega D51
- SDSC to Mega D4

Finally, wire the 16x2 LCD as described below. Here's a tutorial.

- LCD RS (pin 4) pin to Mega D44
- LCD D4 (pin 11) to Mega D5
- LCD D5 (pin 12) to Mega D45

- LCD D6 (pin 13) to Mega D3
- LCD D7 (pin 14) to Mega D2
- LCD E (pin 6) to Mega D46
- LCD VSS (pin 1) to ground
- LCD VDD (pin 2) to +5 V
- LCD V0 (pin 3) to sweep on 10k pot
- LCD RW (pin 5) to LCD VSS (pin 1)
- LCD A (pin 15) to 220 ohm resistor to +5 V
- LCD 16 to GND

The Arduino Code

The code for the Arduino can be found on the drobo in the Plasma folder under projects and then humidity data. It is also included in the Appendix B.2.

MATLAB Code

I wrote a Matlab program to plot the temperature and humidity data for a specified time period. The code can be found on the drobo in the Plasma folder under projects and then humidity data. It is also included in Appendix B.3

B.2 Arduino Code

Below is the Arduino code for the humidity and temperature logger described above.

```
/*
  SD card date, time, temp, and humidity datalogger
  This code logs data from 2 DHT22 temperature and humidity sensors
  as well as date and time from a DS1307 clock to an SD card.
  It uses the Adafruit DHT sensor library
  https://github.com/adafruit/DHT-sensor-library
  and the Adafruit RTC library https://github.com/adafruit/RTClib

  For details on the circuit, see the write up on the Drobo.

 MacKenzie Warrens
 9 March 2019
*/

// including the libraries for the SD shield, DHT sensor, and LCD.
#include <SD.h>
#include "DHT.h"
#include <LiquidCrystal.h>
// Date and time functions using a DS1307 RTC connected via I2C and Wire lib
#include <Wire.h>
#include "RTClib.h"
#include <SPI.h>

#define DHTPIN1 7         // what pin the 1st sensor is connected
#define DHTPIN2 8         // sensor 2
#define DHTTYPE DHT22    // Which type of DHT sensor you're using:

DHT dht1(DHTPIN1, DHTTYPE);
DHT dht2(DHTPIN2, DHTTYPE);
```

```
31 // initialize the library by associating any needed LCD interface pin
   // with the arduino pin number it is connected to
33 const int rs = 44, en = 46, d4 = 5, d5 = 45, d6 = 3, d7 = 2;
   LiquidCrystal lcd(rs, en, d4, d5, d6, d7);
35
   // On the Ethernet Shield, CS is pin 4. Note that even if it's not used as the
       CS pin,
37 // the hardware CS pin (10 on most Arduino boards, 53 on the Mega) must be
      left as an output or the SD library functions will not work.
   RTC_DS1307 rtc;
39 const int chipSelect = 4;

41 //set delay time (time between readings) in minutes (converts to ms later)
   const long delayTime = 10;
43


45 void setup() {
     //set up RTC stuff
47   Wire.begin();
     rtc.begin();
49
     // set up the LCD's number of columns and rows:
51   lcd.begin(16, 2);
     // Print a message to the LCD.
53   lcd.print("Initialized");

55   //initialize temp and humidity sensors
     dht1.begin();
57   dht2.begin();

59   if (! rtc.begin()) {
```

```
    lcd.setCursor(0,1); //setting the cursor to the beginning of the 2nd row.
61    lcd.print("Couldn't find RTC");
    while (1);
63  }

65  if (! rtc.isrunning()) {
    // following line sets the RTC to the date & time this sketch was compiled
67    // rtc.adjust(DateTime(F(__DATE__), F(__TIME__)));
    lcd.setCursor(0,1); //setting the cursor to the beginning of the 2nd row.
69    lcd.print("RTC fail");
  }
71
  lcd.setCursor(0,1);
73  lcd.print("Initializing SD");
  // make sure that the default chip select pin is set to output, even if you
    don't use it:
75  pinMode(10, OUTPUT);

77  // see if the card is present and can be initialized:
  if (!SD.begin(chipSelect)) {
79    lcd.setCursor(0,1); //setting the cursor to the beginning of the 2nd row.
    // don't do anything more:
81    lcd.print("Card failed");
  }
83  else {
    lcd.setCursor(0,1); //setting the cursor to the beginning of the 2nd row.
85    lcd.print("SD good :)");
  }
87}

89//main loop of the program - runs infinitely
```

```
void loop()
{
  //getting current date and time
  DateTime now = rtc.now();

  //getting humidity and temperature data
  float humidity1 = dht1.readHumidity();
  //float tempC1 = dht1.readTemperature(); //temperature in Celcius
  float tempF1 = dht1.readTemperature(true); //temperature in F
  float humidity2 = dht2.readHumidity();
  //float tempC2 = dht2.readTemperature();
  float tempF2 = dht2.readTemperature(true);

  //testing to see if read humidity sensors correctly. if outputs = nan, reset
    to 0 so can still plot
  if (isnan(humidity1)){
    lcd.setCursor(0,0); //setting the cursor to the beginning of the 2nd row.
    lcd.print("DHT1 humid fail");
    humidity1 = 0;
  }
  if (isnan(tempF1)){
    lcd.setCursor(0,0); //setting the cursor to the beginning of the 2nd row.
    lcd.print("DHT1 temp fail");
    tempF1 = 0;
  }
  if (isnan(humidity2)){
    lcd.setCursor(0,1); //setting the cursor to the beginning of the 2nd row.
    lcd.print("DHT2 humid fail");
    humidity2 = 0;
  }
  if (isnan(tempF2)){
```

```
    lcd.setCursor(0,1); //setting the cursor to the beginning of the 2nd row.
121   lcd.print("DHT2 temp fail");
    tempF2 = 0;
123 }

125 // open the file:
  File dataFile = SD.open("DATALOG.csv", FILE_WRITE);
127
  // if the file is available, write to it:
129 if (dataFile) {
    //first record the date and time
131   dataFile.print(now.month(), DEC); dataFile.print(','); // column 1 =
   month (NOT 2 digit format)
    dataFile.print(now.day(), DEC); dataFile.print(',');    // column 2 = day
   (NOT 2 digit format)
133   dataFile.print(now.year(), DEC); dataFile.print(',');   // column 3 = year
    dataFile.print(now.hour(), DEC); dataFile.print(',');   // column 4 = hour
135   dataFile.print(now.minute(), DEC); dataFile.print(','); // column 5 =
   minute

137   //now record the humidity and temperature data
    dataFile.print(humidity1); dataFile.print(',');   // column 6 = humidity
   (%) of 1st sensor
139   dataFile.print(tempF1); dataFile.print(',');      // column 7 = temp (F)
   of 1st sensor
    dataFile.print(humidity2); dataFile.print(',');   // column 8 = humidity
   (%) of 2nd sensor
141   dataFile.print(tempF2);                           // column 9 = temp (F)
   of 2nd sensor
    dataFile.println();//moving to the next line
143
```

```
    dataFile.close();
  }
  else{
    lcd.setCursor(0,0);
    lcd.print("SD error");
  }

  // printing the  temp and humidity to the LCD
  lcd.setCursor(0,0); //setting the cursor to the beginning of the 2nd row.
  lcd.print("DHT1:"); lcd.print(humidity1); lcd.print(" "); lcd.print(tempF1);
  lcd.setCursor(0,1);
  lcd.print("DHT2:"); lcd.print(humidity2); lcd.print(" "); lcd.print(tempF2);

  //wait dealyTime number of minutes until take next point
  delay(delayTime*60*1000);
}
```

B.3 Plotting Program

I wrote a Matlab program to plot the humidity and temperature for a given .csv datafile and time frame. You give it the file path and the beginning and end date/time that you want to plot. It filters out the dates you don't care about and plots the humidity and temperature for both sensors. Here are sample plots below for this data and beginning time of [3 31 2019 13 30] and end time of [4 1 2019 14 30]. This data was test data and was taken every two minutes. I have since changed the sample frequency to once every 10 minutes. The file will be much smaller and there won't be as good of time resolution.

```
%% plotHumidityAndTemp
```

```
% This program plots the humidity and temperature for a given
% date and time range. The user inputs the data file, beginning
% date/time and end date/time. The program filters the data and
% plots the timeframe of interest.

%NOTE: This can take a long time depending on how big the data
   file is

clear all

%% Inputs
filename = ''; %insert the file name here (include whole path)
dateBegin = [3 31 2019 13 30]; %[DD MM YYYY HH MM] HH must be in
   24 hr format!!
dateEnd = [4 1 2019 14 30]; %[DD MM YYYY HH MM] HH must be in 24
   hr format!!

%% Filtering Data
data = xlsread(filename); %loading data column 1 is month, column
    2 is day,
%col 3 is year, col 4 is hour, col 5 is minute, col 6 &8 are
   humidity, and col 7&9 are temperature

%filtering dates
```

```
dummy = 0; %used to elimiate indexing error. There's probably a
   more elegant way of doing this, but it works.
for i = length(data(:,1)):-1:1
    %filtering year
    if dateBegin(3) == dateEnd(3)
        if data(i,3) < dateBegin(3)
            data(i,:) = [];
            dummy = 1;
        elseif data(i,3) == dateBegin(3)
            %filtering month
            if data(i,1) < dateBegin(1)
                data(i,:) = [];
                dummy = 1;
            elseif data(i,1) == dateBegin(1)
                %filtering day
                if data(i,2) < dateBegin(2)
                    data(i,:) = [];
                    dummy = 1;
                elseif data(i,2) == dateBegin(2)
                    %filtering hour
                    if data(i,4) < dateBegin(4)
                        data(i,:) = [];
                        dummy = 1;
                    elseif data(i,4) == dateBegin(4)
                        %filtering minute
```

```
45                      if data(i,5) < dateBegin(5)
                            data(i,:) = [];
47                          dummy = 1;
                        end
49                  end
                end
51          end
        end
53      %getting rid of data past end of time frame
        if dummy == 0 %if dummy = 1, then it doesn't try to
    evaluate
55          if data(i,3) > dateEnd(3)
                date(i,:) = [];
57              dummy = 1;
            elseif data(i,3) == dateEnd(3)
59                  if data(i,1) > dateEnd(1)
                        date(i,:) = [];
61                      dummy = 1;
                    elseif data(i,1) == dateEnd(1)
63                          if data(i,2) > dateEnd(2)
                                data(i,:) = [];
65                              dummy = 1;
                            elseif data(i,2) == dateEnd(2)
67                              if data(i,4) > dateEnd(4)
                                    data(i,:) = [];
```

```
69                                  dummy =1;
                                elseif data(i,4) == dateEnd(4)
71                                  if data(i,5) > dateEnd(5)
                                        data(i,:) = [];
73                                      dummy = 1;
                                    end
75                              end
                            end
77                      end
                    end
79              end
                dummy = 0;
81          else
                if data(i,3) <= dateBegin(3)
83                  if data(i,3) < dateBegin(3)
                        data(i,:) = [];
85                      dummy = 1;
                    elseif data(i,3) == dateBegin(3)
87                      %filtering month
                        if data(i,1) < dateBegin(1)
89                          data(i,:) = [];
                            dummy = 1;
91                      elseif data(i,1) == dateBegin(1)
                            %filtering day
93                          if data(i,2) < dateBegin(2)
```

```
                        data(i,:) = [];
95                      dummy = 1;
                    elseif data(i,2) == dateBegin(2)
97                      %filtering hour
                        if data(i,4) < dateBegin(4)
99                          data(i,:) = [];
                            dummy = 1;
101                     elseif data(i,4) == dateBegin(4)
                            %filtering minute
103                         if data(i,5) < dateBegin(5)
                                data(i,:) = [];
105                             dummy = 1;
                            end
107                     end
                    end
109             end
            end
111     end
        %getting rid of data past end of time frame
113     if dummy == 0 %if dummy = 1, then it doesn't try to
    evaluate
            if data(i,3) > dateEnd(3)
115             date(i,:) = [];
                dummy = 1;
117         elseif data(i,3) == dateEnd(3)
```

```
                    if data(i,1) > dateEnd(1)
119                     date(i,:) = [];
                        dummy = 1;
121                 elseif data(i,1) == dateEnd(1)
                            if data(i,2) > dateEnd(2)
123                             data(i,:) = [];
                                dummy = 1;
125                         elseif data(i,2) == dateEnd(2)
                                if data(i,4) > dateEnd(4)
127                                 data(i,:) = [];
                                    dummy =1;
129                             elseif data(i,4) == dateEnd(4)
                                    if data(i,5) > dateEnd(5)
131                                     data(i,:) = [];
                                        dummy = 1;
133                                 end
                                end
135                         end
                    end
137             end
        end
139     end
end
141
%converting the time in data to datetime format for plotting
```

```
time = [];
for index = 1:length(data(:,1))
    time = [time; datetime(data(index,3),data(index,1),data(index
   ,2),data(index,4),data(index,5),0)];
end

%plotting humidity
figure(1); clf;
plot(time,data(:,6),'b.-')
hold on
plot(time,data(:,8),'r.-')
legend('DHT 1', 'DHT2')
xlabel('Time')
ylabel('Humidity (%)')
title('Humidity')

%plotting temperature
figure(2); clf;
plot(time,data(:,7),'b.-')
hold on
plot(time,data(:,9),'r.-')
legend('DHT 1', 'DHT2')
xlabel('Time')
ylabel('Temperature (F)')
title('Temperature')
```

Appendix C

Coulomb Explosion Derivation

In the regime where the excess charge build up becomes the dominant term, Eq. 3.22 becomes

$$\dot{\vec{v}}_i = \frac{e}{m_i}\vec{E}. \tag{C.1}$$

Assuming a spherically symmetric exponentially decaying single species plasma with charge density $\rho(r) = en_0e^{-r/\sigma_0}$, we can calculate the electric field using Gauss's law in integral form $\int \vec{E} \cdot d\vec{A} = \frac{q_{enc}}{\epsilon_0}$, where q_{enc} is the charge enclosed by the surface and ϵ_0 is the vacuum permittivity. Taking advantage of spherical symmetry, $\int \vec{E} \cdot d\vec{A} = 4\pi r^2 E(r)$, which allows us to solve for the electric field simply by integrating the charge density over all space.

$$q_{enc} = \int \rho dV \tag{C.2}$$

$$= en_0 \int e^{-r/\sigma} r^2 sin(\theta) dr d\theta d\phi \tag{C.3}$$

$$= 4\pi en_0 \int_0^{r'} r^2 e^{-r/\sigma} dr \tag{C.4}$$

Let $a = 1/\sigma$. Then

$$q_{enc} = 4\pi e n_0 \int_0^{r'} r^2 e^{-ar} dr \tag{C.5}$$

This integral becomes much easier if we use the trick below where we take the derivative of the exponential term in the integrand until we obtain something that looks like the integrand. Taking the first derivative with respect to a gives

$$\frac{d}{da} e^{-ar} = -re^{-ar}. \tag{C.6}$$

Taking a second derivative with respect to a gives

$$\frac{d^2}{da^2} d^{-ar} = r^2 e^{-ar}. \tag{C.7}$$

This greatly simplifies the math, and thus q_{enc} becomes

$$q_{enc} = 4\pi e n_0 \frac{d^2}{da^2} \int_0^{r'} e^{-r/\sigma} dr \tag{C.8}$$

$$= 4\pi e n_0 \left[\frac{2}{a^3}(1 - e^{-ar}) - \frac{2r}{a^2} e^{-ar} - \frac{r^2}{a} e^{-ar} \right]. \tag{C.9}$$

Substituting $a = 1/\sigma$ back in gives

$$q_{enc} = 4\pi e n_0 \sigma \left[2\sigma^2 (1 - e^{-r/\sigma}) - 2r\sigma e^{-r/sigma} - r^2 e^{-r/\sigma} \right]. \tag{C.10}$$

The electric field produced by this charge configuration is given by

$$E(r) = \frac{e n_0 \sigma}{\epsilon_0} \left[\frac{2\sigma^2}{r^2}(1 - e^{r/\sigma}) - \frac{2\sigma}{r} e^{-r/\sigma} - e^{-r/\sigma} \right] \tag{C.11}$$

Finally, we solve for the acceleration given in Eq. 3.23 using Eq. 3.24.

$$\dot{v}_i = \frac{e^2 n_0 \sigma}{m\epsilon_0}\left[\frac{2\sigma^2}{r^2}(1 - e^{-r/\sigma}) - \frac{2\sigma}{r}e^{-r/\sigma} - e^{-r/\sigma}\right]. \tag{C.12}$$

Using the Taylor expansion of $e^{-r/\sigma}$and simplifying gives the ion acceleration

$$\dot{v}_i = \frac{e^2 n_0}{m\epsilon_0} r \tag{C.13}$$

The resulting ion velocity is

$$v_i = \frac{e^2 n_0}{m\epsilon_0} rt, \tag{C.14}$$

which is linear in both position and time. This is in agreement with the linear portion of the velocity transects at the center of the exponential plasma, suggestive of the dominance of Coulomb repulsion at the center.

Bibliography

[1]R. Dendy, ed., *Plasma dynamics* (Oxford University Press, New York, 1990).

[2]J. T. Karpen and C. R. DeVore, "Nonlocal thermal transport in solar flares", Astrophysical Journal **320**, 904 (1987).

[3]D. Winget, M. Montgomery, B. Dunlap, P. Cho, M.-A. Schaeuble, and T. Gomez, "Illuminating white dwarf spectra through laboratory experiments at cosmic conditions", High Energy Density Physics **37**, 100853 (2020).

[4]P. Girard, J. Köppen, and A. Acker, "Chemical compositions and plasma parameters of planetary nebulae with Wolf-Rayet and wels type central stars", **463**, 265–274 (2007).

[5]A. Bapat, P. B. Salunkhe, and A. V. Patil, "Hall-effect thrusters for deep-space missions: a review", IEEE Transactions on Plasma Science **50**, 189–202 (2022).

[6]T. Bolgeo, A. Maconi, M. Gardalini, D. Gatti, R. Di Matteo, M. Lapidari, Y. Longhitano, G. Savioli, A. Piccioni, and C. Zanza, "The role of cold atmospheric plasma in wound healing processes in critically ill patients", Journal of Personalized Medicine **13**, 10.3390/jpm13050736 (2023).

[7]D. Yan, J. H. Sherman, and M. Keidar, "Cold atmospheric plasma, a novel promising anti-cancer treatment modality", Oncotarget **8**, 15977–15995 (2017).

[8]A Djaoui, B Shiwai, T. A. Hall, R. W. Eason, and C Jackson, "Interpretation of exafs data from laser shock compressed plasmas", Plasma Physics and Controlled Fusion **31**, 111 (1989).

[9]O. A. Hurricane, P. K. Patel, R. Betti, D. H. Froula, S. P. Regan, S. A. Slutz, M. R. Gomez, and M. A. Sweeney, "Physics principles of inertial confinement fusion and u.s. program overview", Rev. Mod. Phys. **95**, 025005 (2023).

[10]Y. Qian and B. Huang, "Recent progress for different inertial confinement fusion schemes: a systematical review", Journal of Physics: Conference Series **2108**, 012095 (2021).

[11]M. Haines, "Plasma containment in cusp-shaped magnetic fields", Nuclear Fusion **17**, 811 (1977).

[12]K. N. Leung, N. Hershkowitz, and K. R. MacKenzie, "Plasma confinement by localized cusps", The Physics of Fluids **19**, 1045–1053 (1976).

[13]H. Abu-Shawareb et al., "Lawson criterion for ignition exceeded in an inertial fusion experiment", Phys. Rev. Lett. **129**, 075001 (2022).

[14]T. C. Killian, S. Kulin, S. D. Bergeson, L. A. Orozco, C. Orzel, and S. L. Rolston, "Creation of an ultracold neutral plasma", Physical Review Letters **83**, 4776 (1999).

[15]T. Kroker, K. Großmann Mario andSengstock, M. Drescher, P. Wessels-Staarmann, and J. Simonet, "Ultrafast electron cooling in an expanding ultracold plasma", Nature Commuications **12**, 596 (2021).

[16]J. P. Morrison, C. J. Rennick, J. S. Keller, and E. R. Grant, "Evolution from a molecular Rydberg gas to an ultracold plasma in a seeded supersonic expansion of no", Phys. Rev. Lett. **101**, 205005, 205005 (2008).

[17]N Saquet, J. P. Morrison, M Schulz-Weiling, H Sadeghi, J Yiu, C. J. Rennick, and E. R. Grant, "On the formation and decay of a molecular ultracold plasma", Journal of Physics B: Atomic, Molecular and Optical Physics **44**, 184015 (2011).

[18]G. Bannasch, T. C. Killian, and T. Pohl, "Strongly coupled plasmas via Rydberg blockade of cold atoms", Physical Review Letters **110**, 253003 (2013).

[19]S. Laha, P. Gupta, C. E. Simien, H. Gao, J. Castro, and T. C. Killian, "Experimental realization of an exact solution to the vlasov equations for an expanding plasma", Phys. Rev. Lett. **99**, 155001 (2007).

[20]P. Gupta, S. Laha, C. E. Simien, H. Gao, J. Castro, T. C. Killian, and T. Pohl, "Electron-temperature evolution in expanding ultracold neutral plasmas", Phys. Rev. Lett. **99**, 75005 (2007).

[21]P. McQuillen, J. Castro, T. Strickler, S. J. Bradshaw, and T. C. Killian, "Ion holes in the hydrodynamic regime in ultracold neutral plasmas", Phys. Plasmas **20**, 043516 (2013).

[22]M. K. Warrens, G. M. Gorman, S. J. Bradshaw, and T. C. Killian, "Expansion of ultracold neutral plasmas with exponentially decaying density distributions", Phys. Plasmas **28**, 022110 (2021).

[23]P. McQuillen, J. Castro, S. J. Bradshaw, and T. C. Killian, "Emergence of kinetic behavior in streaming ultracold neutral plasmas", Phys. Plasmas **22**, 043514 (2015).

[24]G. M. Gorman, M. K. Warrens, S. J. Bradshaw, and T. C. Killian, "Magnetic confinement of an ultracold neutral plasma", Phys. Rev. Lett. **126**, 085002 (2021).

[25]G. M. Gorman, M. K. Warrens, S. J. Bradshaw, and T. C. Killian, "Laser-induced-fluorescence imaging of a spin-polarized ultracold neutral plasma in a magnetic field", Phys. Rev. A **105**, 013108 (2022).

[26]R. T. Sprenkle, S. D. Bergeson, L. G. Silvestri, and M. S. Murillo, "Ultracold neutral plasma expansion in a strong uniform magnetic field", Phys. Rev. E **105**, 045201 (2022).

[27]G. Bannasch, J. Castro, P. McQuillen, T. Pohl, and T. C. Killian, "Velocity relaxation in a strongly coupled plasma", Phys. Rev. Lett. **109**, 185008 (2012).

[28]T. S. Strickler, T. K. Langin, P. McQuillen, J. Daligault, and T. C. Killian, "Experimental measurement of self-diffusion in a strongly coupled plasma", Phys. Rev. X **6**, 021021 (2016).

[29]T. Langin, G. Gorman, and T. Killian, "Laser cooling of ions in a neutral plasma", Science **363**, 61 (2019).

[30]L. G. Silvestri, R. T. Sprenkle, S. D. Bergeson, and M. S. Murillo, "Relaxation of strongly coupled binary ionic mixtures in the coupled mode regime", Physics of Plasmas **28**, 062302 (2021).

[31]R. T. Sprenkle, L. G. Silvestri, M. S. Murillo, and S. D. Bergeson, "Temperature relaxation in strongly-coupled binary ionic mixtures", Nature Communications **13**, 15 (2022).

[32]J. P. Morrison, N Saquet, and E. R. Grant, "Classical scaling and the correspondence between the coupled rate equation and molecular dynamics models for the evolution of ultracold neutral plasma", Journal of Physics B: Atomic, Molecular and Optical Physics **45**, 025701 (2012).

[33]V. S. Dharodi and M. S. Murillo, "Sculpted ultracold neutral plasmas", Phys. Rev. E **101**, 023207 (2020).

[34]M. S. Murillo, "Ultrafast phase-space dynamics of ultracold, neutral plasmas", Journal of Physics A: Mathematical and Theoretical **42**, 214054 (2009).

[35]T. C. Killian, T. Pattard, T. Pohl, and J. M. Rost, "Ultracold neutral plasmas", Physics Reports **449**, 77 (2007).

[36]J. Castro, P. McQuillen, and T. C. Killian, "Ion acoustic waves in ultracold neutral plasmas", Phys. Rev. Lett. **105**, 065004 (2010).

[37]T. C. Killian, P. McQuillen, T. M. O'Neil, and J. Castro, "Creating and studying ion acoustic waves in ultracold neutral plasmas", Phys. Plasmas **19**, 055701 (2012).

[38]J. Castro, H. Gao, and T. C. Killian, "Using sheet fluorescence to probe ion dynamics in an ultracold neutral plasma", Plasma Phys. Control. Fusion **50**, 124011 (2008).

[39]Y. C. Chen, C. E. Simien, S. Laha, P. Gupta, Y. N. Martinez, P. G. Mickelson, S. B. Nagel, and T. C. Killian, "Electron screening and kinetic-energy oscillations in a strongly coupled plasma", Phys. Rev. Lett. **93**, 265003 (2004).

[40]D. Swanson, ed., *Plasma kinetic theory* (Taylor and Francis, New York, 2008).

[41]S. D. Baalrud, "Transport coefficients in strongly coupled plasmas", en, Physics of Plasmas **19**, 030701 (2012).

[42]S. D. Baalrud and J. Daligault, "Extending plasma transport theory to strong coupling through the concept of an effective interaction potential", Physics of Plasmas **21**, 055707 (2014).

[43]S. D. Baalrud and J. Daligault, "Modified Enskog kinetic theory for strongly coupled plasmas", Physical Review E **91**, 063107 (2015).

[44]S. D. Baalrud and J. Daligault, "Effective potential kinetic theory for strongly coupled plasmas", AIP Conference Proceedings **1786**, 130001 (2016).

[45]S. D. Baalrud and J. Daligault, "Mean force kinetic theory: a convergent kinetic theory for weakly and strongly coupled plasmas", Physics of Plasmas **26**, 082106 (2019).

[46]E. Vikhrov, S. Y. Bronin, B. B. Zelener, and B. V. Zelener, "Ion wave formation during ultracold plasma expansion", Phys. Rev. E **104**, 015212 (2021).

[47]S. Y. Bronin, E. V. Vikhrov, B. B. Zelener, and B. V. Zelener, "Ultracold plasma expansion in quadrupole magnetic field", Phys. Rev. E **108**, 045209 (2023).

[48]T. C. Killian, "Ultracold neutral plasmas", Science **316**, 705 (2007).

[49]P. Debye and E. Huckel, "Zur theorie der elektrolyte", Physikalische Zeitschrift **9**, 15–206 (1923).

[50]T. K. Langin, T. Strickler, N. Maksimovic, P. McQuillen, T. Pohl, D. Vrinceanu, and T. C. Killian, "Demonstrating universal scaling for dynamics of yukawa one-component plasmas after an interaction quench", Phys. Rev. E **93**, 023201 (2016).

[51]F. F. Chen, *Introduction to plasma physics and controlled fusion* (Springer, 2018).

[52]L. Spitzer, Jr., *Physics of fully ionized gases* (Wiley, New York, 1962).

[53]S. Mazevet, L. A. Collins, and J. D. Kress, Phys. Rev. Lett. **88**, 55001 (2002).

[54]D. O. Gericke and M. S. Murillo, "Disorder-induced heating of ultracold plasmas", Contributions to Plasma Physics **43**, 298 (2003).

[55]S. Hamaguchi, R. T. Farouki, and D. H. E. Dubin, Phys. Rev. E **56**, 4671 (1997).

[56]M. S. Murillo, "Using fermi statistics to create strongly coupled ion plasmas in atom traps", Phys. Rev. Lett. **87**, 115003 (2001).

[57]T. Pohl, T. Pattard, and J. M. Rost, "Coulomb crystallization in expanding laser-cooled neutral plasmas", Physical Review Letters **92**, 155003 (2004).

[58]C. Foot, *Atomic physics* (Oxford University, Oxford, 2005).

[59]M. Warrens, "Using an anti-MOT to laser cool the ions in an ultracold neutral plasma to $\Gamma > 11$", Master's thesis (Rice University, 2019).

[60]S. B. Nagel, C. E. Simien, S. Laha, P. Gupta, V. S. Ashoka, and T. C. Killian, "Magnetic trapping of metastable $^3P_2$ atomic strontium", Phys. Rev. A **67**, 011401(R), 011401(R) (2003).

[61]C. E. Simien, Y. C. Chen, P. Gupta, S. Laha, Y. N. Martinez, P. G. Mickelson, S. B. Nagel, and T. C. Killian, "Using absorption imaging to study ion dynamics in an ultracold neutral plasma", Physical Review Letters **92**, 143001 (2004).

[62]T. K. Langin, "Laser cooling of ions in a neutral plasma", PhD thesis (Rice University, 2018).

[63]T. C. Killian, M. J. Lim, S. Kulin, R. Dumke, S. D. Bergeson, and S. L. Rolston, "Formation of Rydberg atoms in an expanding ultracold neutral plasma", Phys. Rev. Lett. **86**, 3759 (2001).

[64]R. S. Fletcher, X. L. Zhang, and S. L. Rolston, "Using three-body recombination to extract electron temperatures of ultracold plasmas", Phys. Rev. Lett. **99**, 145001 (2007).

[65]P. McQuillen, J. Castro, and T. C. Killian, "High-resolution ionization of ultracold neutral plasmas", Journal of Physics B: Atomic, Molecular and Optical Physics **44**, 184013 (2011).

[66]P McQuillen, T. Strickler, T Langin, and T. C. Killian, "Ion temperature evolution in an ultracold neutral plasma", Physics of Plasmas **22**, 033513 (2015).

[67]S. Kulin, T. C. Killian, S. D. Bergeson, and S. L. Rolston, "Plasma oscillations and expansion of an ultracold neutral plasma", Phys. Rev. Lett. **85**, 318 (2000).

[68]F. Robicheaux and J. D. Hanson, "Simulated expansion of an ultra-cold, neutral plasma", Phys. Plasmas **10**, 2217 (2003).

[69]T. Pohl, T. Pattard, and J. M. Rost, "Kinetic modeling and molecular dynamics simulation of ultracold neutral plasmas including ionic correlations", Phys. Rev. A **70**, 033416 (2004).

[70]T. Pohl, T. Pattard, and J. M. Rost, "Coulomb crystallization in expanding laser-cooled neutral plasmas", Phys. Rev. Lett. **92**, 155003 (2004).

[71]E. A. Cummings, J. E. Daily, D. S. Durfee, and S. D. Bergeson, "Flourescence measurements of expanding strongly coupled neutral plasmas", Phys. Plasmas **12**, 123501 (2005).

[72]M. A. Viray, S. A. Miller, and G. Raithel, "Coulomb expansion of a cold non-neutral rubidium plasma", Phys. Rev. A **102**, 033303 (2020).

[73]M. K. Warrens, N. P. Inman, G. M. Gorman, B. T. Husick, S. J. Bradshaw, and T. C. Killian, "Wave steepening and shock formation in ultracold neutral plasmas", Physics of Plasmas **31**, 113503 (2024).

[74]Y.-Y. Sun, M. M. Shen, Y.-L. Tsai, C.-Y. Lin, M.-Y. Chou, T. Yu, K. Lin, Q. Huang, J. Wang, L. Qiu, C.-H. Chen, and J.-Y. Liu, "Wave steepening in ionospheric total electron density due to the 21 august 2017 total solar eclipse", Journal of Geophysical Research: Space Physics **126**, e2020JA028931 (2021).

[75]D. Umstadter, R. Williams, C. Clayton, and C. Joshi, "Observation of steepening in electron plasma waves driven by stimulated raman backscattering", Phys. Rev. Lett. **59**, 292–295 (1987).

[76]A. Balogh and R. A. Treumann, *Physics of collisionless shocks* (Springer, New York, New York, 2013).

[77]W. Snow, "Survey of acoustic characteristics of bullet shock waves", IEEE Transactions on Audio and Electroacoustics **15**, 161–176 (1967).

[78]L. D. Landau and E. M. Lifshits, *Fluid mechanics* (Pergamon Press, Elmsford, New York, 1987).

[79]G. B. Whitham, *Introduction and general outline*, 1st ed. (Wiley-Interscience, New York : 1999).

[80]J. E. Lingeman, J. A. McAteer, E. Gnessin, and A. P. Evan, "Shock wave lithotripsy: advances in technology and technique", Nature Reviews Urology **6**, 660–670 (2009).

[81]R. B. Scott, S. J. Bradshaw, and M. G. Linton, "The dynamic evolution of solar wind streams following interchange reconnection", Astrophys. J. **933**, 72 (2022).

[82]R. A. Treumann, "Fundamentals of collisionless shocks for astrophysical application, 1. non-relativistic shocks", The Astronomy and Astrophysics Review **17**, 409 (2009).

[83]B. Campanella, S. Legnaioli, S. Pagnotta, F. Poggialini, and V. Palleschi, "Shock waves in laser-induced plasmas", Atoms **7** (2019).

[84]P. Shukla, W. M. Moslem, S. S. Duha, and A. A. Mamun, "Time evolution of cylindrical and spherical shock waves in an ultracold neutral plasma with non-maxwellian electrons", Europhys. Lett **96**, 65002 (2011).

[85]J. P. Morrison and E. R. Grant, "Dynamics of colliding ultracold plasmas", Phys. Rev. A **91**, 023423 (2015).

[86]C Sack and H Schamel, "Evolution of a plasma expanding into vacuum", Plasma Physics and Controlled Fusion **27**, 717 (1985).

[87]P. Mora, "Plasma expansion into a vacuum", Phys. Rev. Lett. **90**, 185002 (2003).

[88]G. Szypko, G. Gorman, and S. Bradshaw, "Modeling Fluid Evolution of Interchange Reconnection Aftermath", in, Vol. 55, 7, https://baas.aas.org/pub/2023n7i107p04 (2023).

[89]J. Centrella and J. W. Wilson, "Planar numerical cosmology. ii. the difference equations and numerical tests", The Astrophysical Journal Suplement Series **54**, 229–249 (1984).

[90]P. Gupta, "Expansion and electron temperature evolution in an ultracold neutral plasma", PhD thesis (Rice University, Houston, TX, 2007).

[91]M. Barbarino, M. Warrens, A. Bonasera, D. Lattuada, W. Bang, H. J. Quevedo, F. Consoli, R. De Angelis, P. Andreoli, S. Kimura, G. Dyer, A. C. Bernstein, K. Hagel, M. Barbui, K. Schmidt, E. Gaul, M. E. Donovan, J. B. Natowitz, and T. Ditmire, "Thermal and log-normal distributions of plasma in laser driven coulomb explosions of deuterium clusters", International Journal of Modern Physics E **25**, 1650063 (2016).

[92]E. V. Vikhrov, S. Y. Bronin, A. B. Klayrfeld, B. B. Zelener, and B. V. Zelener, Phys. Plasmas **27**, 120702 (2020).

[93]X. Long, S. S. Yu, A. M. Jayich, and W. C. Campbell, "Suppressed spontaneous emission for coherent momentum transfer", Phys. Rev. Lett. **123**, 033603 (2019).